Universidad Nacional Autónoma de México

Programa de Posgrado en Ciencias Físicas

Simulation and characterization of a high purity Germanium detector to measure low levels of radioactivity in materials

T E S I S

que para optar por el grado de

Maestro en Ciencias (Física)

PRESENTA:
Carlos Iván Ortega Hernández

Tutor Principal:
Dr. Alexis Armando Aguilar Arévalo
Instituto de Ciencias Nucleares

México, CDMX. Agosto 2020

Acknowledgements

This research was supported in part by the Global Challenge Research Funds project "Dark Matter: Instrumentation Development to observe the Invisible", GCRF United Kingdom, to the projects DGAPA-PAPIIT No. IN108917 and CONACYT No. CB-2014/24066 that allowed us to continue and deepen the research.

I would also like to extend my thanks to the support of the academic technician Ing. Mauricio Martínez Montero of the ICN in everything related to the Germanium detector operations at the ICN Detector Laboratory, Dr. Mariano Hernández Gil, to Head of the Department of Medicine, Surgery and Zootechnics for Equidae from Facultad de Medicina Veterinaria y Zootecnia, UNAM, for providing us access to their portable x-ray equipment, as well as the Technicians Samuel Aponte Landeros and Roberto Solís Jaquez of the same department, for their assistance taking the X-ray pictures of the detector.

Also, I extend my thanks to the technical assistance from the Neutrino and Dark Matter Laboratory team of IF-UNAM, directed by Dr. Eric Vázquez Jáuregui.

Abstract

In this project we developed a Monte Carlo simulation of the HPGe detector in ICN-UNAM lab by using the simulation toolkit Geant4. Using a collection of radioactive point sources, we calculated experimentally the photopeak efficiency at 25 cm. The result led us to adjust some the inner parameters of the ICN HPGe sensitive crystal since no technical sheet was provided by manufacturer. By initializing outgoing photons, the simulated efficiency curve was calculated obtaining a percentage error of 9.47 % between both results. Then, by diluting several salt substitute weights into injectable solution a set of extended samples were prepared to measure the actual concentration of ^{40}K. This was achieved by implementing the sample's geometry in the simulation and setting the photon energy as ^{40}K gamma energy to calculate the photopeak efficiency. This lead us to determine the ratio of ^{40}K milligrams per salt substitute gram whose result give a percentage error of 9.41% compared with the central value of label information.

Introduction

The high purity Germanium (HPGe) detectors are widely used in spectroscopy due to their high atomic number that lead Ge to have a much larger linear attenuation coefficient and hence a shorter mean free path. These properties make Ge the material of choice for hard X-ray or gamma-ray detection to achieve higher detection efficiency. HPGe detectors are mainly used to determine the existence and concentration of radioactive isotopes in common objects for human consumption as well as industrial components for the construction of high energy physics experiments that require ultra-low background levels.

The cryogenics lab at ICN-UNAM has HPGe which was donated by Fermilab to perform low activity measurements in materials. The ICN-HPGe detector is part of the LABChico research program, the first underground laboratory for academic purposes at the Comarca Minera UNESCO Global Geopark [33], in the Mexican state of Hidalgo. LABChico will focus on applications for environmental radiation monitoring, gamma ray assay and screening, as well as prototype design for detectors in underground astro-particle physics experiments.

In this thesis the first measurements and characterization of the efficiency are presented. Its structure is the following: In chapter 1 the basics of radioactive emission form active isotopes are presented with especial emphasis in gamma radiation, going through the decay rates of radioactive nuclei. Then a review of the mechanisms of interaction between matter and gamma radiation is given, to understand the actual effect of radiation on real detectors.

In chapter 2 a review of radiation detectors is given, in which the main features of each type are presented and classified according the general purposes of research for which they are used. Going deeper into semiconductor detector type and into their operation and performance according to the atomic structure, the Germanium detector is highlighted due to its good energy resolution. Finally, the importance of HPGe detectors in high-energy physics experiments is contrasted by presenting the current status of neutrinos experiments and their HPGe detector counting facilities.

Once the basic structure of HPGe detectors has been reviewed, the internal components of ICN's detector as well as its operational features and recollection data system are exposed in chapter 3, making special emphasis on its geometrical arrangement. Then, by setting a collection of point radioactive sources at a standard height of 25 cm from the detector's head the energy resolution is obtained for every gamma line emission from the source's set and then interpolated. Using these results the photopeak efficiency is calculated in a gamma [53,1333] keV energy range.

In chapter 4 the inner dimensions of the sensitive crystal are obtained by taking an X-ray scan of the detector's head. Using this information as well as the materials specified by manufacturer both the detector and the experimental setup geometries are implemented in Geant4. Some unknown parameters such as the dead layer width and the inner contact radius are adjusted according to a reference that scanned a Germanium detector from the same manufacturer with a collimated source to estimate such parameters. Along the chapter the event initialization in Geant4 is clarified to contrast it with our experimental setup. Then the simulated energy spectra is compared with experimental results and computing the photopeak efficiency with the same methodology, both experimental and simulated curves are compared.

Later, a experiment to measure ^{40}K concentration in salt substitute is performed by preparing extended samples. At the end of chapter 4 the basics of extended volumes that are composed by several materials declaration in Geant4 syntax are granted. This lead us to include the extended samples geometry in simulation and hence to extract the photopeak efficiency. From such result the total number of emitted gamma rays is determined. This lead us to determine its actual concentration which was compared to label information.

Finally, in chapter 5, the conclusions are presented, in which we compare the relative efficiency obtained through both methods with the reported by manufacturer.

The results obtained throughout this thesis project supporting the LABChico research program are waiting to be published in *Journal of Instrumentation* (JINST).

Contents

Chapter 1

Gamma Ray Spectroscopy

1.1 Radioactive emission

Nuclear Radiation is the emission of energy through photons, charge carriers or nucleons and it is usually categorized in Ionizing or Non-Ionizing, the former carries higher energy than 10 eV that is enough to break atomic or molecular bounds. Common sources of electromagnetic and particle radiation are radioactive materials that emit in three fundamental ways, Alpha (α), Beta (β) and Gamma (γ). In this project, we focus on gamma radiation, so we do a brief review of the remaining just for completeness.

1.1.1 Alpha Decay

Alpha decay is produced when a radioactive atom ejects double ionized Helium atom, which is known as α particle. This happens in order to stabilize nuclear and electromagnetic interactions inside its nucleus. The generic form of alpha decay is

$$ {}^{A}_{Z}X \longrightarrow {}^{A-4}_{Z-2}Y + {}^{4}_{2}He, \tag{1.1} $$

where upper index A is known as mass number while lower index Z as atomic number and X, Y are decaying father and daughter nuclei respectively. These symbols completely classify radioactive nuclei. This decay is most likely to happen for nuclei with high atomic numbers ($Z > 83$), in fact the most common case of such decay occurs in the radio isotope:

$$ {}^{226}_{88}Ra \longrightarrow {}^{222}_{86}Rn + {}^{4}_{2}He + Q, \tag{1.2} $$

where ${}^{222}_{86}$Rn is the most common isotope of radon and Q is the mass/energy deficit between initial and final state. This energy must be shared between the Rn and the α particle in a definite ratio due to the conservation of momentum. Since no secondary

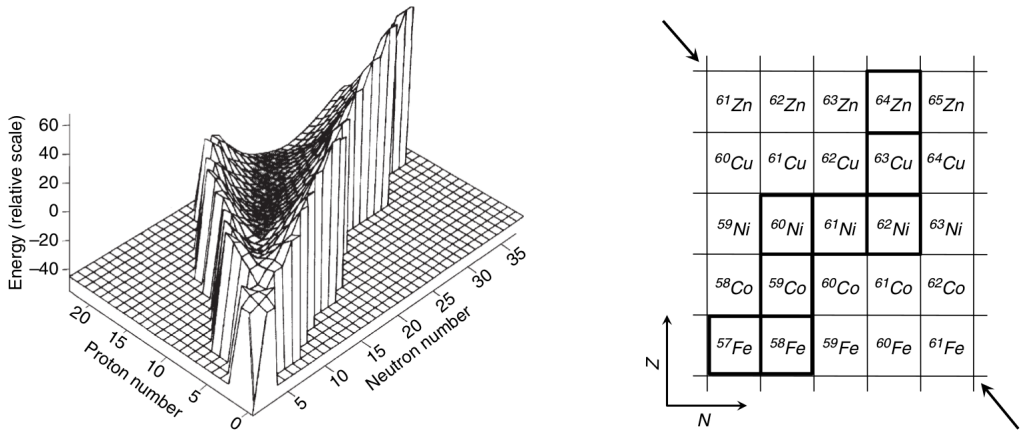

Figure 1.1: Segré chart of regions of stability and radioactive decay sequences can be mapped onto the schema [6].

particles are released in the decay then there is no a fraction of loosed energy. Thus, the alpha-particle is mono-energetic and alpha spectrometry becomes feasible.

1.1.2 Beta Decay

Beta decay is produced when an isotope is unstable due to an unbalanced relationship between its neutron number, N, the atomic number Z and its binding energy. Segrè chart [12], see figure 1.1, classifies isotopes as stable or unstable. While stable nuclides occupy the bottom of a nuclear-stability valley, unstable ones are outside this valley bottom. The most dominant radioactive decay channel occurs when a nuclide moves down the hillside directly to the valley bottom. This process is known as **beta decay**, by this process, unstable atoms obtain a more stable ratio of protons to neutrons.

β^- decay

A first case is when nuclide is located on the neutron rich side of stability. When a *down* quark is transformed into an *up* quark an electron and its correspondent antineutrino are released, this is possible due to weak interaction. From a nuclear point of view a neutron is transformed into a proton and a pair electron-antineutrino is released. This process is mainly represented through the following the transition:

$$n \longrightarrow p + \beta^- + \overline{\nu}_e, \tag{1.3}$$

where n is a neutron, p a proton, $\overline{\nu}_e$ a electron antineutrino and β^- is simply identified as the electron. Due to the presence of weak interaction and beside other factors these process are characterized by lengthy decay times or small decay probabilities.

β^+ decay

The process described in equation 1.3 can occur, also, in opposite direction through the same weak interaction mechanism. In this case the proton is transformed into a neutron and a positron with a neutrino are released. In the same way it is represented through:

$$p \longrightarrow n + \beta^+ + \nu_e, \tag{1.4}$$

where ν_e is the electron neutrino and β^- is a tag for the positron. From the chart point of view, this happens when the nuclide is located in the positron rich side of the stable chart. This is a decay easier to detect since emitted positron almost immediately interacts with an electron in the outer shells of the atom. Both the positron and the electron are annihilated and two gamma-rays are released. This annihilation process will be deepened later.

1.1.3 Gamma Decay

Gamma decay, unlike α and β decay, does not modify mass number A or atomic number Z. This decay mode produces electromagnetic radiation or gamma rays in a enormous range of energies. In this process an excited atom emits a gamma ray to decay to its ground state. In this process the atom is usually preceded by an alpha or beta decay:

$${}^A_Z X^* \longrightarrow {}^A_Z X + \gamma, \tag{1.5}$$

where the asterisk denotes excited states. The amount of energy in excited states depends on the charge and current distribution along the atom. Specifically, it depends on the multipolar electrical and magnetic distribution of the atom. Terms in such an expansion correspond to angular momenta in definite quantized units described by its quantum numbers l, m. These basic concepts are used to formulate selection rules in electromagnetic nuclear transitions and so gamma ray allowed energies.

A nuclear level is not infinitely accurate since the Heisenberg Uncertainty principle prohibits it, but it has a finite width related with lifetime by:

$$\delta E \times \delta t \geq \frac{\hbar}{2}, \tag{1.6}$$

where δt stands for uncertainty in excited state period. For practical purposes it can be taken as the mean life of the nuclear level, τ, to estimate its energy uncertainty.

1.1.4 Various photon sources

Bremsstrahlung

This radiation is produced by the continuous interaction of electrons in outer shells with the Coulomb electric field of the nucleus. The electron energy loss appears to be continuum of photon emission, mostly apparent in low energy range (X-ray range). This effect is only visible for light particles as electrons, although in principle the maximum energy is that of the beta-particle.

The Bremsstrahlung interaction is larger when the number atomic absorbers and beta-particle energy are both high. For example, for 1000 keV beta-particles in lead atoms ($Z = 82$) there is an appreciable effect while for betas of same energy in aluminium atoms ($Z = 13$) the effect is negligible. It follows that any structure near the detector, should be constructed of a low Z material such as a rigid plastic in order to reduce Bremsstrahlung effect.

X-ray emission

X-rays are mono-energetic gamma-rays, their energy is equal to the difference between electron energy levels. The nomenclature of X-rays is established according the transitions of the electrons between two energy shells. It can be better understood with the diagram shown in figure 1.2 (a). The K-shell has only one energy level. Higher shells have sub-shell levels; which in terms of quantum properties is said to be degenerate. This means that the electrons in each shell, apart from K-shell, have several states whose energy level is exactly the same. Hence, after a decay to a lower energy level, the emitted photon will carry the same energy for all sub-shells in the primary energy level. The only way to look at a nucleus fine structure is by putting in into a magnetic field. Then the sub-shells will give rise to different energy sub-levels, and hence new X-ray energies are available, just as seen in figure 1.2 (b).

The X-ray detection can give information of the element, nevertheless it is impossible to determine the actual isotope since the arrangement of the atomic electrons is determined only by the number of protons in the nucleus (Z) and not by its mass (A).

1.2 Decay rates

Radioactive decay is a statistical process, whereby unstable nuclei emit radiation that changes the state of the nucleus. As a first order process, the rate of decay, i.e. activity, is proportional to the number of atoms of radionuclei present in a source:

$$A = -\frac{dN}{dt} = \lambda N. \tag{1.7}$$

The solution of such differential equation is obtained considering an integrating factor,

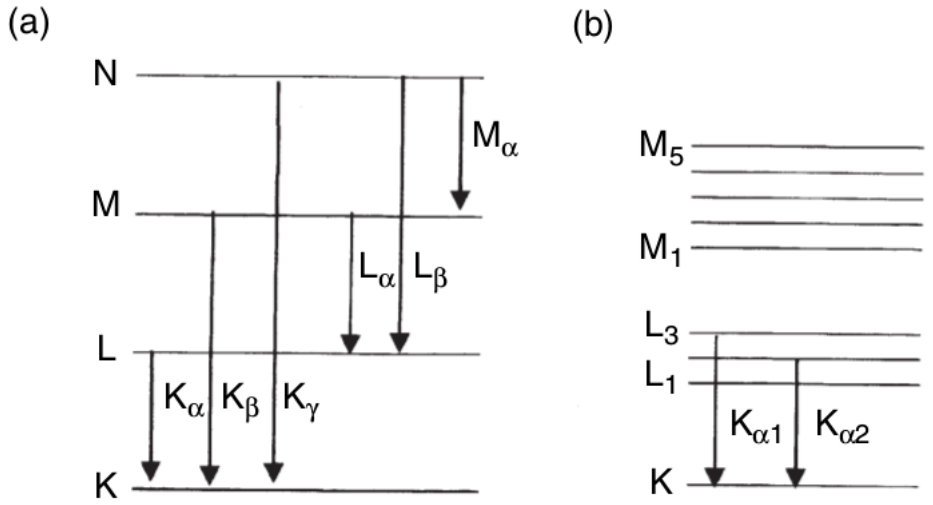

Figure 1.2: X-ray emission nomenclature for nuclei in excited levels [4].

$$N(t) = N_0 e^{-\lambda t}, \tag{1.8}$$

where N_0 is the number of atoms of radionuclei in the initial sample. The proportionality constant λ, called decay constant, is related with the average time an atom can be expected to exist before its nucleus decays, i.e. its mean life, τ. Such relationship becomes clear by integrating:

$$\tau = \frac{1}{N_0} \int_0^\infty dt N(t) t = \frac{1}{\lambda}. \tag{1.9}$$

In practice it results more convenient to deal with half-life, $t_{1/2}$ defined as to be the time during which the activity decreases to half its original value. Solving a algebraic equation similar to 1.9 a proportionality relationship it is found that $t_{1/2} = \tau \ln 2$. It must be clarified that equation 1.8 determine the population of a specific decay channel, so τ is a relative measure of time for every decay mode. When a radionuclide (parent) decays into a second radionuclide (daughter) the rate change of the number of active atoms of the daughter can be determined by considering the inclusion of more daughter kind atoms due to parent atom decay [5]. Then, the decay radio of daughter atoms follows the differential equation:

$$\frac{dN_d}{dt} = \lambda_p N_p - \lambda_d N_d = \lambda_p N_{p0} e^{-\lambda_p t} - \lambda_d N_d, \tag{1.10}$$

where p and d are tags for parent and daughter atoms respectively and $p0$ is a label for the initial population of the parent type atom. The solution of this linear

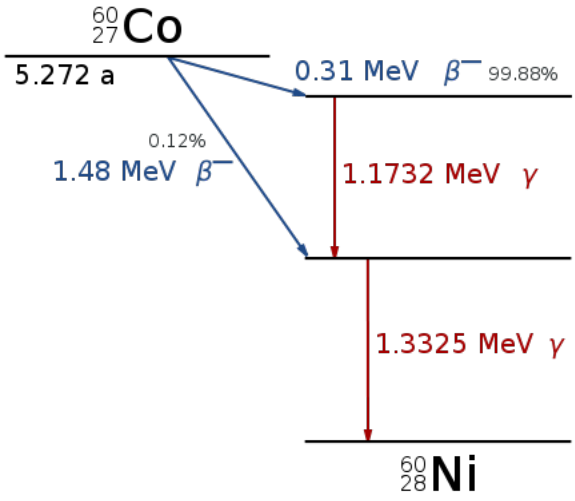

Figure 1.3: ^{60}Co consecutive gamma decay diagram [6].

differential equation is

$$N_d(t) = \frac{\lambda_p N_{p0}}{\lambda_d - \lambda_p}\left[e^{-\lambda_p t} - e^{-\lambda_d t}\right] + N_{d0}e^{-\lambda_d t}, \tag{1.11}$$

where $d0$ is a label for the initial population of the daughter type atom. The most common case of this decay type is $^{60}_{27}$Co isotope which goes to an excited level of the isotope $^{60}_{28}$Ni through beta decay, then it goes to a lower excited state and release a 1173 keV gamma-ray [6]. Finally, the ground state is reached and a 1332 keV photon is released, as shown in figure 1.3.

1.3 Interaction of Gamma radiation with matter

The degree of interaction between gamma ray and matter depends upon photon energy as well as detector atomic structure, the denser the material the greater probability of dispersion of the photon with the electrons of the outer layers. The detailed shape of that energy dependency in linear attenuation coefficient is determined by the main mechanisms of interaction. Figure 1.4 shows the attenuation coefficient, μ, of a set of materials as a function of photon energy. This is an important quantity to determine the probability of an interaction per unit distance traveled inside the material given by

$$I(x|E_\gamma) = I_0 e^{-\mu(E_\gamma)x} \tag{1.12}$$

The attenuation coefficient is greater for materials with a higher atomic number. For this reason lead is used to cover up sensitive detectors since it is a more suitable

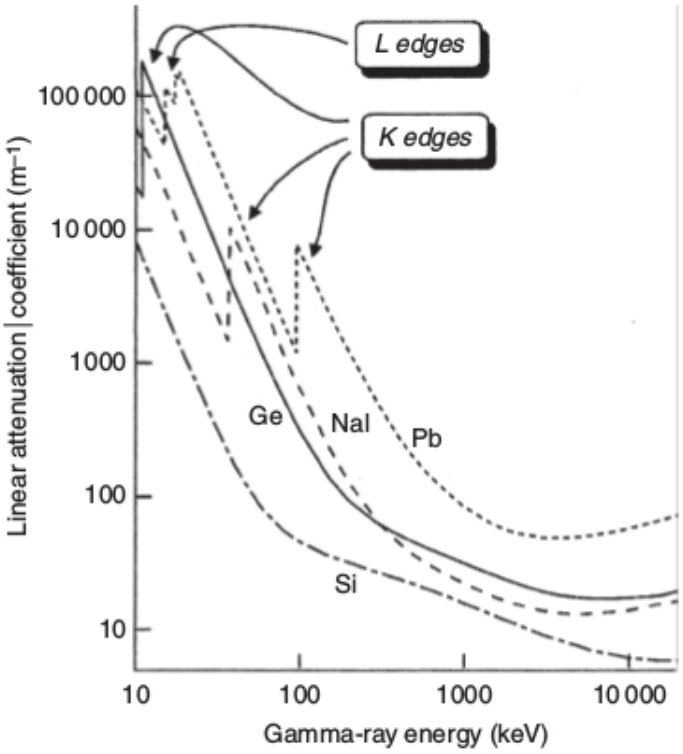

Figure 1.4: Attenuation coefficient of materials as a function of gamma-ray energy [4]

shielding material.

The linear attenuation coefficient as function of the incoming gamma-ray energy is composed by three fundamental curves of interaction named *Photoelectric effect*, *Compton scattering* and *Pair production*, see figure 1.4. Each of these has an relative magnitude and an energy range that we will discuss along the chapter.

1.3.1 Photoelectric Effect

Photoelectric Effect arises when a gamma-ray interacts with a bounded electron in an atom (figure 1.5 (a)). If the photon has enough energy to break-up the bound, the electron will be ejected from its shell with a kinetic energy E_e, given by

$$E_e = E_\gamma - E_b, \tag{1.13}$$

where E_γ and E_b are the gamma-ray and bound energies respectively. After the ejection, the atom is left in an excited state with an excess of energy E_b. There are two ways in which the atom can recover its equilibrium.

- By redistributing the excitation energy between the remaining electrons in its shells. This result in the release of further electrons from the atom which

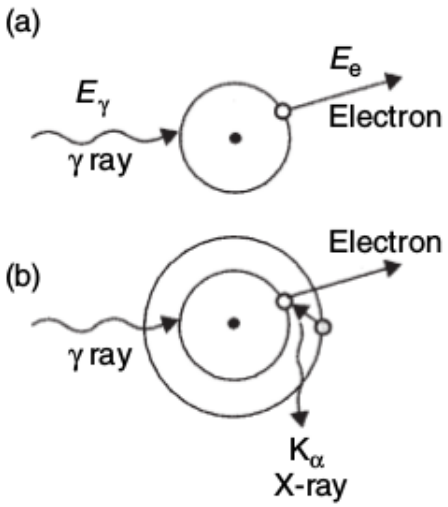

Figure 1.5: (a) The mechanism of photoelectric absorption, (b) the emission of X-rays [4]

transfers a further fraction of the total gamma-ray energy to the detector. This process is known as *Auger cascade*.

- By filling the left vacancy with an upper-shell electron falling into it with the emission of a characteristic X-ray.

For the second way, the emitted X-ray is a low-energy photon since its energy comes out from the difference of energy levels, as shown in figure 1.5 (b). This X-ray may then in turn undergo photoelectric absorption once more, perhaps emitting further X-rays which are absorbed and so on until ultimately all of the energy of the initial gamma-ray is absorbed by the material.

The most striking features in the curves of the figure 1.4 are the sharped jumps in low energy range. They are related with the energy shells from which electron is ejected. The most likely are electrons in K shell but if sufficient energy is not available then electrons from L or M shells will be ejected instead. This gives rise to the discontinuities in the photoelectric absorption curves.

1.3.2 Compton scattering

Compton scattering is the inelastic scattering of a photon with an electron, first discovered in 1923 by Arthur Compton. It is a well studied process since it can be described to a high level of precision by the theory of quantum electrodynamics (QED). The cross-section is an important quantity since it is directly measured and can be used to test the validity of a theory.

This project does not pretend to extensively treat with the cross section, named σ, calculation. However, since it is most often the predominant interaction mechanism a

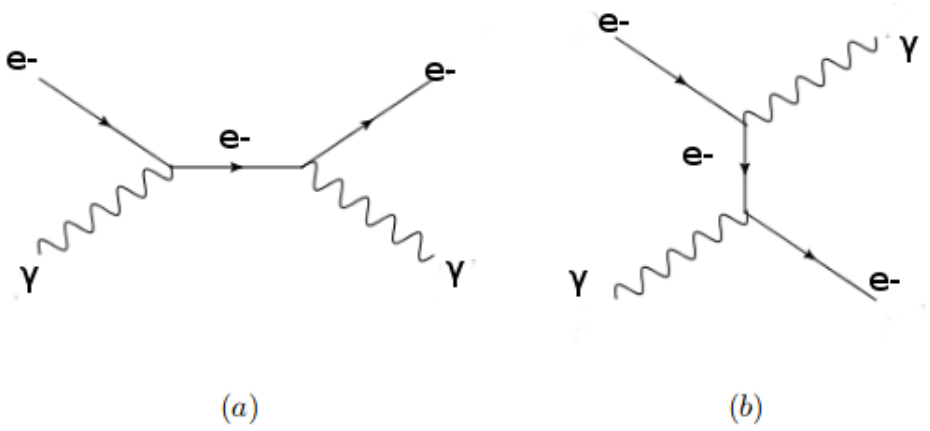

Figure 1.6: Tree-level Feynman diagrams contributing to the matrix element of the Compton scattering process [1]

brief review of the main concepts and tools is given, without loss of the general scope, to obtain the first order approximation. Considering only the tree-level diagrams and using the Feynman rules for QED , the matrix elements corresponding to the channels t and s, shown in 1.6 (a) and (b) respectively, can be calculated [1].

The total matrix element, $\mathcal{M}$, is obtained by adding both matrix elements from the channels t and $\mathbf{s}$. Below are the steps to obtain the energy spectrum of Compton scattering.

1. Compute $|\mathcal{M}|^2$, taking special care on the interference term.
2. Averaging over all spin configurations for both electrons and over all polarization for both photons.
3. Determine the phase space: The region where the process is kinetically allowed.
4. Recalling Feynman's Golden rule for cross-section calculation. Such rule provides us to a energy-momentum conservation relationships. The former relates both incoming photon energy, E_γ, and scattered photon energy, E'_γ, through the scatter angle, θ. Such relationships, in natural units ($\hbar = c = 1$), are given by:

$$E'_\gamma = \frac{E_\gamma}{1 + \frac{E_\gamma}{m_e}(1 - \cos\theta)}, \tag{1.14}$$

$$E_e = E_\gamma - E'_\gamma \tag{1.15}$$

where m_e is the mass of the electron.

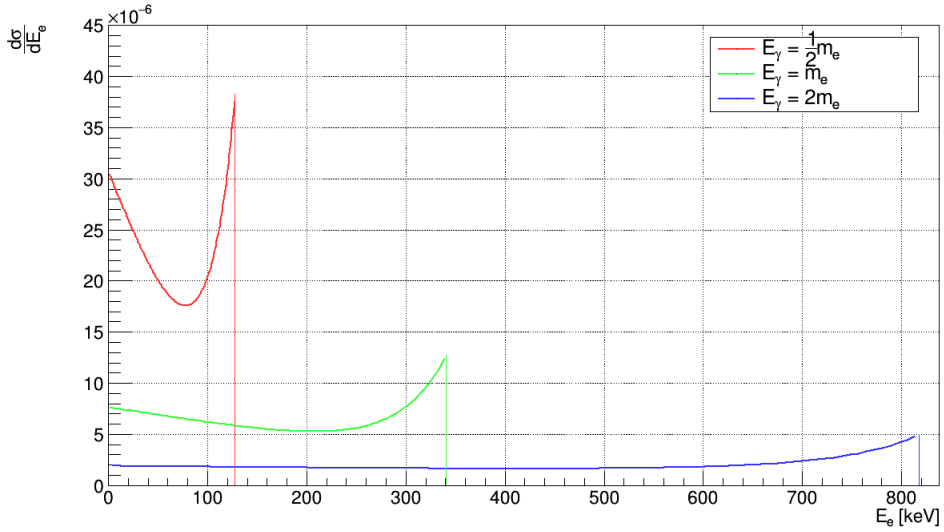

Figure 1.7: Klein-Nishima spectrum for several values of incoming photon energies in terms of electron's mass: (a) $E_\gamma = \frac{1}{2}m_e$, (b) $E_\gamma = m_e$ and (c) $E_\gamma = 2m_e$

5. Partially integrating over the phase space and letting the incoming gamma-ray energy as a free parameter to obtain the differential cross-section, that reads:

$$\frac{d\sigma}{d\cos\theta} = \frac{\alpha^2\pi}{m_e^2}\left(\frac{E'_\gamma}{E_\gamma}\right)^2\left(\frac{E'_\gamma}{E_\gamma} + \frac{E_\gamma}{E'_\gamma} - \sin^2\theta\right), \tag{1.16}$$

where α is the fine structure constant.

6. Substituting 1.14 and 1.15 in 1.16 to obtain the energy spectrum, which is given by

$$\frac{d\sigma}{dE_e} = \frac{\alpha^2\pi}{m_e\left(E_\gamma - E_e\right)^2}\sqrt{1-\frac{E_e}{E_\gamma}}\left\{\frac{E_\gamma}{E_\gamma - E_e} - \frac{E_e}{E_\gamma} + \left(1 - \frac{m_e}{E_\gamma}\frac{E_e}{E_\gamma - E_e}\right)^2\right\} \tag{1.17}$$

this result is best known as *Klein-Nishima spectrum.*

The Compton edge is defined to be the Klein-Nishima spectrum evaluated at $\theta = 0$, that is the maximum energy transfer to the remaining photon in 1.14, and its height depends on the energy of the incoming photon E_γ. Figure 1.7 shows the evaluation of 1.17 for some values of E_γ.

1.3.3 Pair production

Pair production is produced when gamma radiation interacts with the electromagnetic field of the whole atom. Again, as a result of quantum electrodynamics, incoming

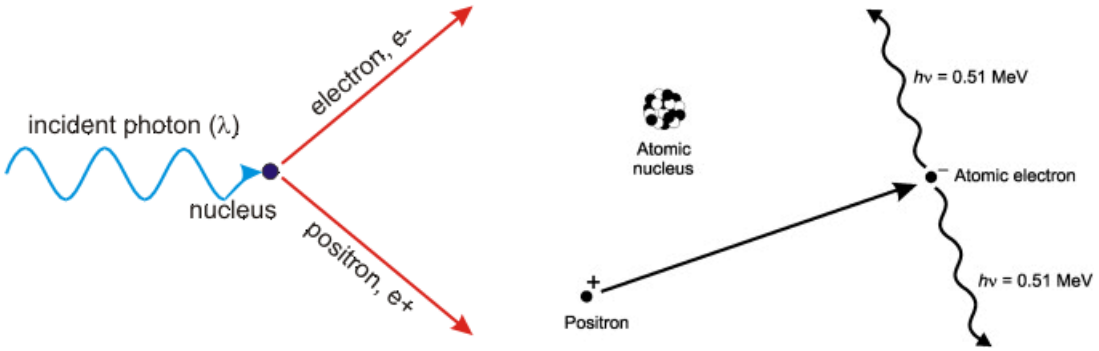

Figure 1.8: (a) Pair production (b) Pair annihilation [4]

photon gives rise to a pair electron-positron, see figure 1.8 (a). A minimum amount of energy is needed for this process to take place, naturally twice the mass of the electron that is the pair total energy at rest. It is also possible that the photon turns into a pair electron-positron by interacting with the Coulomb field of an electron from the outer shells. The probability for this happening is much smaller and this process is only visible up to gamma-ray energies of 3 MeV since the field is light due to a screening produced by the nucleus field.

When the energy of the positron is reduced by attenuation near thermal energies, it must inevitably meet an electron and the two will annihilate to give rise to two photons with same energy (due to momentum conservation) of 511.0 keV, just as shown in figure 1.8 (b). This is likely to happen within 1 *ns* of creation of the pair and, considering that the charge collection time of typical detectors is 100 up to 700 *ns*, the annihilation can be regarded as instantaneous with the pair production event. The net amount of energy deposited in detector by the immediate consequences of the pair production event is:

$$E_e = E_\gamma - 2m_e, \tag{1.18}$$

Unlike Compton scattering, the cross-section of pair production is a slowly increasing function that is mostly dominant in high energy range. According to Bethe-Heitler approximation it reads

$$\sigma_{pair} \approx \alpha Z^2 r_e^2 \ln E_\gamma, \tag{1.19}$$

where α is the fine structure constant, r_e the classic electron radius and Z the atomic number. This result can be obtained by considering:

- The scattering potential of a neutral or partially ionized atom.
- The Born approximation for the interaction of the scattering electron with such potential.

- The invariant matrix element, $\mathcal{M}$, that follows from effective interactions of electron with transformed potential.

Since pair production takes place in a energy range of little coincidence with the region of interest, it barely will be taken into account to data analysis.

1.4 Interaction with shielding

There are features in energy spectra which are not direct consequences of the interaction of the γ-ray with the detector itself. When a shielding is placed over the detector in order to protect it from outcoming beams foreign to the original source, then the radiation is likely to interact through the main mechanisms with the surrounding material. In this case the direct effect in energy spectra is quite different.

The mechanism with a greater weight in the side effects is the photoelectric effect. A single photoelectric absorption can be followed by the emission of a characteristic X-ray of the absorbing medium. There is a small but significant possibility that this fluorescent X-ray may escape the shielding and interacts with the detector. The result will be a number of X-ray peaks in the energy spectrum in the 70-90 keV energy region [8]. To solve this problem it is necessary the usage of graded shields, that is to cover the lead shield with further more layers. The choose of such layers depend upon the spectroscopy scopes and the energy range being studied. Figure 1.9 shows an usual arrangement of shielding shells for Na(I) and Ge detectors. Here, the Cd layer is able to absorb the Pb X-rays. Nevertheless this results into the emission of Cd characteristic X-rays whose energies are in 20-26 keV range, that can in turn be absorbed by a Cu layer. Typically Cu characteristic X-rays are too low in energy (about 8 keV) to figure as a problem in an actual energy spectrum since mostly used detectors in spectroscopy are even not able to measure such energy scale.

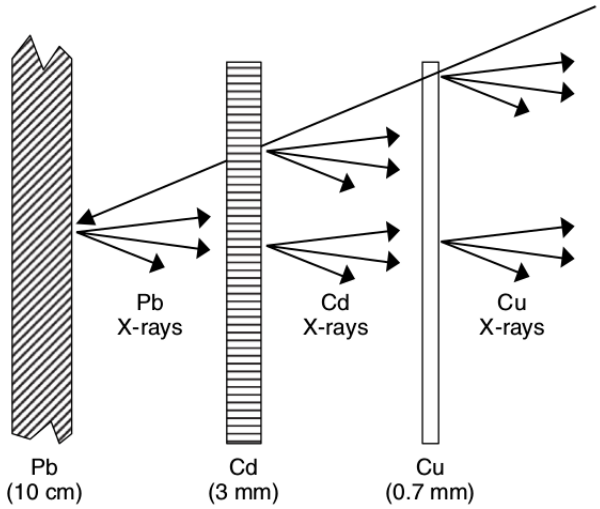

Figure 1.9: Graded shield standard shell configuration for general purposes of spectroscopy [8]

Chapter 2

High Purity Germanium Detectors

As introduced in chapter one there are several mechanism of interaction between radiation and matter. When an incoming photon passes within a material, it transfers a fraction of its kinetic energy to electrons by ionizing atoms. This is achieved by such mechanisms from which electrons, positrons and photons emerge. Then this set of secondary particles gives rise to ion pairs and they determine the actual signal in a detector. By choosing adequately the interaction media one could optimize the signal depending on the objective of the experiment and the range of energy of interest. Throughout this chapter we will give a brief review of radiation detectors, delving into solid semiconductor type and finally into high purity Germanium detectors (HPGe), which are the object of study for wide ranges of energy and high resolution.

2.1 Radiation detectors

A fundamental feature of nuclear processes is that the energy released is larger than the binding energies of atomic electrons. Any emitted particles will have sufficient energy to ionize atoms. Nuclear radiation is called ionizing radiation, therefore, and detecting this ionization allows us to observe nuclear processes. The radiation detectors are mainly classified by their ionizing media type that could be either solid, liquid or even gas.

2.1.1 Gas ionization

This is type of detector is mainly designed for protection applications to measure ionizing radiation, and also in particle physics to detect the presence of ionizing particles. The basic gaseous ionization detector consists of a chamber that is filled with a suitable medium that could be either air or a special fill gas [2]. Besides the operating medium must be easily ionized, there are other issues that should be into account:

- To be chemically stable (or inert) so that the moving ionization electrons are not easily captured by the molecules of that medium.

- To have a low value of ionization potential in order to maximize the amount of ionization produced per energy deposited by any incident particle.
- To not be very sensitive to radiation damage so that its response to incident particles does not change markedly with use.

The chamber has a cathode and an anode that are held at some large relative voltage, and the device is characterized by a capacitance that is determined by the geometry of the electrodes. As ionizing radiation enters the gas between the electrodes, a finite number of ion-pairs are formed. The behavior of the resultant ion-pairs is affected by the potential gradient of the electric field within the gas and the type and pressure of the fill gas

There is a relationship between the applied voltage and pulse height which may depends on several factors. Pulse height and the number of ion pairs collected are directly related, this deal is addressed in greater detail in the semiconductor section. The voltages can vary widely depending upon the detector geometry and the gas type and pressure. There are three basic types of gaseous ionization detectors, which are categorized according to the voltage applied to the detector:

- Ionization chambers,
- proportional counters,
- Geiger-Müller tubes.

Detectors of ionizing radiation can be used both for activity measurements as well as for dose measurement. With knowledge about the energy needed to form an pair of ions – the dose can be obtained.

2.1.2 Semiconductor Detectors

A material can be classified by the energy gap between valence and conduction band, as shown in figure 2.1, in *insulator*, *conductor* or *semiconductor* [3]. The former is characterized for having its valence band fully occupied thus preventing electrons in adjacent bands from reaching the conduction band. For an electron to migrate through the material, it must have enough energy to jump from the valence band across the band gap into the conduction band. The gap for insulators is about 10 eV, a energy amount that cannot be reached only by thermal vibrations [2]. Regardless of the magnitude of the applied field, the material will not be able to transport electric current.

Unlike insulators, conductors allow electrons to freely migrate from valence band to conduction band since both bands overlap. For this reason, thermal vibrations ensure that conduction band is continuously populated, therefore any light external field will cause a current flow. From a practical point of view, conductors are not useful for gamma ray detectors since thermal vibration produce a leakage currents whose background signal would fully dirt the actual current.

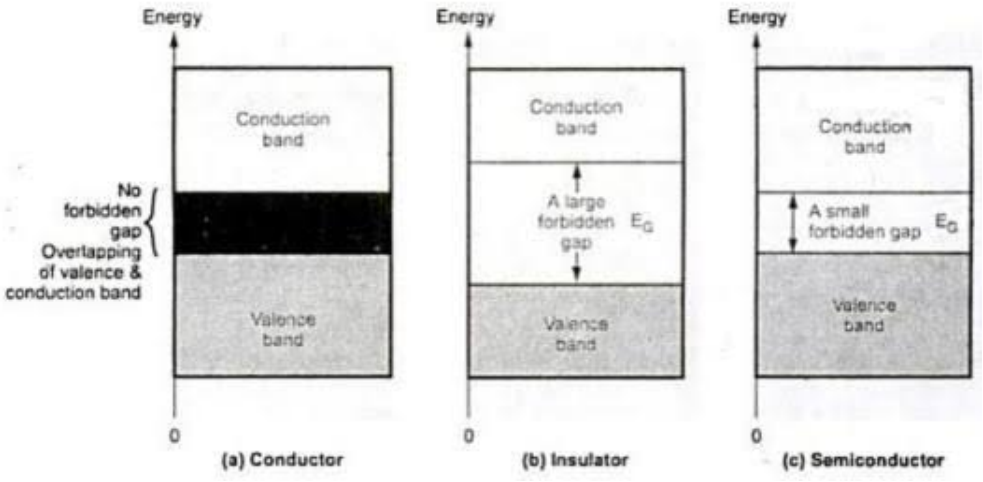

Figure 2.1: Energy band diagram for Insulator, Conductor and Semiconductor [2]

Just like insulators, semiconductors are characterized for having a valence band fully occupied but their band is much smaller, of the order of 1 eV, small enough to be reached by thermal vibrations. According to Boltzmann's statistical formulation [9], the probability that an electron be promoted to the conduction band reads

$$p(T|E_g) \propto T^{3/2} \exp\left(-\frac{E_g}{2k_B T}\right), \tag{2.1}$$

where E_g is the band gap, k_B the Boltzmann constant and T temperature. As realized in 2.1, transition probability is strongly influenced by temperature, therefore semiconductor detectors must be cooled in order to reduce noise signals.

A vacancy left by a electron previously promoted from any band to conduction band is effectively positively charged and is referred to as a hole. It is desirable that both charges and holes have a good mobility within a semiconductor, therefore must be no trapping centers that might prevent them reaching the collecting contacts. There are several types of trapping centers and are mainly consequence of:

- Impurities within detector lattice.
- Interstitial atoms and vacancies within the lattice caused by structural defects within the crystal.
- Interstitial atoms caused by radiation damage.

From practical point of view it is not possible to prepare a material completely free of impurities. An increase in the conductivity of a Semiconductor is observed when a small amount of impurity was added to it. Those materials that accomplish such property are known as *Doped Materials*, where the impurities are Dopants and the process is Doping.

The introduction of any kind of impurities modifies lattice arrangement, therefore new energy states are introduced, either just above the valence band or just below the conduction band. This results in a band gap narrowed and since the conductivity depends upon the number of electrons in the conduction band, the conductivity of a doped material will be higher than the intrinsic conductivity.

A lattice of fourvalent atoms (part of the fourth group in periodic table) such as Germanium and Silicon are doped using two types of dopants:

1. Pentavalet (valency 5): Arsenic (As), Antimony (Sb), Phosphorous (P), etc.
2. Trivalent (valency 3): Indium (In), Boron (B), Aluminium (Al), etc.

These dopants are used in order to ensure that size of the atoms is not much different from the fourth group. Hence, the trivalent and pentavalent choices. These dopants give rise to two types of semiconductors, *p-type* and *n-type*.

N-type semiconductor

An n-type semiconductor is created when pure semiconductors, like Si or Ge, are doped with pentavalent elements. As shown in figure 2.2 (a), when a pentavalent atom takes the place of a Si atom, four of its electrons bond with four neighbouring Si atoms. However, the fifth electron remains loosely bound to the parent atom. Hence, the ionization energy required to set this electron free is very small. Thereby, this electron can move in the lattice even at room temperature.

For a better perspective, the ionization energy required for silicon at room temperature is around 1.1 eV. On the other hand, by adding a pentavalent impurity, this energy drops to around 0.05 eV.

The number of electrons made available by the dopant atoms is independent of room temperature and primarily depends on the doping level. Also, as the temperature rises, the Ge (or Si) atoms free some electrons by thermal vibrations and generate some holes. But, the number of these holes is very small. Hence, at any given point in time, the number of free electrons is much higher than the number of holes.

P-type semiconductor

In the same way, a p-type semiconductor is created when trivalent elements are used to dope pure semiconductors. As shown in figure 2.2 (b), when a trivalent atom takes the place of a Si atom, three of its electrons bond with three neighbouring Si atoms. However, there is no electron to bond with the fourth Si atom. This leads to a hole or a vacancy between the trivalent and the fourth silicon atom. This hole initiates a jump of an electron from the outer orbit of the atom in the neighbourhood to fill the vacancy. This creates a hole at the site from where the electron jumps. In simple words, a hole is now available for conduction.

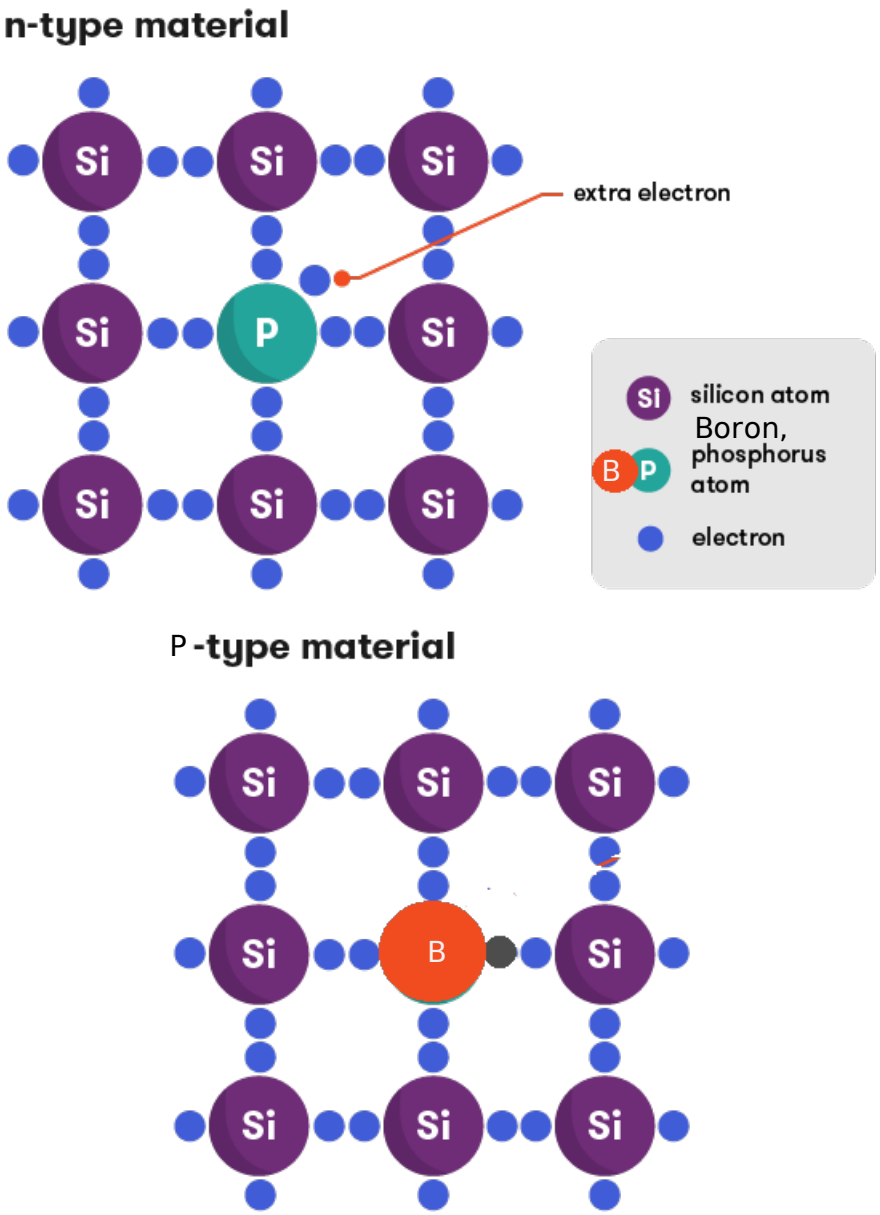

Figure 2.2: (a) Lattice arrangement of a n-type semiconductor. (b) Lattice arrangement of a p-type semiconductor [32]

In opposite case, the number of holes made available by the dopant atoms is independent of temperature and primarily depends on the doping level. As the temperature rises, the Ge (or Si) atoms free some electrons and generate some holes. The number of holes is much higher than the number of free electrons. Also, due to recombination, the number of free electrons reduce further.

P-N Junction

When the two dissimilar types of semiconductors are placed in contact, there is an electronic redistribution since p-type material has an excess of holes and n-type an excess of electrons, figure 2.3 (a). Holes may spread from the p side to the n side of the junction and electrons from the n side to the p side, figure 2.3 (b). Excess holes meeting excess electrons will combine together, mutually annihilating and creating a neutrally charged region known as *depletion region.*

On the other hand, the mutual migration of effective charges gives rise to the generation of a voltage across the junction called the contact or diffusion voltage, figure 2.3 (c). The depletion region is the active element of a detector and is very thin, but if a positive voltage is connected to the n side of the junction its width will increase as the electrons are withdrawn from the material. If a negative voltage is applied to the p side of the junction will withdraw the holes, this is called a reverse biased junction.

By solving Poisson's equation of flux density through the contact region [11] depletion layer width can be estimated as

$$d = \sqrt{\frac{2\epsilon_m}{e}\frac{N_a + N_d}{N_a N_d}\Delta V}, \tag{2.2}$$

where ϵ_m is the dielectric constant for the material, e is the fundamental charge, N_a and N_d are the total numbers of pentavalent dopants (donnors) and trivalent dopants (acceptors) respectively and ΔV is the voltage difference between the two regions which is independent from the total number of dopants. From 2.2 it is concluded that to maximize the depletion layer width and therefore the active detector region, the total number of impurities must be minimized.

Impurities migration

The migration of impurities in semiconductors involves different mechanisms which depend on the chemical properties of the impurity atoms and the lattice atoms. Some of they are the charge and size of the impurity atoms, the concentration of defects in the semiconductor, and the crystalline structure of the host lattice are all factors that can influence migrations. The most practical way to classify impurity migration in semiconductors is by the material group [24], that is the chemical properties of the semiconductor. Besides secondary effects such as changes in thermodynamic

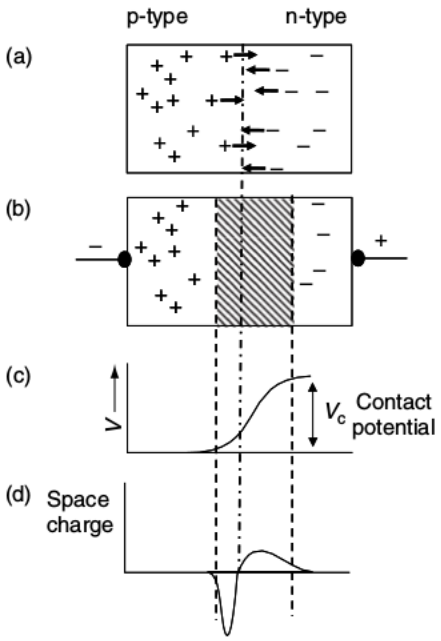

Figure 2.3: (a) p–n Junction before charge carrier redistribution. (b) Depletion region created by carrier redistribution. (c) Variation in potential across junction. (d) Variation in space charge across junction [4]

diffusion coefficient, the most important effect of impurities migration is that non uniform dopant distribution may result in inhomogeneous intrinsic electric fields that an application of large voltage can not compensate [25]. This result in very poor charge collection and hence a not very reliable signal.

This project is focused in Ge semiconductor detectors and, as we will see in the next section, its operational temperature is about 77 K. Unfortunately the impurities migration has been barely studied for the group IV in which germanium is located. The only known migration case is produced due to the Ge singly ionized vacancy acceptor [26] that produce a self-diffusivity between 808 and 1177 K that is completely out of contact with the operational indications of Ge. However this impurity diffusion process is necessary to achieve high purities in Ge detectors.

2.1.3 Junction biasing

A *pn* junction at electric equilibrium is purely characterized by its depletion region where there is no available charge carriers and by the contact potential. The second depends upon the dopant concentration on the semiconductor, the higher dopant presence the larger contact potential. This, in fact, occurs since position of the Fermi levels changes because of higher dopant concentration pushes the Fermi level closer to the valence or conduction band. To control externally this effect, the junction can be biased by connecting it to an external potential. There are two ways to perform

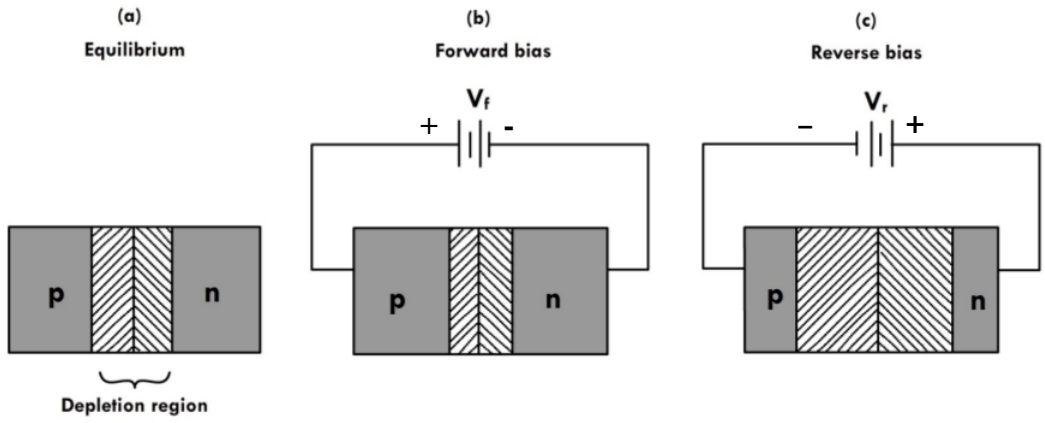

Figure 2.4: *pn* junction under (a) equilibrium, (b) forward and (c) reverse bias. The depletion width shrinks in forward bias and expands in reverse bias [11]

it, that can either increase or decrease the depletion zone.

Forward bias

When the p side is connected to the positive terminal of an external power source and the n side to the negative terminal, then it is said to be a *Forward bias*. Under this configuration, the external potential opposes the contact potential. Hence, the effective potential at the junction will be lowered. The application of the external potential, in forward bias, shifts the n side up with respect to the p side. This leads to a lowering of the barrier for injection of electrons from the n to the p side.

Reverse bias

In reverse bias, the applied external potential is in the same direction as the contact potential. The p side is connected to the negative terminal and the n side to the positive terminal. This causes the depletion region width to increase since the majority carriers are attracted to the external potential, as shown in figure 2.4c. In the energy band diagram the Fermi levels are shifted. Unlike the forward bias case, because of the higher barrier, diffusion current is negligible in reverse bias. There is however a small current that flows through the *pn* junction, called the reverse saturation current.

This current independent of reverse bias voltage and is generated by drift of the thermally generated carriers in the depletion region. Electron and holes dynamically generated in the depletion region get accelerated towards the n and p side due to the applied voltage and this leads to a small reverse saturation current, also called drift current.

2.2 Radiation interaction with real semiconductor detector

Each of the interaction mechanisms discussed in chapter one have as a final result the energy result in the transfer of energy from the gamma-ray to electrons, or, in the case of pair production, to an electron and a positron. The complete range of transferred energy extends from zero energy to the full energy of incoming gamma-ray. The expected number of pairs, N_p, can be computed as:

$$N_p = E_e/\varepsilon, \tag{2.3}$$

where E_e is the transferred energy and ε is the energy needed to create an ion pair, that is 2.96 eV for Germanium [3]. By multiplying this quantity to the unitary charge (electron) we can determine the charge of the electrical current displaced through the material, and hence the intensity of the signal. The most important feature of this relationship is the proportionality between the deposited energy and the detector signal.

To determine the relative amplitude of events per deposited energy in a semiconductor detector for each interaction mechanism in an actual energy spectrum, it is necessary to take into account the geometry and size of detector. Both the full and partial energy absorption named Compton edge and photopeak in energy spectra have relative amplitudes that depend upon detector size. For a hypothetical small detector, defined as to be the one that let only one scattering event to happen, only photoelectric interactions are able to produce the full energy absorption. On the other hand Compton scattering events will produce only a single recoil electron carrying a fraction of the gamma-ray energy. The scattered gamma-ray will escape from the detector and will carry the remaining energy. This will produce a distribution that spreads from zero values to the Compton edge.

Therefore, the interaction of γ-rays with a small semiconductor detector produces a hit distribution with greater weight in Compton region and with an existing, but reduced photopeak amplitude. Also, if the photon energy is greater than two times the mass of the electron, the amount of energy absorbed due to pair production is bounded by the energy in excess of the electron–positron rest masses. In a small detector the loss of energy absorbed caused by the escape of the annihilation γ-rays gives rise to a double escape peak. It is called double since both 511 keV annihilation photons produced in secondary interactions escape from the detector. This peak is located 1022 keV below the position of full energy absorption, just as shown in figure 2.5 (a).

On the other hand, if the sensitive detector volume is large then every γ-ray will have the opportunity to interact by one or other of the three discussed processes. If the interaction occurs through photoelectric effect then there will be a complete absorption of gamma-ray energy through release of photo-electrons and Auger electrons.

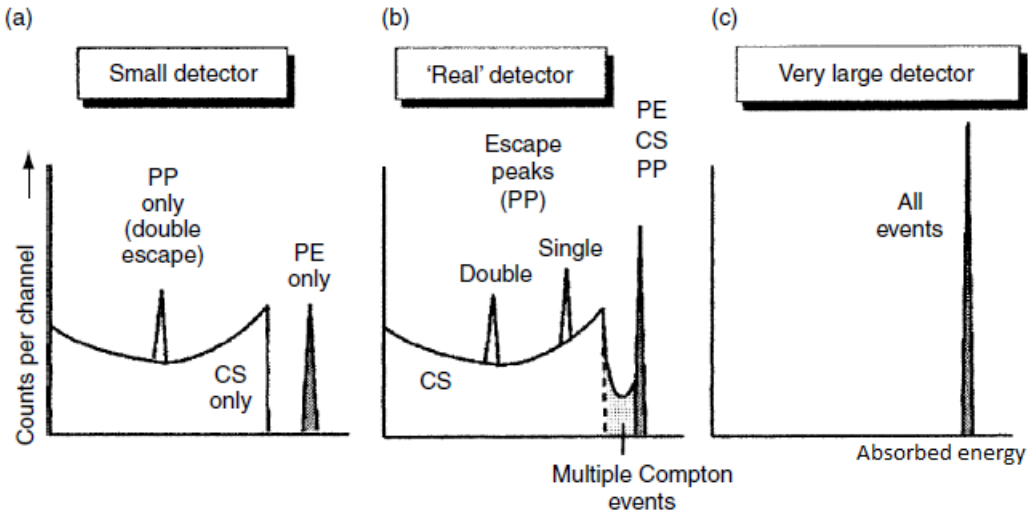

Figure 2.5: Energy spectra expected from semiconductor detectors of different sizes. The larger the detector, the higher the proportion of events resulting in full energy absorption: PE, photoelectric effect; CS, Compton scattering; PP, pair production [4]

Otherwise, if the photon interacts through Compton scattering then the recoiling photon will have the opportunity to interact once more and so on due to the largeness of the detector. Every interaction will release a recoiling electron that will transfer its energy. After several scattering events the photon energy will be so low that photoelectric will be inevitable and hence a full absorption of the remaining energy. Once more the complete photon energy is transferred to the detector with a constant resolution.

In a similar way there is a complete energy absorption when the primary photon interacts through pair production. In this case, the energy is equally distributed in the electron and the positron. Both the electron and the positron will lose their energy by creating electron–hole pairs in the process. Once the positron reaches thermal energies, it will be annihilated by combination with an electron and releasing two photons that will transfer their energy through any interaction mechanism. This produces energy spectra that are completely distributed in the full energy photopeak, as shown in figure 2.5 (c).

Both cases have been discussed to illustrate the actual importance of the dimensions of a semiconductor detector and the way they completely determine the relative amplitude of the photopeak and the Compton edge. Therefore, a real case in situated between both extremes. Besides that the mentioned processes happened with a smaller probability, there are another possibilities. These are:

1. **Multiple Compton events:** They are produced when a Compton scattering is followed by one or more further Compton events before the original scattered γ-ray escapes from the detector and each consecutive event absorbing a little

more of the γ-ray energy. If the initial Compton occurs at an energy near the Compton edge then the multiple Compton events would appear in the spectrum between the Compton edge and the full energy peak.

2. **Single escape peak:** If the energy of the incoming photon is greater than 1022 keV pair production is possible. After annihilation of the positron, if only one of the releasing photons escapes while the other is completely absorbed, then 511 keV will be lost from the detector. This will result in a separate peak in the energy spectrum representing the lost energy.

The actual signal of a real detector is a mixture of the previous features and the so discussed photopeak, Compton edge and double escape peak. Figure 2.5 (b) shows the comparison between the three cases.

2.2.1 Ideal semiconductor detectors

After a review of semiconductor properties, the features for an ideal semiconductor detector summarize as follows:

- High atomic number: to have as large an absorption coefficient as possible.
- Provide as many electron–hole pairs as possible per unit energy.
- Allow good electron and hole mobility.
- Be available in high purity as near perfect single crystals.
- Be available in reasonable amounts at reasonable cost

These features leaves two options for a good semiconductor detector: Silicon (Si) and Germanium (Ge). Both are high atomic atoms but in what leave them as good candidates in front of other materials are their low average energy spent by the charged particle to produce a single electron-hole pair. This quantity is much larger than the bandgap for these materials and it depends on temperature as shown in table 2.2.1. Germanium is the most obvious candidate because of the efforts put into the preparation of high purity material for the electronics industry, is readily available at reasonable cost. Nevertheless it is only used for the measurement of low-energy photons due to its low atomic number. To obtain a general scope in the range of high energy gamma rays, it is suitable to choose Germanium detectors with low concentration of impurities.

2.3 High Purity Germanium Detectors

2.3.1 Manufacturing

High purity germanium crystal, HPGe henceforth, are semiconductor diodes having a p-I-n structure in which the intrinsic region is sensitive to ionizing radiation, particularly X-rays and gamma rays, just as explained above. As discussed previously, in

Material	Bandgap [eV]		Energy per electron-hole pair [eV]	
	300 K	0 K	300 K	77 K
Si	1.11	1.16	3.62	3.79
Ge	0.66	0.74	-	2.96

Table 2.1: Average energy per electron-hole pair for Silicon and Germanium [2]

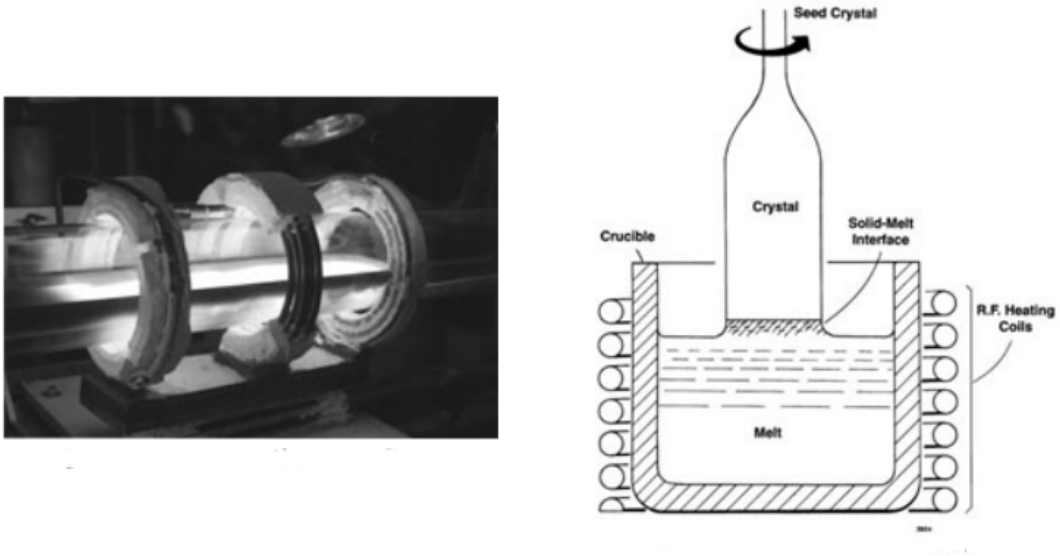

Figure 2.6: (a) Three coil zone refine. (b) Growth of High purity Germanium [36]

order to enhance the depletion region in a semiconductor detector it is necessary to reduce the number of impurities. HPGe detectors are highly purified with a technique known as *zone refining* where the germanium is melted in a crucible by using radio frequency (RF) heating coils, see figure 2.6 (a).

The underlying principle is that melting process set a side concentrated impurity atoms in liquid region, this occurs since the ratio of an impurity in the solid phase to that in the liquid phase is usually less than one. Therefore, at the solid/liquid boundary. Then the solid region remains purer than the original melt, once the liquid freezes a high purity solid arises. Each RF coil melt a small section of Germanium crystal inside a crucible, just as shown in picture 2.6. As the RF is slowly displaced along the length of the crucible the molted section moves with them. Thus, the germanium melts as the coil approaches and freezes as the coil moves away. In this manner, the impurities are swept to one end and this leads to a low concentration of impurities in the Ge crystal. This process is repeated several times until the impurities are mostly concentrated at one end of the ingot. Finally the end full of impurities is taken away leaving a Ge crystal much purer than the original as shown in figure 2.6 (b). The reduction of impurities at the end of the process is about a factor 100-150, depending on the manufacturer.

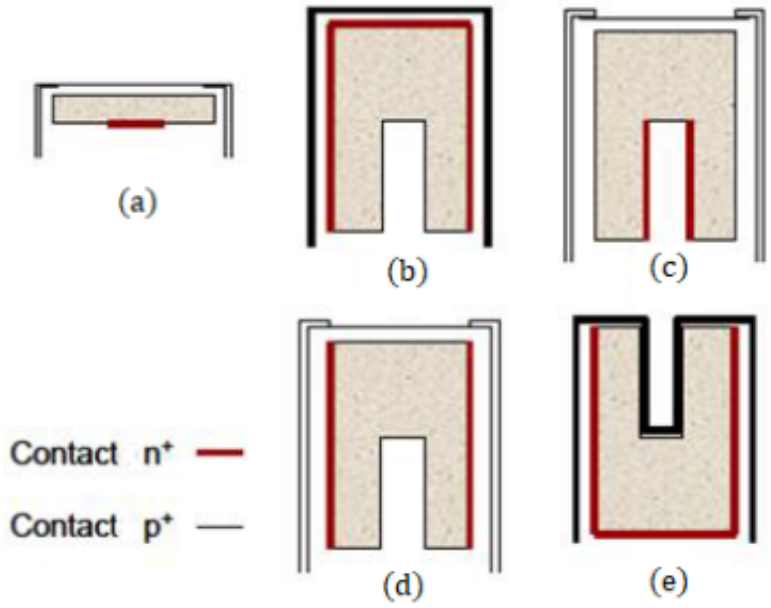

Figure 2.7: HPGe detector types: (a) **Planar** (P-Type), (b) **Coaxial** (P-Type), (c) **Reverse electrode Coaxial** (N-Type), (d) **Extended range coaxial** (P-Type), (e) **Well type** (N-Type) [35]

2.3.2 Coaxial HPGe Detectors

HPGe detectors can by manufactured with different geometries, which are established according to either the research focus or source geometry. The HPGe detector are mostly produced with a cylindrical geometry, nevertheless they are distinguished by its contact arrangement in its inner and outer surfaces. This feature mostly determines if the detector is P or N-Type, as shown in figure 2.7. Such arrangements offer a wide variety of options in energy range, efficiency and detection times.

The crystal thickness required for an efficient detection of photons with an energy up to MeV is about 5 cm for Germanium. In order to produce a detector with a large depletion depth under such specifications a cylindrical coaxial geometry must be used. In this configuration one electrode is fabricated at the outer surface of a cylindrical crystal and the other is located at the inner surface of the central hole. Under this arrangement larger depletion volumes can be achieved.

The most common type of HPGe detector are those with a close-ended configuration. They are characterized for having only part of its central core removed and the outer electrode is extended over one flat side surface. For coaxial detectors, the P-N junction can be located either in the inner or the outer surface. In the former case the depletion region grows outward. For a junction located in the outer surface the depletion region extends inward as the high voltage bias is increased until the crystal

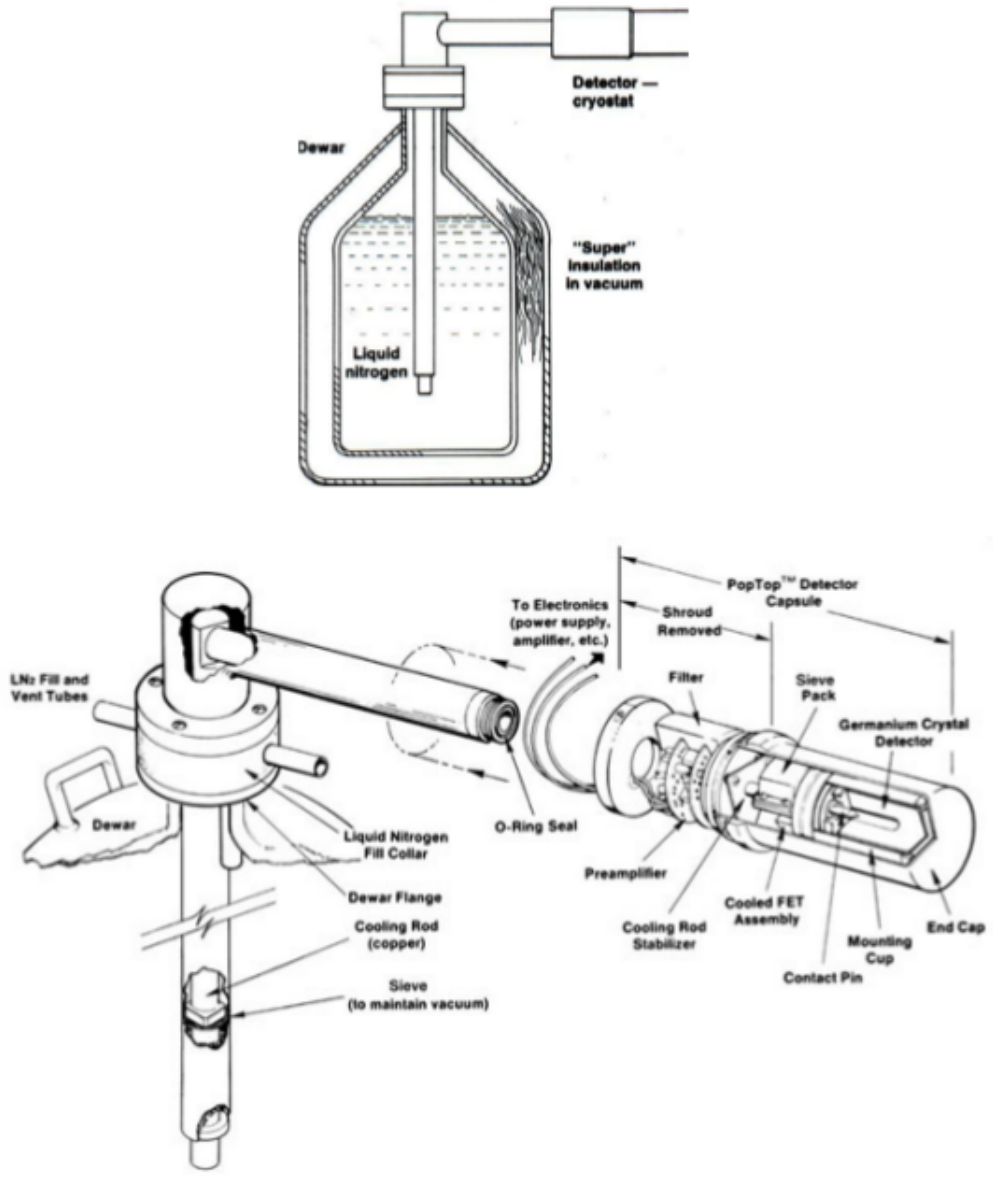

Figure 2.8: Standard inner geometry of cryostat, electronics, cooling system and Nitrogen Dewar container for vertical HPGe detectors [35]

is fully depleted. For this reason it requires a much lower full depletion bias, therefore it is preferred in practice.

To obtain a p-n junction at the outer surface, the n^+ contact is performed over the outer surface for a p-type detector while the p^+ contact is applied in case of an n-type crystal. The n-type coaxial detectors are often called reverse electrode detectors. Regardless its configuration, coaxial detectors are used for general gamma-ray spectroscopy purposes. They cover a wide range from below 100 keV up to 10 MeV. The only distinction between both crystal types lies on the dead layer thickness,

that of n-type is thinner than that of p-type, then n-type is more used for low energy spectroscopy.

Semiconductor detectors such as Silicon can be operated normally at room temperature, nevertheless it is not the case for Germanium detectors due to the small band gap energy. This allows electrons in valence band to jump to conduction band only by thermal vibrations, hence crystal must be cooled to avoid that leakage currents dirt the actual signal. HPGe detectors are allowed to warm to room temperature when they are not in operation, however, they are always maintained at LN_2 temperature when measuring to ensure that crystal will not be compromised.

As shown in figure 2.8, the Ge crystal is encapsulated in a vacuum tight metal container, called *cryostat*, in order to reduce thermal conduction between air and the Ge crystal. The main function of the cryostat is to cool the Ge crystal to suppress thermal vibrations. The Ge detector preamplifier is usually part of the cryostat, so they should be located as close as possible so that the overall capacitance can be minimized. Both the Ge crystal and preamplifier assembly are cooled and maintained by the cryostat under high vacuum for both thermal insulation and protection of the internal components from contamination.

In order to reduce photon scattering, cryostat materials must be as low atomic number (Z) as possible. Some candidates that accomplish such requirement are Aluminium ($Z = 13$), Magnesium ($Z = 12$), Beryllium ($Z = 4$), Teflon, and Mylar. In practice Aluminium is mostly used. The cryostat is cooled through a finger that is in contact with liquid nitrogen contained in a Dewar, just as shown in figure 2.8. There are various types of dewars so that the detection geometry can be selected depending on the application. For general radioactive or neutron-activated samples, the vertical type is widely used. For in-beam spectroscopic purposes, either the horizontal or side-looking type is more convenient. Portable dewars are also available for outside field measurements. Since this project is oriented to determine the existence of radioactive isotopes in products for human consumption and to calculate their respective activity, we will focus on vertical type.

2.3.3 Energy resolution

The most important characteristic of HPGe detectors is their excellent energy resolution. In Figure 2.9, two spectra from an HPGe and a NaI(Tl) are compared for a ^{60}Co source. The great superiority of the HPGe detector allows the separation of many closely spaced gamma lines, which is very beneficial for measuring multi-gamma emitting radioactive sources, especially when it comes to fine structure distinctions.

So far we have discuss the features and specifications for semiconductor detectors. It has become apparent that HPGe detectors have an extensive amount of advantages for spectroscopy purposes. Such features can be summarized as follows:

- **Higher atomic number**. Germanium is preferred due to its atomic number being much higher than silicon and which increases the probability of gamma

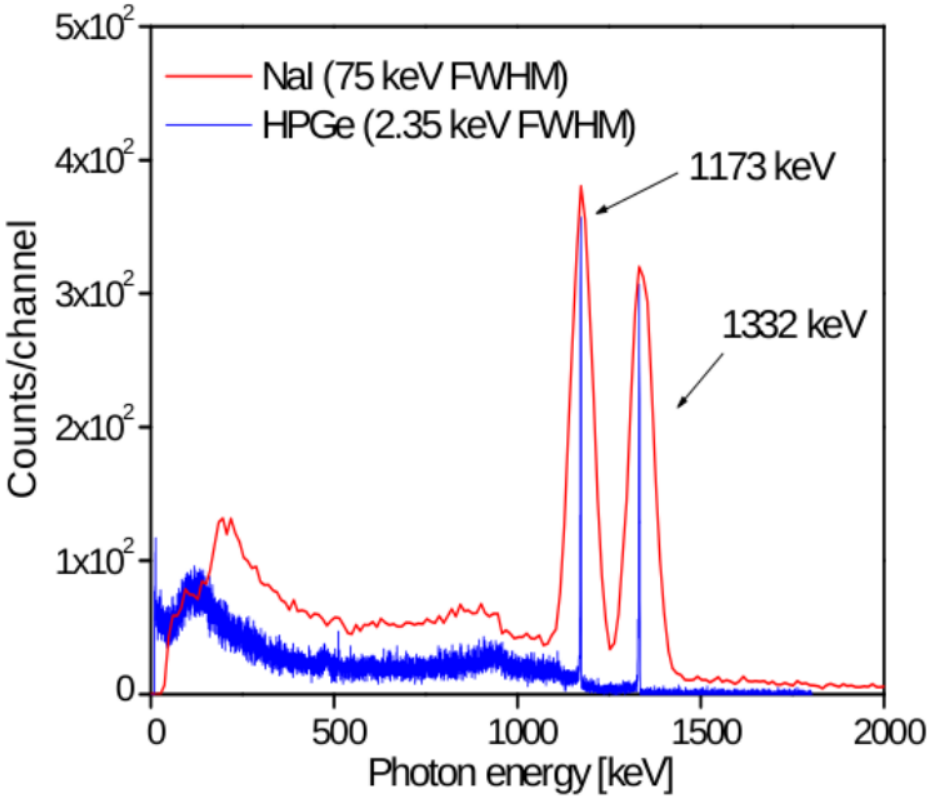

Figure 2.9: Comparison of NaI(Tl) and HPGe detectors spectra for ^{60}Co [7]

ray interaction.

- **Low pair energy**. Germanium has lower average energy necessary to create an electron-hole pair, which is 3.6 eV for silicon and 2.9 eV for germanium.
- **Very good energy resolution**. The FWHM for germanium detectors is a function of energy. For a 1.3 MeV photon, the FWHM is 2.1 keV, which is very low.
- **Large Crystals**. While silicon-based detectors cannot be thicker than a few millimeters, germanium can have a depleted, sensitive thickness of centimeters, and therefore can be used as a total absorption detector for gamma rays up to few MeV.
- **Wide energy range**. Germanium electronic configuration allows detector to register accounts from keV up to few hundred MeV, that is enough to observe γ-rays from radioactive sources.

2.3.4 Dead layer

Every semiconductor detector has a undepleted region, close to the outer surface which is completely inert, this region is known as dead layer. Since it is considered

in the net volume of the crystal, then it has effect on the performance of the detector because of the sensitive volume is reduced. For coaxial detector this effect is sharpened. This is because the dead layer completely surrounds the sensitive volume so the photon has to go through it before entering the detector's active volume.

Coaxial vertical HPGe detectors are characterized for having a lithium layer at the outer surface to strengthen the p contact. A time dependence of the Li-layer thickness has been studied due to the continuous diffusion of the lithium atoms inside the germanium crystal with mechanisms such as *kick-out* and *vacancy mechanism* [24]. This has an important role in the dead layer thickness since the Li atoms must pass through the dead layer and some of they push the impurities in the active volume leaving a larger inert region. For this effect to become particularly pronounced HPGe detectors must keep at room temperature for several years [17] and also it could be affected by the impurity distribution inside the germanium so that lithium atoms could migrate in a non-uniform way.

On the other hand, if the vacuum, where the sensitive crystal is located, deteriorates then the outer layer can react with air molecules or impurities make the dead layer grow inert. These are causes of temporary deterioration of the detector. There is no definitive guide to determine the current deterioration status of a detector since it is determined by its age, manufacturing process and the external conditions in which it is normally operated. As we will see in the next chapter, the increase in the thickness of the dead layer affects the detection efficiency. The use of simulations helps to validate the internal geometry of the detector and to quantify the effect of dead layer on detection efficiency, this will be explored in chapter four.

Besides the effect on the sensitive volume of the HPGe detector, the dead layer growth also affects the operating voltage. When reducing the active volume the electric field within the dielectric material (Ge) reduces so the operating voltage must be adjusted to keep magnitude of the electric field as when the detector was new. A simple approximation can be calculated by considering an arrangement of two coaxial cylinders filled by Ge as dielectric material. The well known capacitance per length unit of such arrangement is

$$C = \frac{2\pi\varepsilon}{\ln\left(\frac{b}{a}\right)}, \tag{2.4}$$

where a and b are the inner and outer radii respectively and ε is the dielectric constant. If the outer radius decreases an amount δ, that is the dead layer growth, then the ratio $\Delta V/C$ must remain in order to keep the same magnitude of electric field. By considering lengths of ICN-HPGe detector introduced in the following chapter $b = 24$ mm, $a = 4.8$ mm and a suggested dead layer growth $\delta = 0.4$ mm by [18] in a 30 yr period of time an increase of 30 V in operating voltage has been estimated. However this projects does not aim to delve into said account since the measurements have been performed at the same period of time.

2.4 HPGe detectors in High Energy Experiments

Besides the numerous applications that HPGe features provide in spectroscopy and nuclear physics, they are useful in high energy physics experiments. This is particularly true in dark matter (DM) and neutrino experiments, where a ultra-low background is mandatory since the signals produced by direct or indirect neutrino interactions are usually tenuous. Hence, their infrastructure must not contain fabrication materials with a high concentrations of radioactive chain elements such as ^{238}U, ^{232}Th and ^{40}K.

2.4.1 Ultra-low background experiments

A clear example is provided by SNOLAB experiments [27] which are mainly focused on the study of neutrino intrinsic properties. Such case is SNO+ experiment, which consists on a 12 m diameter acrylic sphere filled with 800 tonnes of liquid scintillator which floats in a water bath. This experimental setup detects Cherenkov radiation produced when the neutrino beam interacts with outer electronic shells of the liquid. This is performed through photomultiplier tubes (PMT) which are quite sensitive to radiation.

To perform high quality measurements, a complete counting system of Germanium detectors in needed to reduce radioactive contamination levels. The facility is located in the Vale Creighton Mine near Sudbury Ontario, Canada at 2 km underground. It consists on one Germanium detector manufactured by PGT in 1991 for low radioactive components and two HPGe detectors manufactured by Canberra. The former has an approximate sensitive crystal volume of 208 cm^3. The shielding that protects the crystal from room background is composed by an inner shell of 2 inches cooper and an outer shell of 8 inches lead. This shell configuration in the shielding achieves a low emission of X-rays, just as explained in chapter 1.

The two remaining detectors were manufactured by Canberra, one of them is p-type well detector and the second is p-type coaxial detector, the former is shown in figure 2.10. This project will study in detail the inner structure of the second type later. On the other hand, well-type detector is sensitive to gamma energies from 10 to 900 keV. The set of the three detectors cover a wide range of gamma energies and allows the facility to identify a large number of natural emitters in the fabrication materials of the experimental setup itself. For this detector tested mixed radionuclide samples with various geometries. In order to obtain the counting efficiency for such samples, a complete model of the detector and the sample whose activity is under measurement is modeled in Geant4 simulation toolkit. Finally, the experimental efficiency is corrected using the calculated results from the model. This method will be better understood throughout chapters 3 and 4.

An ultra-low background detector is expected to have less than 100 counts per year from all backgrounds combined. After a long search for natural emitters and that a combined background run of 3 months was completed, it was determined that

Figure 2.10: Canberra HPGe well-type detector: (a) Shielding and Nitrogen dewar horizontally arranged. (b) Detector sample chamber [22]

the combined backgrounds from the whole setup was at the level of about 30 counts per year.

A second case of HPGe detector facilities in high energy experiments can be found at Los Alamos Neutron Science Center. The Coherent Captain-Mills (CCM) experiment aims to probe the existence of sterile neutrinos and its relationship with the three active neutrinos from the Standard Model. Such probe would enhance the understanding in elementary particles and also would have a deep impact in Dark Matter and cosmology. In a similar way, CCM experiment works by detecting radiation through PMTs, therefore, low gamma-ray background is needed. For this realistic software replica of the entire experimental hall, including the neutron beam line, sample, detector supports and the walls of the experimental area has been implemented in simulations built in Geant4 in order to identify and subtract neutron emission background. In addition to this, to reduce gamma-ray natural background it has been proposed recently [30] to acquire a facility of germanium detectors to monitor the existence of natural emitters in the experiment arrangement.

2.4.2 Direct measurement with HPGe detector

A less common case is when the HPGe detector itself is used to discriminate between particles in order to identify the so-called weakly interacting massive particles (WIMP) that are thought to be a constituent of dark matter. Underground detectors of direct detection include two channels: A thermal channel which is based on the thermalization of photons and a ionization channel which is proportional to the number of carriers collected. Nevertheless, the so-called Luke-Neganov effect [23] affects properties of the detector due to the amplification of the photon signal by the electron (carrier) drift. Basically it describes that at high fields, the photon signal tends to grow linearly with the applied voltage. This proposes Germanium as possible candidate since it is good cryogenic bolometer.

Also, Germanium is nucleon rich, this should enhance interaction cross sections of

WIMPS with the detecting medium. If we consider the interaction of fast neutrons with Germanium, the elastic-scattering cross section is much higher than the inelastic cross section [28]. When the particle interacts with matter purely via ionization, as in the case for photons, the ratio of ionizing energy to the total energy is close to one, if no Luke-Neganov amplifying occurs. Therefore, this configuration can be used for particle discrimination [29]. For the WIMPS experiments, if we consider that these particles interact with the nuclei of the detecting media, this provides a way of discriminating the photons from other events. Both cases clarify the important role the HPGe detectors in HEP experiments, recalling that all the data analysis concerned is performed using high energy techniques.

Chapter 3

The ICN HPGe detector

In this chapter a full description of the experimental procedure used to determine the total efficiency as function of the incoming gamma-ray energy and the source-detector geometry is given. Starting from the geometry and inner specifications given by manufacturer of the HPGe detector, the basis of the experimental arrangement are laid. Some of the results obtained are highly important for the Monte Carlo simulation such as the resolution curve, discoursed bellow.

3.1 General features

The HPGe ICN detector was donated by Fermi National Accelerator Laboratory (FermiLab) to the *Instituto de Ciencias Nucleares* (ICN-UNAM) group working on the DAMIC and CONNIE [13] experiments to measure low radioactivity levels in extended sources. The package consists on the following components:

- **EG&G ORTEC brand high purity Germanium detector**

  Model: LD-31. Serial number: 80DC-5048. Working pressure: atmospheric. FermiLab serial number: 80DC-5048.

- **Dewar from Carbide Corporation.**

  Model number: CNHDS30-16195 CFG: SV. Serial number: 4034. FermiLab serial number: 123627.

- **CANBERRA brand lead shield**

  FermiLab serial number: 120297.

The detector was manufactured by AMETEK ORTEC which provides a compendium of outer dimensions and generic features of vertical coaxial type that are only for reference. Unfortunately, there is not detailed information of its inner parameters as well as the crystal sensitive volume since no technical sheet was provided by Fermilab. The specifications of the ICN-HPGe detector are shown in figure 3.1.

- High Purity Germanium of P-type and coaxial closed geometry.

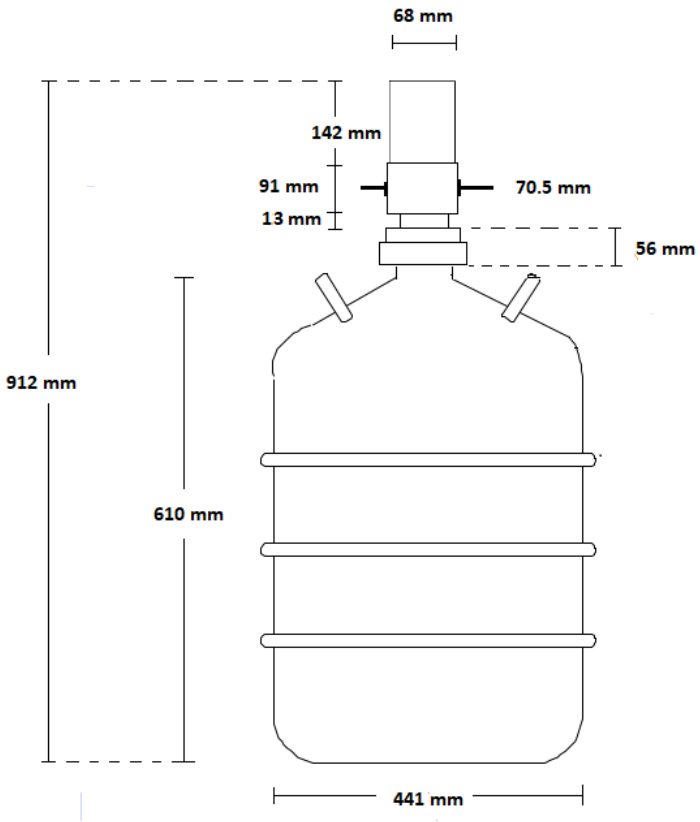

Figure 3.1: Dimensions of ICN-HPGe detector head and Dewar liquid nitrogen container.

- Model GEM30P4 with capsule POPTOP CFG-SV (Vertical cryostat, Dipstick type) and Dewar DWR-30.
- Outer contact of 700 μm diffused Lithium, inner contact of 0.3 μm Boron implanted ions, fiber carbon Endgap and a 1 mm Aluminium window in the upper face of the cryostat.
- Precision of 0.85 keV for low energy (up to 122 keV) and 1.85 keV at high energies (up to 1.33 MeV).
- Operating voltage of 3200 V with negative polarity.

Each feature has been explained in the previous chapter except for the Aluminium window. It has as a main function to allow low energy photon to interact with sensitive crystal.

3.1.1 Mounting

The liquid nitrogen in charge of cool the sensitive crystal, so that this reduce the thermal vibrations, is contained into a Aluminium dewar which has the standard structure

described in previous chapter. The ICN dewar has the following specifications:

- Dewar from the Union Carbide Corporation.
- Model: LD-31.
- Serial number: 80DC-5048.
- Operating pressure: atmospheric.
- Fermilab serial Number: NT11878.
- Storage capacity: 30 lt.

The dewar is filled and the cool finger of the detector is inserted within it. Once the detector is mounted it is left an approximate time of 5 hrs. so that the crystal is completely cryogenized at the established operating temperature of 77 K. The detector has several contacts, just three of them are relevant. A cable that is connected to the preamplifier, a second one that goes to the high voltage source and the last one works as output to a oscilloscope to monitor the signal. The closest dimensions and arrangement of the ICN-HPGe detector is shown in figure 3.1 that is a standard configuration provided by [35].

3.1.2 Shield

Besides the cryostat and the Dewar specifications, an important component of the experimental arrangement is the lead shield that protects the detector's head from outcoming radiation and hence reduces background in the actual signal. The ICN HPGe detector uses a Canberra shielding and it is composed by several shells, listed in table 3.1.2. Figure 3.3 shows the actual arrangement of the shells and its position with respect to the detector, this diagram was generated in the Geometry package of ROOT data analysis framework which is quite useful to check the geometry in a simulation.

Shell	Material	Width [mm]
1	Lead (Pb)	47.5
2	Copper (Cu)	1.6
3	Aluminium (Al)	1.4
4	Lead (Pb)	6.6

Table 3.1: Detector shielding shells: Materials and width.

The purpose of the shell structure has already been unveiled in chapter 1. The upper view of the shielding configuration is shown in figure 3.2a. Finally the whole experimental setup is shown in figure 3.2b.

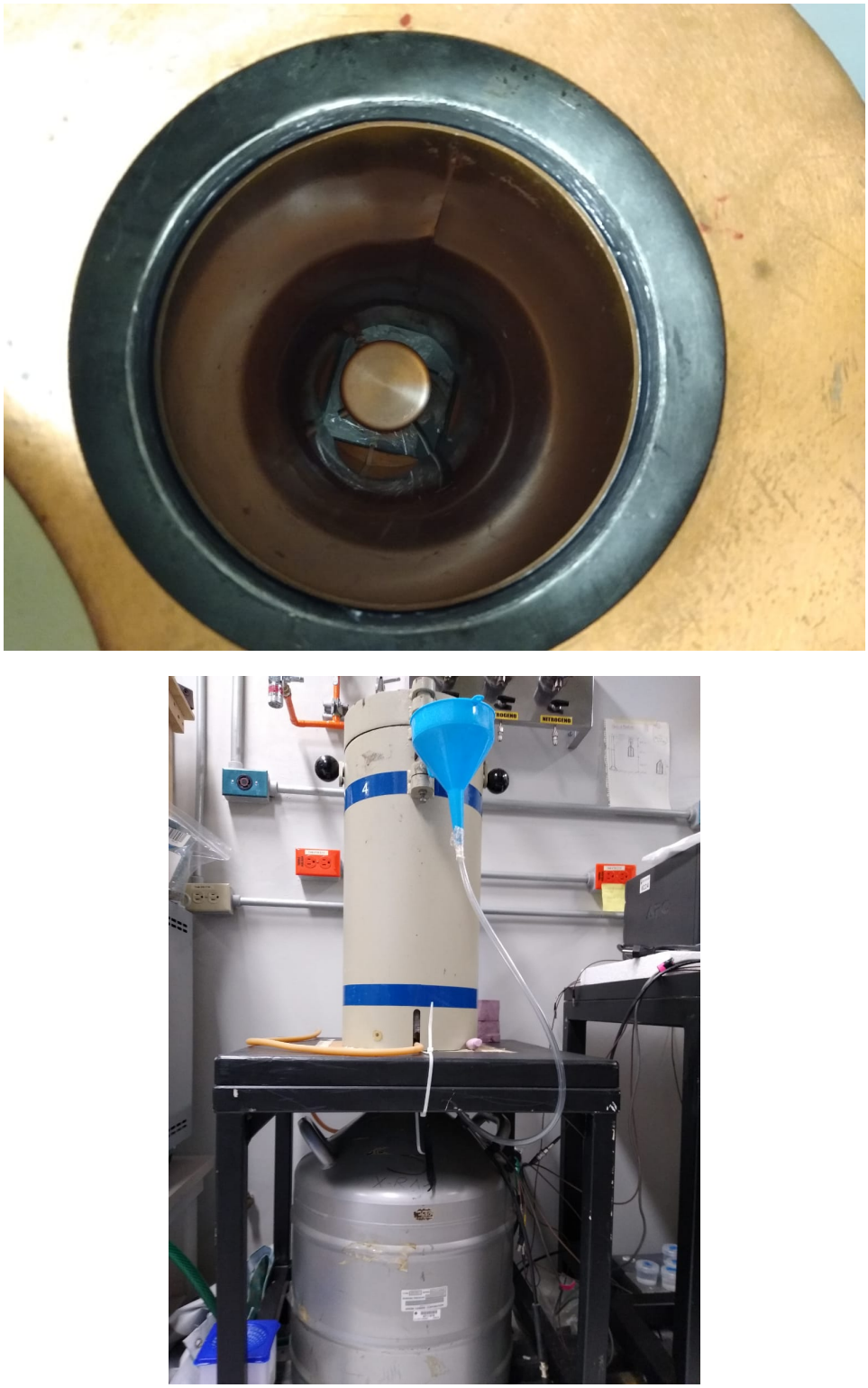

Figure 3.2: Experimental setup of ICN-UNAM HPGe detector: (a) Upper view of the cryostat head and the shells of the whole shielding. (b) Front view of the detector with shielding and Nitrogen Dewar installed.

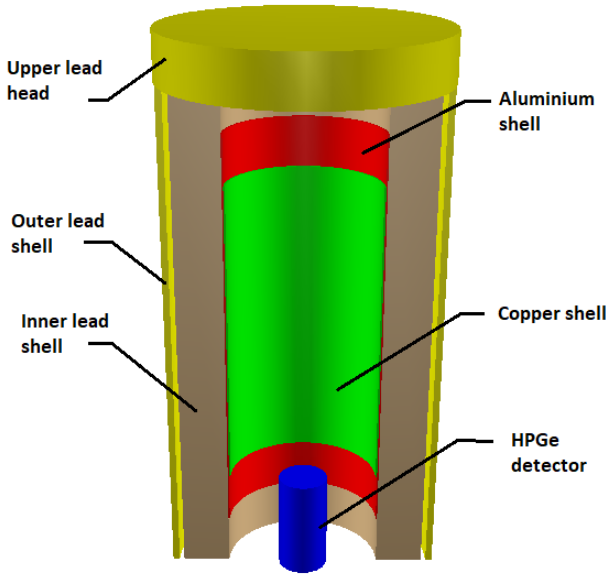

Figure 3.3: Shell arrangement of Canberra lead shield to cover HPGe detector from ICN.

3.2 PX5-HPGe Multichannel Analyzer

3.2.1 Specifications

The PX5-HPGe Multichannel Analyzer (MCA) [34] is a high performance digital pulse processor (DPP) and power supply module. It was designed to support semiconductor HPGe detectors and its main requirements are

1. High voltage bias exceeding the 1.5 kV limit of the standard PX5.
2. Preamplifiers built to the NIM standard so needing ± 12V DC and/or ± 24V DC.
3. Requiring precise cancellation of resistive tails in the 50 to 100 μs range.

This model of PX5 MCA are mostly used for spectroscopy with High purity germanium (HPGe) and lithium-drift silicon (Si(Li)) detectors, both cryogenically cooled, since both meet the listed requirements. The replacement of an analog system with digital technology improves several key parameters such as:

1. Better performance, specifically better resolution and higher count rates.
2. Greater flexibility since more configuration options are available, programmed through the software.

Figure 3.4: Front panel of the PX5-HPGe Multichannel Analyzer [34]

3. Improved stability and reproducibility.

To obtain a hit distribution, the DPP digitizes the detector preamplifier output, applies a real-time digital processing to the analog signal, detects the peak amplitude for each channel number, and bins this in its histogram memory. Finally, data set is then transmitted to the computer. The PX5 supports USB, RS232, Ethernet and the auxiliary connectors provide several additional inputs and outputs.

3.2.2 Control Panel

The items found in the frontal panel of the PX5-HPGe DPP are shown in picture 3.4. The main task of each of the components is listed below:

- **ON/OFF**: This switch turns the PX5 on and off. If it is hold for a longer time then 3 s then it will returns to the configuration settings that were in use when it was powered off, which includes turning on the preamplifier supplies.
- **HV POL** $\pm$: LED that indicates if the hardware jumper in the PX5 HV power supply is set to positive or negative.
- **HV FAULT**: LED that is actived when the "HV INH" (external voltage regulator with inhibit input) signal from the HPGe detector is disabling the HV power supply.
- **HV ON**: LED that is actived when there is actually high voltage at the HV output connector. Besides the case must be closed, for HV to be on:
  1. The HV must be commanded ON in software.
  2. The hardware polarity jumper and the software polarity setting must match.
  3. The HV Inhibit input must be inactive.
- **Connectors**: From front and rear, they deal with input and output signals respectively:
  1. Power Plug that mates with 3.5 mm x 1.3 mm x 9.5 mm female barrel: Connection to the main power source.

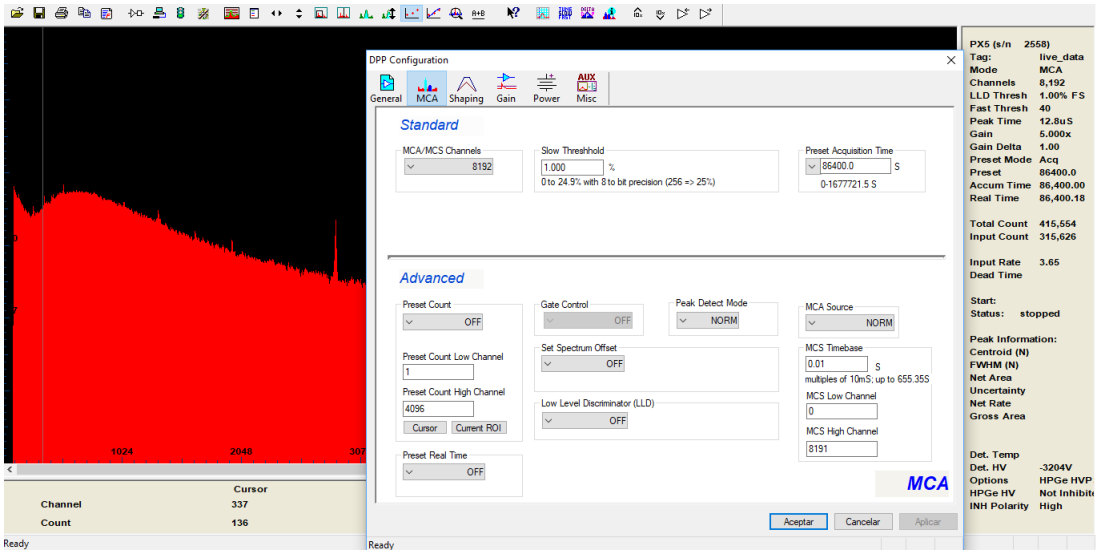

Figure 3.5: Screenshot of an actual session in the PX5 software window [34]

2. Standard USB jack: To store pre-defined configurations of gain, threshold and voltage.
3. Standard Ethernet connector: direct connection to the computer where the spectrum is displayed.
4. Standard BNC connector: Coaxial output to monitor the signal in an oscilloscope.
5. Preamplifier Power: power outlet for the detector preamplifier.

- **HV**: SHV output of the high voltage power supply.
- **HV INH**: BNC input to the HV power supply. The HV supply in the PX5 is shut down if this is active. The output from the HPGe becomes active if the detector gets warm.

The number of hits per bin are stored in an internal memory of multichannel analyzer and plotted in MCA software. A screenshot a PX5 software window is shown in figure 3.5, there the following items are found.

- An upper tool bar in panel which includes the following options:
  - Autopeak search option.
  - Tab to set the calibration parameters.
  - Histogram addition option.
  - Start/Pause histogram recording.
- A right panel which gives all the information of the current configuration of the MCA as well as the current recording.

- A lower panel which indicates the coordinates of the cursor. Useful for manual search for peaks.
- A configuration window to establish the recording setting with the following tabs:
  - MCA parameters such as Gain, Threshold (lower bin cut) and Preset acquisition time.
  - Shaping settings for Oscilloscope coincidence.
  - Power supply settings: voltage magnitude and polarity.

3.2.3 Operating voltage

The HPGe detector operates with a voltage of 3200 V with negative polarity. A custom power supply board is installed in a standard PX5-HPGe MCA, providing the high bias voltage needed by the HPGe detector as well as the voltage and current supply required by the preamplifier. The magnitude of the power supply can be commanded in software from about 50 to 5000 V DC and currents up to 30 μA. The output usually reads 3 $\pm$V when the HV supply is turned off, so it s stability is optimal for Ge detectors [34]. It has been possible to verify that the gain has remained stable, maintaining the environment around the sensitive crystal with low humidity and stable temperature.

As discussed in chapter 2, HPGe detectors show low increasing leakage current and electronic noise at temperatures above 110 K due to thermal vibrations. Such effects become evident in the detector resolution. On the other hand, operational temperatures below 40 K may result in deterioration in energy resolution due to trapping effects. In order to avoid them these effects, stable temperatures from 77 to 100 K must be reached to get an optimal operation. This is achieved by letting the detector's cooling rod in contact with LN2 for a minimum period of time of three hours, this will ensure that its cooling cycle finishes properly, this process takes from three to five hours. This project does not intend to treat with the use of the detector outside the temperature range, however some studies infer in the dependence of the operating voltage as well as the necessary preparations to operate germanium detectors at temperatures higher or lower than the customary temperature [21].

3.3 Detector response

3.3.1 Radioactive material

A set of radioactive sources manufactured by *Spectrum Techniques LLC* with the product tag RSS8UN were used to perform measurements. There are two models of this source set, one of them is for high precision spectroscopy while the second is for academic use. For this latter the sources have not been calibrated so there is a 20 % of uncertainty on the labeled activity [39]. Each source is constructed using a

polypropylene disk and its sizes are: 2.0 cm x 0.125 cm. Each of them have an initial activity of 1.0 μCi excepting the ^{137}Cs and ^{241}Am sources that have 0.1 μCi and 0.4 μCi respectively. For all sources, the fourth column reports the branching ratio, it measures the probability that the radionuclide decay in such channel that releases a photon of listed energy. This information was obtained from decays sheets of the National Laboratory Henri Becquerel [38].

Source	γ energy [keV]	Half-life [yr]	Branching ratio [%]
^{241}Am	59.54	432.2	0.776
^{133}Ba	53.16, 81.0	10.5	0.0214, 0.3331
^{133}Ba	276.0, 303.0, 356.0	10.5	0.0753, 0.191, 0.6363
^{57}Co	122.0, 136.0	0.745	0.855, 0.107
^{22}Na	511.0, 1275.0	2.6	1.8, 0.9994
^{137}Cs	662.0	30.1	0.9436
^{54}Mn	835.0	0.855	0.999
^{65}Zn	1115.0	0.668	0.5023
^{60}Co	1173.2, 1332.5	5.27	0.999, 0.999

Table 3.2: Radioactive sources specifications provided by *Spectrum Techniques LLC* [39]

First, natural background is recorded for long periods of time (24 hrs.) to reduce statistical fluctuations. Once it has been recorded, point sources are placed at a 25 cm distance above cryostat head, that has been chosen as a standard for vertical coaxial HPGe detector to reduce pile-up effect in photopeaks [16, 19]. The intrinsic parameters of the PX5 MCA such as Threshold, Gain and Preset Time has been set in such manner that obtained spectra can be analyzed in a range for 20 keV up to 1480 keV, which is enough to identify all the photopeaks of sources in table 3.3.1. The spectra is recorded for time intervals of 7200 s.

The actual shape of the signal in the oscilloscope both for the HPGe detector is shown in figure 3.6 top, here a ^{60}Co and a ^{137}Cs source were placed over the detector head. On the other hand, figure 3.6 bottom shows the signal of the pre-amplifier pulse, here a ^{60}Co source was placed to record the signal shape. For both signals, the energy spectrum is located at the left of the oscilloscope screen. Also from the cathode signal, it is possible to measure the rise time which goes from 0.8 to 1.4 μs.

3.3.2 Linearity

PX5 software also allows users to search photopeaks in measured spectrum, then it provides the mean and deviation of each. Alternatively, it can be done manually. By obtaining the mean let us know the number of channel where the photopeak is located. Essentially, a linear tendency is expected when comparing the photopeak energy with the number of channel. Figure 3.7 shows the energy as a function of the number of channel, here a straight line has been fitted to measured data as:

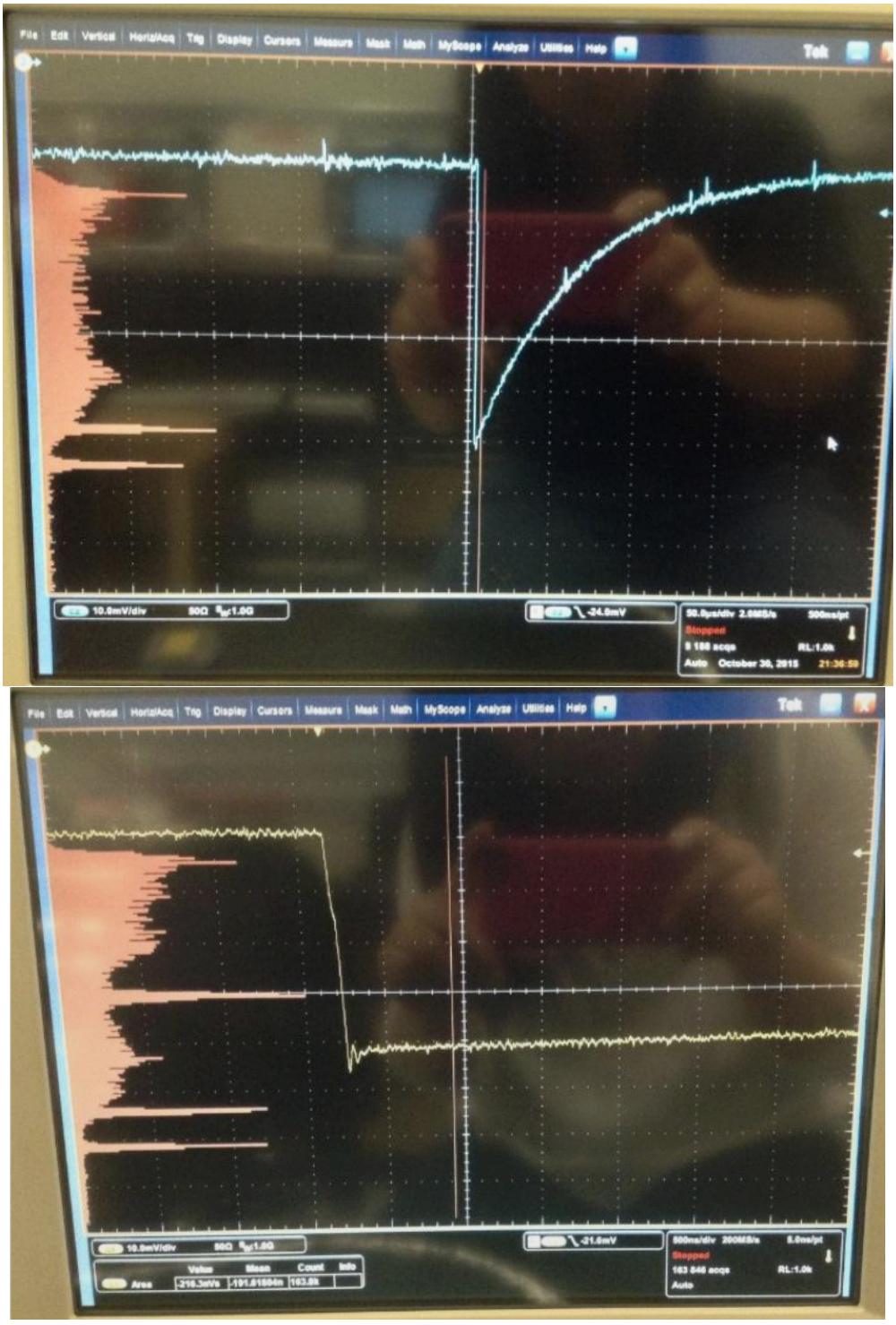

Figure 3.6: Pulse on the oscilloscope with values of 10.0 mV/div, 50.0 μs/div to 2.0 MS/s, 500 ns/pt. TOP: detector cathode signal of ^{60}Co and ^{137}Cs sources. BOTTOM: pre-amplifier signal of ^{60}Co source.

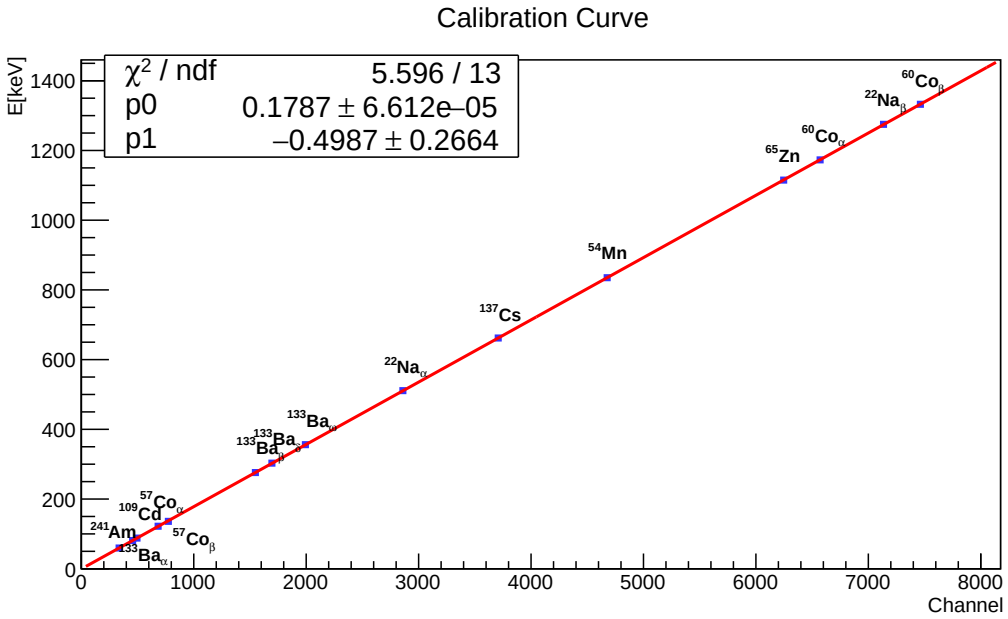

Figure 3.7: Calibration curve of the ICN HPGe detector.

$$E(N) = m \times N + b, \tag{3.1}$$

where E is the reconstructed energy and N the number of channel. Here, m and b are the fit parameters which are given by

$$m = (0.1786 \pm 0.0001)\text{keV/bin}, \quad b = (-0.498 \pm 0.266)\text{keV}. \tag{3.2}$$

A statistical error evidently of the same order of the central value for the parameter b, hence it suggests that it is feasible to set such parameter as zero. Under these considerations, equation 3.1 allow us to obtain hit distribution as function of deposited energy.

Once the calibration has been performed energy spectra, including background, can be analyzed. Firstly, by identifying the energy range of the photopeaks in background the isotopes in experimental setup are determined, see figure 3.8a. To perform this task, the program **histoGe** [41] is executed.

Figure 3.8b shows energy spectrum from ^{60}Co compared with background from the lead shield, meanwhile figure 3.9a shows the energy spectrum of point source with subtracted background. In both cases, ^{60}Co spectrum shows the main features discussed in chapter one: Compton continuum, Compton edge, photopeak and backscatter peak, this features are found in remaining spectra from the sources in table 3.3.1.

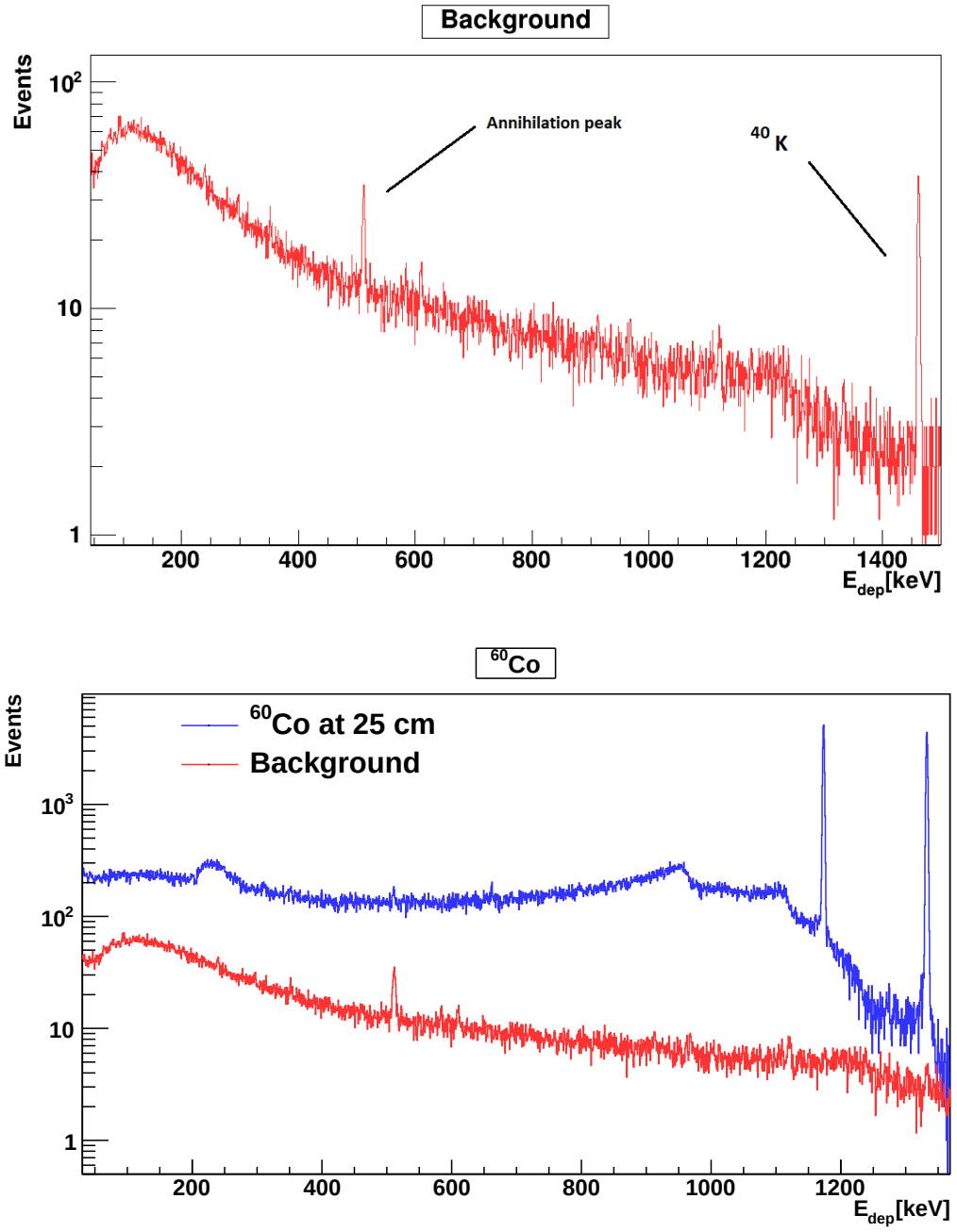

Figure 3.8: (a) HPGe detector background recorded for 24 hrs. in ICN facilities. (b) ^{60}Co spectrum taken at 25 cm frm ICN HPGe detector's head.

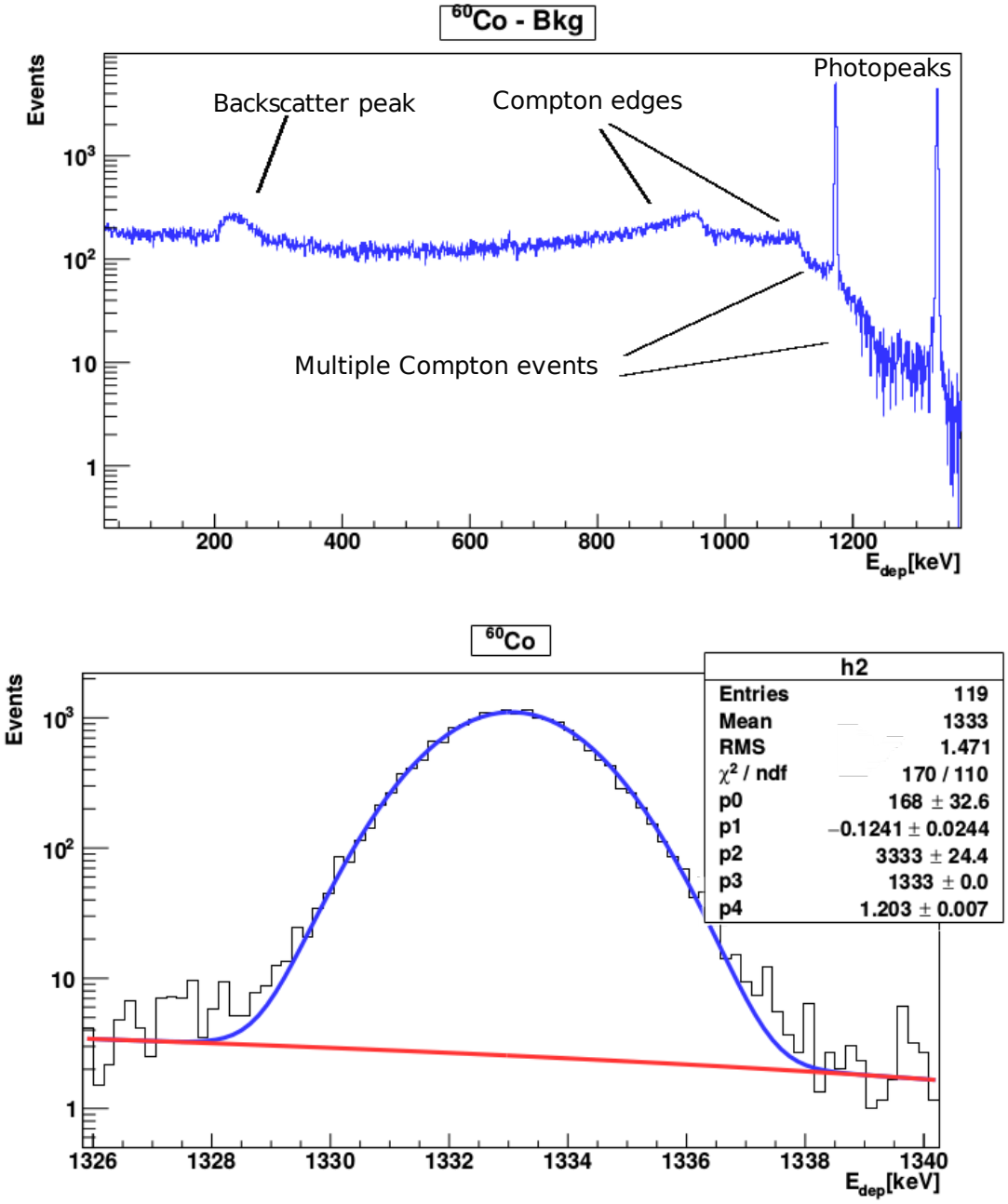

Figure 3.9: (a) Subtracted background energy ^{60}Co spectrum measured with the ICN HPGe detector. (b)Function model fitted to the hit distribution of the ^{60}Co spectrum about the gamma-ray energy 1333 keV. In blue color, the photopeak modeled as a Gaussian distribution function. In red color, the baseline modeled as a straight line.

Source	γ energy [keV]	Measured energy [keV]	FWHM [keV]	Resolution [%]
^{133}Ba	53.16	53.43 ± 1.85	1.533 ± 0.117	2.898 ± 0.446
^{241}Am	59.54	59.14 ± 0.96	1.575 ± 0.112	2.681 ± 0.525
^{133}Ba	80.99	81.09 ± 1.47	1.774 ± 0.124	2.152 ± 0.214
^{109}Cd	88.03	88.40 ± 1.42	2.694 ± 0.123	1.816 ± 0.299
^{57}Co	122.06	122.15 ± 2.37	1.544 ± 0.232	1.258 ± 0.175
^{57}Co	136.47	136.47 ± 1.95	1.529 ± 0.242	1.182 ± 0.198
^{133}Ba	276.39	276.16 ± 1.70	1.727 ± 0.184	0.623 ± 0.136
^{133}Ba	302.85	302.67 ± 1.52	1.791 ± 0.092	0.502 ± 0.089
^{133}Ba	356.01	355.71 ± 1.22	1.746 ± 0.136	0.491 ± 0.051
^{22}Na	511.0	510.60 ± 2.12	2.149 ± 0.167	0.421 ± 0.042
^{137}Cs	661.65	661.81 ± 2.56	2.435 ± 0.091	0.368 ± 0.035
^{54}Mn	834.84	835.34 ± 2.19	2.137 ± 0.085	0.254 ± 0.028
^{65}Zn	1115.53	1116.01 ± 2.11	2.237 ± 0.176	0.198 ± 0.026
^{60}Co	1173.22	1173.87 ± 2.87	2.786 ± 0.261	0.233 ± 0.015
^{22}Na	1274.5	1274.15 ± 1.51	2.726 ± 0.112	0.214 ± 0.012
^{60}Co	1332.49	1333.06 ± 2.28	2.826 ± 0.181	0.212 ± 0.011

Table 3.3: Radioactive sources specifications provided by *Spectrum Techniques LLC*.

3.3.3 Resolution

The most important characteristic of HPGe detectors is their excellent energy resolution. It is dimensionless magnitude and works as a measurement of the detector capability to define a energy level for each channel. The great superiority of the HPGe detector allows the separation of many closely spaced gamma lines, which is very beneficial for measuring multi-gamma emitting radioactive sources. Resolution at a photopeak is defined as

$$R = \frac{FWHM}{E}, \tag{3.3}$$

where E is the energy value of the photopeak and FWHM is the acronym for full width at half maximum and is related with the peak deviation, σ, through

$$FWHM = 2\sqrt{2\ln(2)}\sigma. \tag{3.4}$$

Once a measured spectrum is calibrated it is analyzed through a ROOT macro that performs the following tasks:

1. Identifies each photopeak and fit a Gaussian distribution mounted on a straight line that models the baseline and the multiple Compton events bellow the photopeak, see figure 3.10. This is performed by the least squares method.

2. Determines the central value of resolution with eqs. 3.3 and 3.4 by employing the mean and the deviation from the fitted Gaussian distribution.

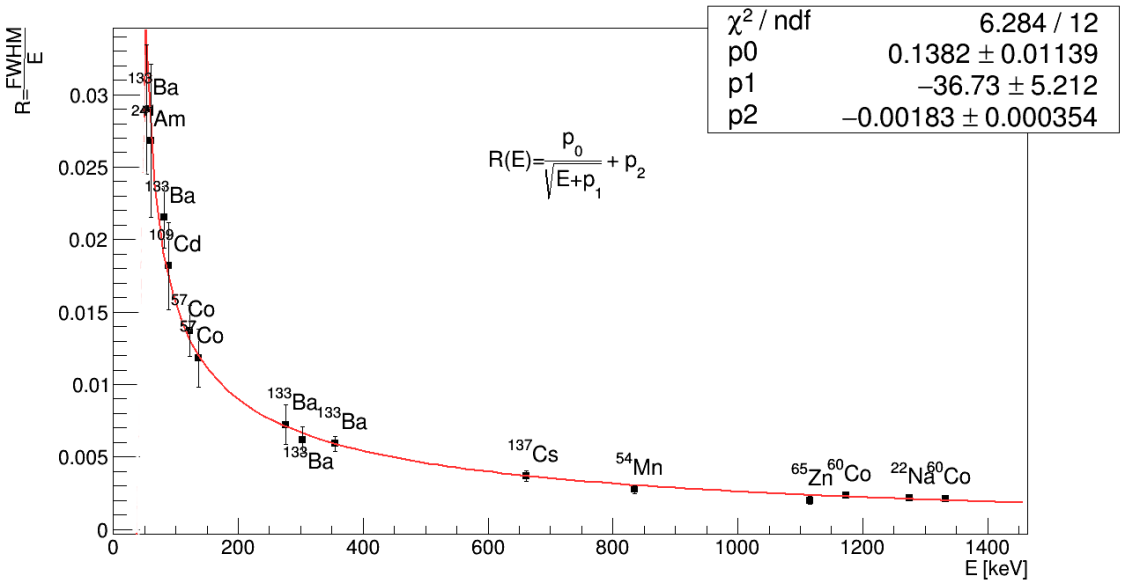

Figure 3.10: Resolution curve obtained with the HPGe detector and a set of radioactive sources from *Spectrum Techniques LLC*.

3. Considers the deviations of the mean and the bell width defined as [3]

$$\Delta\mu = \frac{\sigma_x}{\sqrt{N}}, \qquad \Delta\sigma = \frac{\sigma_x}{\sqrt{2(N-1)}}, \tag{3.5}$$

where σ_x is the standard deviation and N is the total number of counts. It determines the error of resolution value by a sum of squares of residual errors:

$$\Delta R^2 = R^2 \left[\left(\frac{\Delta\sigma}{\sigma} \right)^2 + \left(\frac{\Delta\mu}{\mu} \right)^2 \right] \tag{3.6}$$

4. Determines the total number of counts of full-energy peak, N_p, in a symmetrical radius interval of 6σ and subtracts the counts bellow the straight (baseline).

The results obtained for the whole set of radioactive sources is in table 3.3.3. Here, a function of energy with an expected inverse square root behavior has been fitted to the data set, which was proposed as,

$$R(E) = \frac{p_0}{\sqrt{E + p_1}} + p_2, \tag{3.7}$$

where p_0 and p_1 are fitting parameters. The fitted function is shown in figure 3.10. Such curve let us realize that the lower the energy resolution of the detector, the greater its ability to distinguish two radiations with very close energy. This is

very important to perform the total account in full width photopeak. This is such an important result since it let us interpolate the resolution values resulting from photon energies whose sources are not available.

3.4 Photopeak efficiency

3.4.1 Point sources experiment

The photopeak efficiency of a detector is defined as the ratio of the number of counts in full-energy peak ,N_p, to the number of photons emitted by the source with a certain energy (N_e), i.e,

$$\varepsilon_p = \frac{N_p}{N_e}. \tag{3.8}$$

As explained in chapter one, the shape of the photopeak depends upon the energy of the gamma-ray energy as well on the detector geometry, then ε_p inherits the dependency on such parameters. This become clear since ε_p can be factored into two parts: the intrinsic efficiency, ε_{int} and the geometrical efficiency or acceptance, ε_{geo}. The total efficiency is the product of both factors, i.e,

$$\varepsilon_p = \varepsilon_{int} \times \varepsilon_{geo}. \tag{3.9}$$

Here the intrinsic efficiency is defined to be the ratio of the total number of photons hitting the detector, N_t, to the number of photons emitted by the source:

$$\varepsilon_{int} = \frac{N_t}{N_e}. \tag{3.10}$$

On the other hand, the geometrical efficiency is defined to be ratio of the number of photons emitted towards the detector by the total number of photos. It can be expressed in term of the solid angle region when dealing with point sources. This translation is performed by considering the probability density function of a photon that is emitted in a particular direction $\rho(\Omega)$ and integrate over the solid angle covered up by the sensitive detector region. For isotropic a sources such density is uniform and is $(4\pi)^{-1}$.

$$\varepsilon_{geo} = \int_R \rho(\Omega) d\Omega = \int_R \frac{d\Omega}{4\pi} \tag{3.11}$$

For coaxial cylindrical detectors and when the point source is placed along its symmetry axis the integration region is simply determined by the radio of detector,r , and the distance between the source and the upper face of the crystal ,d , as shown

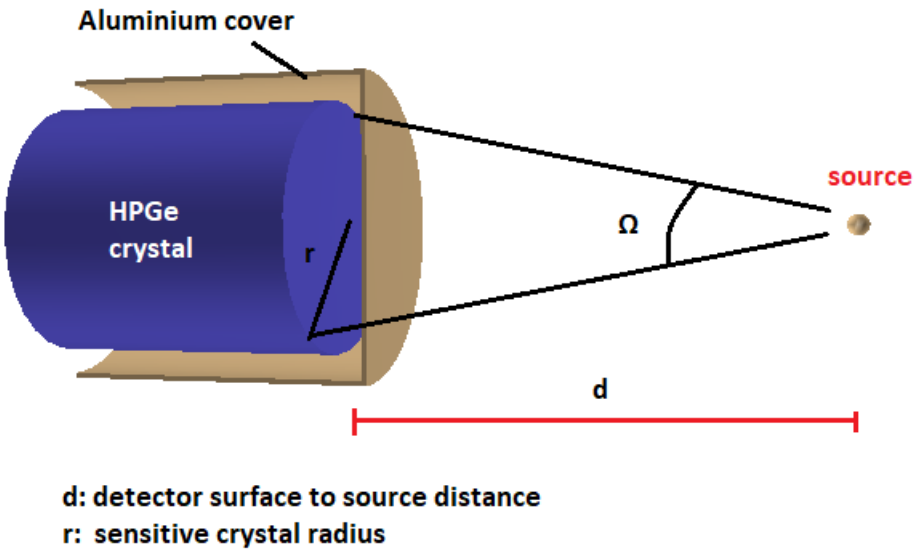

Figure 3.11: Source-HPGe detector geometry diagram.

in figure 3.11. To obtain a numerical result, the gap between the sensitive HPGe crystal and the Aluminum cryostat must be taken into account.

$$\varepsilon_{geo} = \frac{1}{2}\left(1 - \frac{d}{\sqrt{r^2 + d^2}}\right). \tag{3.12}$$

As described before the resolution, the mean peak energy among other parameters were obtained from the photopeak. Now to integrate the counts within full-energy photopeak the pile-up events from the Compton edge and background must subtracted. This is second stage of the macro written in ROOT mentioned in in section 3.3.2, to model such events as a straight line with negative slope and to subtract every count bellow it from the total sum of events to calculate N_p. The remaining quantity to determine is the total number of photons emitted by the source. Recalling the radioactive decay law, N_e can easily be computed using

$$N_e = I_\gamma T A_0 e^{-T/\tau}, \tag{3.13}$$

where A_0 is the initial activity, τ the half-life of the source, I_γ the branching ratio and T is the time exposure of the source. Since I_γ, τ and T are well measured parameters, the main uncertainty of 3.12 comes out the initial activity of the source

$$\Delta\varepsilon_{tot}^2 = \left(\frac{\partial\varepsilon_{tot}}{\partial A_0}\right)^2 \Delta A_0^2 = \varepsilon_{tot}^2 \left(\frac{\Delta A_0}{A_0}\right)^2. \tag{3.14}$$

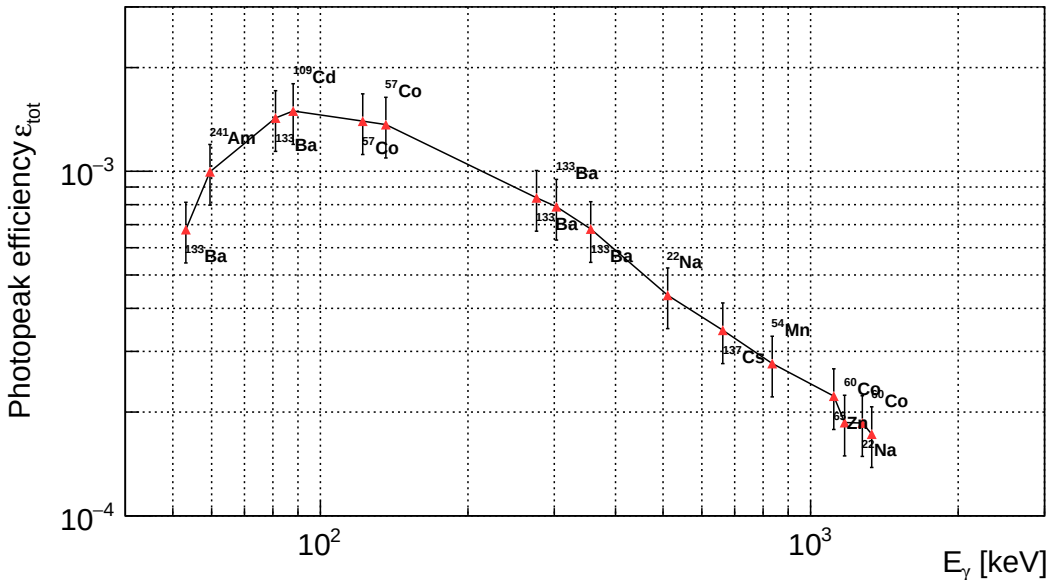

Figure 3.12: Absolute efficiency curve measured with *LLC Spectrum techniques* source kit in the ICN HPGe detector.

Figure 3.12 show the efficiency curve obtained with the whole set of sources. We have realized that this curve has the following features in log-log scale.

- Quasi-linear tendency with positive slope in [59, 122] keV range.
- Quasi-linear tendency with negative slope beyond 136.0 keV.
- Global maximum nearby 122 keV.

These features are expected [15] for well-type detectors in the intrinsic efficiency curve. Nevertheless, coaxial-type detectors seems to exhibit the same features with slight differences such as the energy for the maximum value which is shifted (about 100.0 keV). Therefore it becomes apparent that for HPGe symmetrical detectors, the efficiency curve behavior has a greater weight in the atomic and crystalline structure than in detector-source geometry.

3.5 Potassium salt experiment

3.5.1 Preparation of extended sources

The actual focus of spectroscopy is to deal with extended samples whose geometries could be varied and complex, as well as they can contain a wide variety of radioactive material. In most of the cases it is decided to dilute the sample in a sterile liquid in

Figure 3.13: Extended sample of diluted salt substitute in injectable solution into a polypropylene container placed at the top of the ICN HPGe detector's head.

order to ensure that the solution has a closely uniform of radioactive nuclei. If not the case, the solution is prepared taking into account two important issues considering both liquid and sample chemical composition. First, that does not exist a chemical reaction between the liquid and the sample, and to have complete knowledge and control of the radioactive nuclei in the liquid. This latter is to be able to safely subtract all components outside the sample in the background.

Besides these issues, the solution container chose is also important. Without going into details of the possible candidates, polypropylene raises as a highly used material to contain radioactive samples in spectroscopy. These are the main reasons:

- Its chemical properties mean it does not react with acids, therefore it let us dilute radioactive solutions within it.
- Highly resistant to corrosion and chemical leaking, this becomes useful to hold a radioactive solution for long exposure times to record energy spectra.
- It does not conduct electricity well, and so is classed as an insulator, hence there is no a leaking signal risk.
- It is low density, then all the outgoing radiation coming from the container interior will lose a minimal amount of its energy.

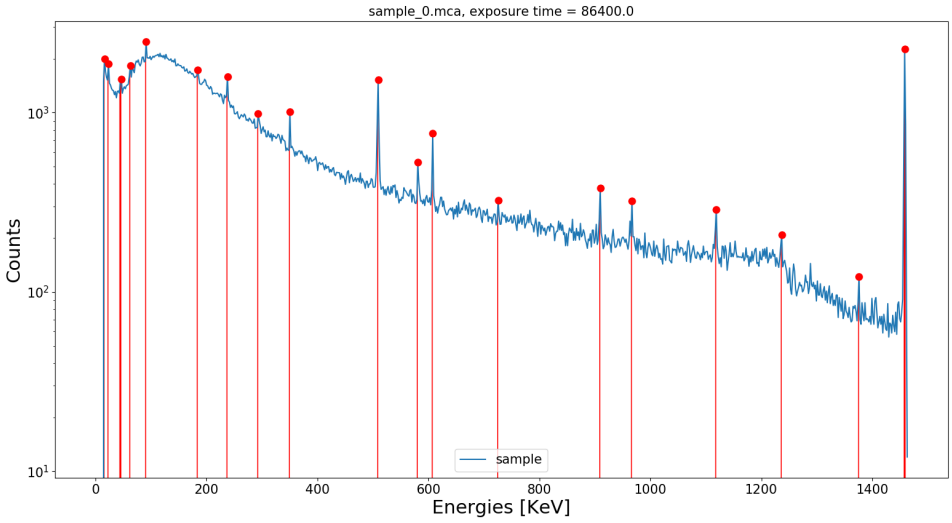

Figure 3.14: Peak search of the recorded background of injectable solution water in polypropylene container performed with **histoGe** code [41]

3.5.2 ^{40}K photopeak counting

So far, we have briefly introduced the general scope of spectroscopy. Now we focus on determining the concentration of radioactive isotopes in common objects such as potassium salt. This objective will be divided into two tasks, the current is to determine the energy of released radiation and to determine the number of hits in full-width photopeak per potassium salt gram. Latter the purpose of simulated absolute efficiency curve in such objective will be elucidated.

Potassium salt brand Novoxal with a 59% purity was chosen to perform this measurements. For this, a set of solutions were prepared in clinical polypropylene containers with 4.75 cm. diameter, 4.42 cm. height, 0.9 mm. width and a capacity of 50 ml. Several concentration percentages of salt were considered. Samples of 2, 4, 6, 8 and 10 g. were diluted in Pisa brand injectable water solution which reports on label a slight concentration of Potassium. Since we focus on determining ^{40}K concentration per gram in potassium salt, then the background subtraction will be important.

By placing the diluted sample right on the cryostat head, long spectra is recorded. The acquisition time is set as 24 h. since a small statistical fluctuation in both background and samples spectra. The background is shown in figure 3.14, it was recorded by placing a container with no diluted salt in liquid. Several gamma lines are identified background spectrum of both cases. Once more the program **histoGe** [41] which uses a data base of radioactive decays has been used to perform the peak identification. Here we find the relevant photopeak at 1460 keV energy that corresponds to ^{40}K besides those isotopes found in the experimental setup background. This let us realize that, effectively the injectable liquid solution has a concentration of such isotope, which at this point is unknown through experimental methods.

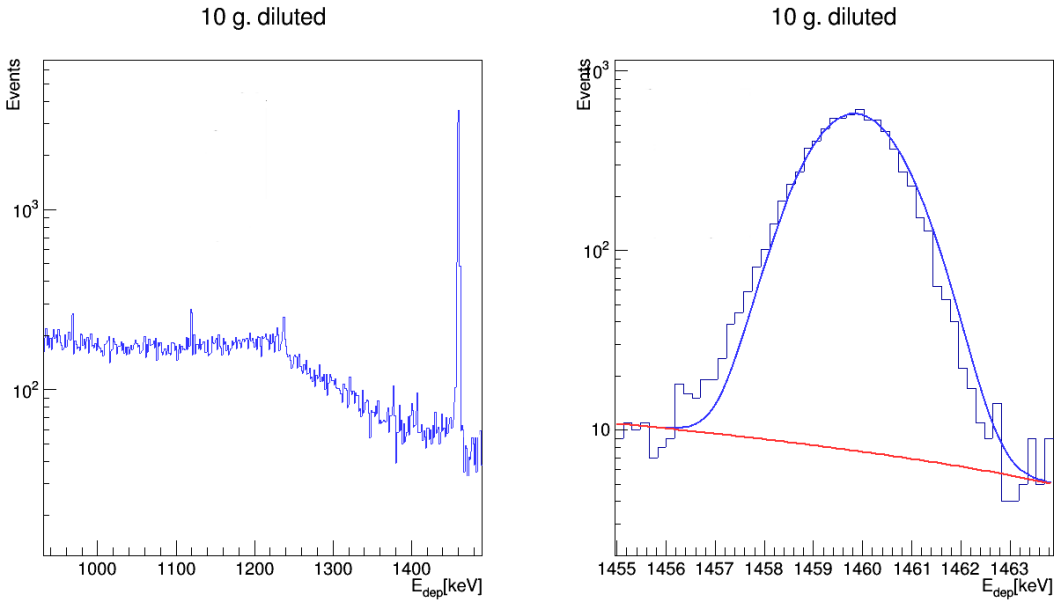

Figure 3.15: Energy spectrum recorded in ICN HPGe detector of a diluted sample of 10 g. potassium salt concentration. Background subtracted spectrum in whole energy range at left and about 1460 keV characteristic photopeak of ^{40}K at right.

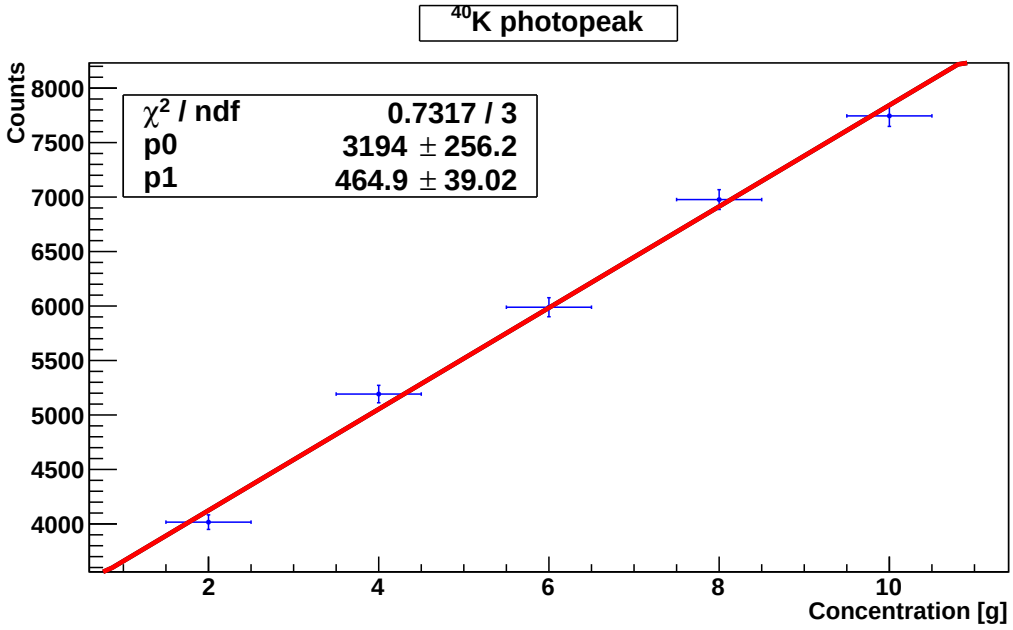

Figure 3.16: Energy spectrum recorded in ICN HPGe detector of a diluted sample of 10 g. potassium salt concentration. Background subtracted spectrum in whole energy range at left and about 1460 keV characteristic photopeak of ^{40}K at right.

In order to determine the number of hits in full width photopeak (FWP), the standard fitting method used previously is performed in energy spectra, in this case

the model of a straight line as a baseline is more accurate since signal is quite more tenuous. In figure 3.15, the energy spectrum of 10 g. solution is shown in two different ranges, it is completely distinguished for having high statistical fluctuations due to the low presence of ^{40}K active nuclei. The results of the peak counting as function of the potassium salt concentration are shown in figure 3.16, the horizontal uncertainty corresponds to half of the minimum measurement scale of the weighing machine, meanwhile the vertical bar corresponds to the uncertainty in the normalization parameter of Gauss distribution fitted to the photopeak. At first instance, the number of counts depends upon of the fitting parameters as well as of the percentage of diluted. Nevertheless it was found that counts in FWP has a linear dependency salt concentration.

Since no method is able to determine the absolute efficiency of a detector using extended samples, then the number of emitted photons by the samples will depend strongly on the result of the simulation. Once the efficiency is computed, then the number of emitted photons by the sample can be obtained and hence the ^{40}K concentration per salt gram.

Chapter 4

Monte Carlo simulation of ICN HPGe detector

In this chapter we will make a brief review of the importance of accurate software modeling in the designing of the highly sophisticated detectors utilized in experimental particle physics. Going through the generalities of Monte Carlo simulations as well as the basics of Geant4, the simulation toolkit mainly used in high energy physics (HEP) experiments, it is intended to give a global view of the correlation between the experiment and the simulation as well as the code construction process itself. Once this background is covered, the implementation of the HPGe detector experimental setup in the Monte Carlo simulation build in Geant4 is presented. At last, the main result, named the efficiency curve, is compared with the experimental result.

4.1 Geometry implementation

Up to now, the basic structure of a Monte Carlo simulation has been reviewed. These previous knowledge will materialize in the implementation of ICN HPGe detector simulation. For this, all the features seen in chapter 3 will be used. This includes the inner specifications given by manufacturer as well as the outer specifications obtained through a X-ray picture.

The Dewar and cryostat dimensions specified by manufacturer are shown in picture 3.1. These, together some of the internal parameters listed above, are the quantities of total certainty. Nevertheless, there is a set of inner parameters which have not been longer specified by ORTEC listed bellow:

- Sensitive crystal height.
- Sensitive crystal radius.
- Inner contact height.
- Geometric shape of the upper edge of the crystal.

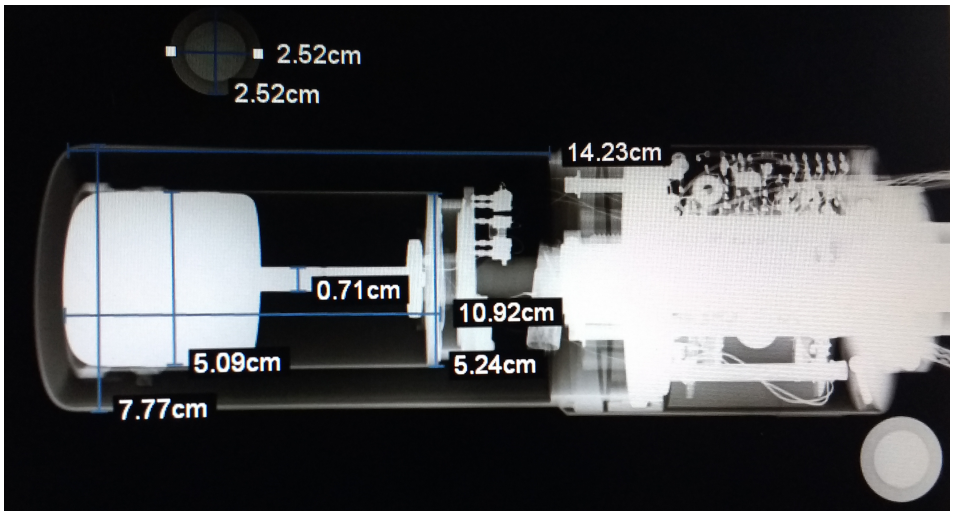

Figure 4.1: Frontal X-ray picture of ICN HPGe detector cryostat.

Item	Dimensions [mm]
Crystal diameter	50.9
Vacuum gap	13.4
Endcap width	1.0
Round corners curvature	7.0
Inner contact radius	4.8
Inner contact height	43.2
Dead layer width	0.65
Aluminium cryostat width	0.5

Table 4.1: ICN HPGe detector inner lengths.

In order to determine the actual lengths, a X-ray picture of the cryostat was taken at the Department of Medicine, Surgery and Zootechnics for Equidae from Facultad de Medicina Veterinaria y Zootecnia, UNAM, see figure 4.1.

To complete the detector initialization the inner geometry must be established. Besides the parameters that have been taken both form X-ray scan and from general featured specified by ORTEC [35], see figure 4.2, no information was provided by manufacturer of dead layer (DL) thickness surrounding the active volume of the germanium crystal. It depends highly on the current deterioration of the cryostat. Dead layer thicknesses of the order of 0.75 mm have been measured [14] for a similar coaxial vertical Ge detectors manufactured by ORTEC by bombarding its crystal with a collimated gamma source. Having similar dimensions, the ICN-HPGe detector crystal was expected to have a dead layer of around the same order. Monte Carlo simulations with varying dead layer thicknesses were performed to estimate this parameter by comparing the measured and simulated point-source photopeak efficiencies, finding a best match at a dead layer thickness of 0.65 mm.

Figure 4.2 shows a diagram of the actual dimensions of the HPGe detector imple-

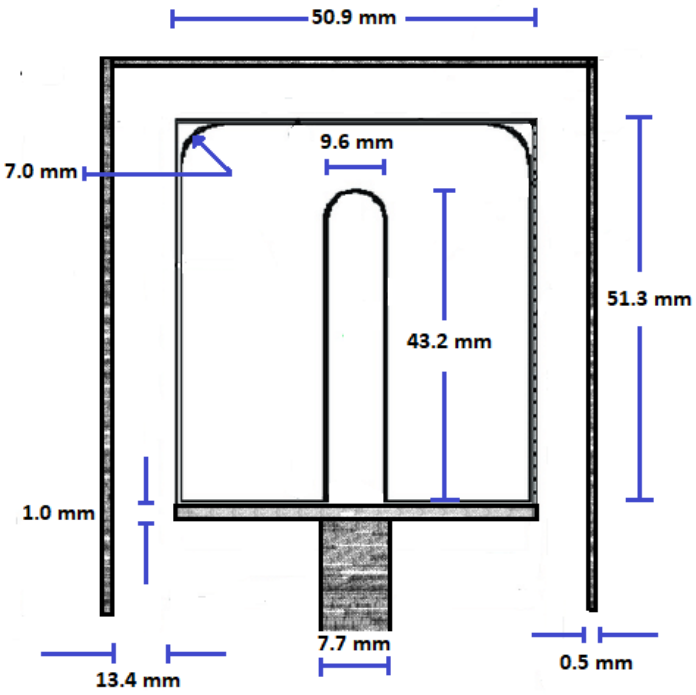

Figure 4.2: Actual dimensions of inner parameters of ICN HPGe detector.

mented in Geant4 and table 4.1 lists the whole set of cryostat. In simulation, the dead layer material is set also as Germanium in simulation but its logical volume is not set as sensitive detector, hence all the counts per deposited energy by gamma rays will not be apparent in energy spectra. Figure 4.3a shows the geometry implementation of the cryostat and figure 4.3b shows the experimental setup in a visualization interface in Geant4.

4.2 Point source simulation

The emitting source is idealized as punctual whose spatial position is set as the standard performed in experiments [19, 16], 25 cm above cryostat head. As first approach, the source is simulated just by initializing an outgoing photon with the same probability per solid angle unit, i.e. isotropically. The photon is sent from the mentioned point and its energy is set as the gamma decays from the sources kit shown in table 3.3.1. Once the incoming photon penetrates the sensitive crystal it will deposit an energy amount depending the interaction mode. This simulation will be preformed following the Monte Carlo (MC) process described in appendix A.2.4. For the algorithm to work properly every event must be independent from each other. This, in terms of the Geant4 toolkit, means that an event can not be initialized by a run until a previous beam has finished its journey and all the particles created through secondary interactions have been annihilated.

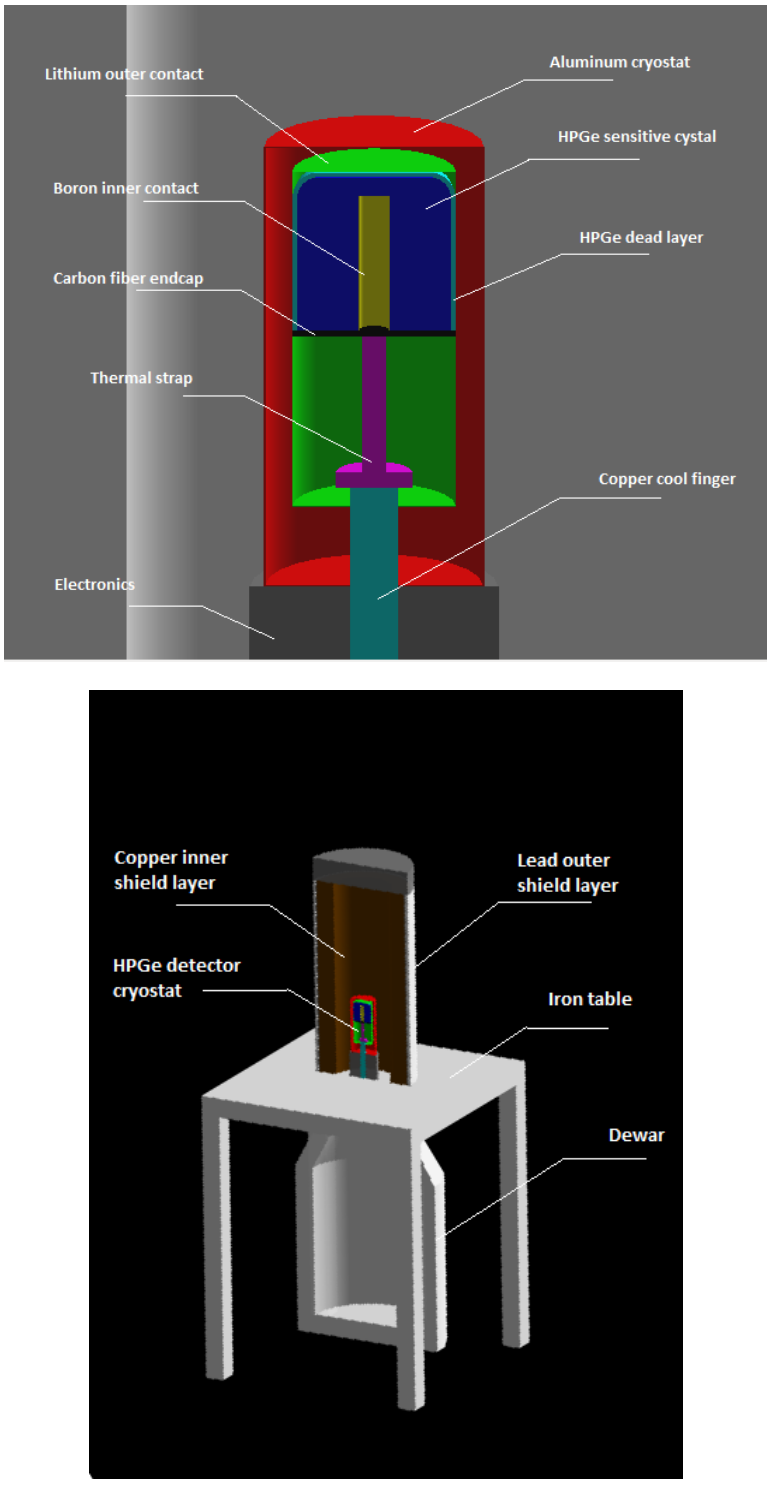

Figure 4.3: ICN HPGe detector geometry implemented in Geant4. Top: Inner features of cryostat. Bottom: Shield and experimental setup

The hit number per deposited energy unit and other information such as the hit spatial distribution of every step in an event are stored in a columnar data set. This object is best known in ROOT syntax as NTuple. Once the run is completed

all information in NTuples is stored in a ROOT file which works as a dictionary of standard C++ language. Under these conditions, the energy spectrum stored has an idealized appearance just like the discussed in chapter 2, figure 2.5, that is far from expected for an actual detector. This discrepancy is due to the lack of response of the sensitive crystal as a detector.

In order to include the resolution effect of the detector response in MC energy spectra, a fluctuation about each deposited energy value is sampled. This sampling is performed by recalling the Gaussian probability density function (PDF) centered on the actual deposited energy value and whose bell width is determined by the resolution value of the γ-ray energy in the following way:

$$f(\delta E|E_{dep},\sigma) = \frac{1}{\sqrt{2\pi\sigma^2}} \exp\left[-\frac{(E_{dep}-\delta E)^2}{2\sigma^2}\right], \tag{4.1}$$

$$E_{dep} \rightarrow E_{dep} + \delta E, \tag{4.2}$$

with

$$\sigma(E_{dep}) = \frac{RE_{dep}}{2\sqrt{2\ln(2)}}. \tag{4.3}$$

Recalling that the resolution R is also a function of deposited energy and we have proposed a model in eq. 3.7. This means that simulation requires experimental value of the resolution to be able to provide energetic spectra comparable to the experimental results. Once the sampling is performed, the hit distribution is also modified since every hit number has a deposited energy value attached, which is shifted by the sampling. Therefore every energy spectrum will acquire a smoother shape.

Recalling the geometrical factor 3.12, it has an order 10^{-3} for the point source distance $d = 25$ cm and the sensitive crystal radius $r = 2.55$ cm, shown in X-ray picture 4.1. Since a minimal amount of events of 10^3 is needed to perform correctly the Monte Carlo simulation a run of 5×10^7 events is programmed. To determine such amount of events, several tests were performed since the relative amplitude between the photopeak and the Compton edge depends strongly on the sensitive crystal dimensions.

4.2.1 Spectra comparison

First, the energy spectra of the sources of a single emission line are compared. This is performed by normalizing simulated spectra in photopeak amplitude, i.e.,

$$h_s \rightarrow h_s \cdot \frac{h_e[N_p]}{h_s[N_p]}, \tag{4.4}$$

where h_s is the simulated spectra histogram, h_e the experimental spectra histogram and N_p is the bin number of the photopeak mean, which is related to the photopeak energy due to the linear relationship between both.

To perform the comparison, the natural background of the experimental setup is subtracted from experimental spectra. A comparison between both simulated and experimental spectra of ^{54}Mn is shown in figure 4.4a, here we observe that the main features of an usual gamma-spectra measured with semiconductor detectors mentioned in section 2.2. These are Compton edge, photopeak and backscatter are present in both histograms.

This is the simplest case where there is only one gamma emission, nevertheless, actual sources such as ^{137}Cs offers a wider range of possibilities such as the emission of characteristic X-rays or , in the case of ^{65}Zn, the emission of the single escape peak.

A second, and more common case, is where the radioactive source has several lines of gamma emission. This is a more complex case which requires a more developed event initialization in MC simulation since every line has its own intensity and its emission probability. As established before this project has simulated the radioactive source as a mono-energetic outgoing photon, whose energy is well defined by the gamma lines of each source. Therefore, it is convenient to list the features in experimental spectra that simulation can not reproduce.

- **Double escape peak:** As discussed in chapter one, this feature is a direct consequence of electronic capture which occurs as a collective action of the atom and the electronic shells. Due to the lack of isotope initialization in MC simulation.

- **Characteristic X-ray:** Since such emission exclusively depends on the multipolar moments of charge of the atom, therefore it becomes obvious the lack of this feature in simulated spectra.

- **Natural background:** These would require to have a precise knowledge of all the fabrication materials present in experimental setup as well as their respective gamma lines and finally to simulate the emission within the continuous media.

Since the every run in MC simulation was initialized with 5×10^7 events, which does not match precisely with the actual gamma line intensity of the radioactive sources. Therefore, to compare the energy spectra for multigamma emitters, the photopeak amplitudes must be normalized correctly. This is can be performed in two gamma emitters by solving the second order equations system,

$$\begin{aligned} h_{exp}[N_1] &= a \cdot h_1[N_1] + b \cdot h_2[N_1] \\ h_{exp}[N_2] &= a \cdot h_1[N_2] + b \cdot h_2[N_2], \end{aligned} \tag{4.5}$$

whose solution is

$$
\begin{aligned}
a &= \frac{h_{exp}[N_1]h_2[N_2] - h_{exp}[N_2]h_2[N_1]}{h_2[N_1]h_2[N_2] - h_1[N_2]h_1[N_1]} \\
b &= \frac{h_{exp}[N_2]h_1[N_1] - h_{exp}[N_1]h_1[N_2]}{h_2[N_1]h_2[N_2] - h_1[N_2]h_1[N_1]},
\end{aligned}
\tag{4.6}
$$

where h_{exp} is the experimental spectrum histogram, h_1 is the simulated spectrum histogram of the first gamma-line, h_2 of the second, N_1 the bin number of the mean in the photopeak distribution for the first gamma line and analogously for N_2. In both cases of single peak and multi-peak spectra, the normalization to experimental spectra have been performed in order to compare their features with special attention on the photopeak region.

The correct implementation of the Ge detector geometry in simulation has a secondary, but not less important, consequence that is the normalization of Compton edge. A clear example where such normalization is enough to obtain a good match between simulation and experiment is ^{60}Co spectrum, shown in figure 4.6a. There we find out that the atomic structure of ^{60}Co does not have multipolar moments that let it emit X-rays and also its electronic configuration does not exhibit electronic capture to produce single or double escape peak emission. The remaining discrepancy is due to the lack of background in simulated spectrum.

A second case where the spectra comparison shows a clear lack of features listed above is shown in figure 4.6b, where we have compare the simulated spectrum with the experimental one of ^{57}Co, which is characteristic of two gamma emissions at 122.0 and 136.0 keV, as reported by [38]. The discrepancy in [60,120] keV range lies on the fact that ^{57}Co nucleus has dipolar magnetic moments that trigger X-ray emission, which are not included in simulation.

In spite of such discrepancies in energy spectra for some point sources, they do not compromise the photopeak shape since it has a good agreement between experiment and simulation. Therefore, it is expected that the counting of hits in full width photopeak has a deviation that does not exceed 20% of the experimental result, which is the uncertainty on the activity of the radioactive sources.

4.2.2 Simulated photopeak efficiency

Once more, the counting in full-width photopeak is performed as in the experimental case. A Gaussian PDF is fitted to the photopeak and the baseline with multiple Compton events is fitted as a straight line. In this case the number of emitted photons is a well defined parameter, hence the efficiency curve is obtained and compared with the experimental result, see figure 4.7. To obtain efficiency curve a model of inner structure is proposed in which the parameters that are not well known such as the dead layer and the inner contact radius are slightly varied in a safe range. Such ranges have been found [14] by sweeping the cryostat with a collimated source to determine the dead layer and to obtain information of the inner radius.

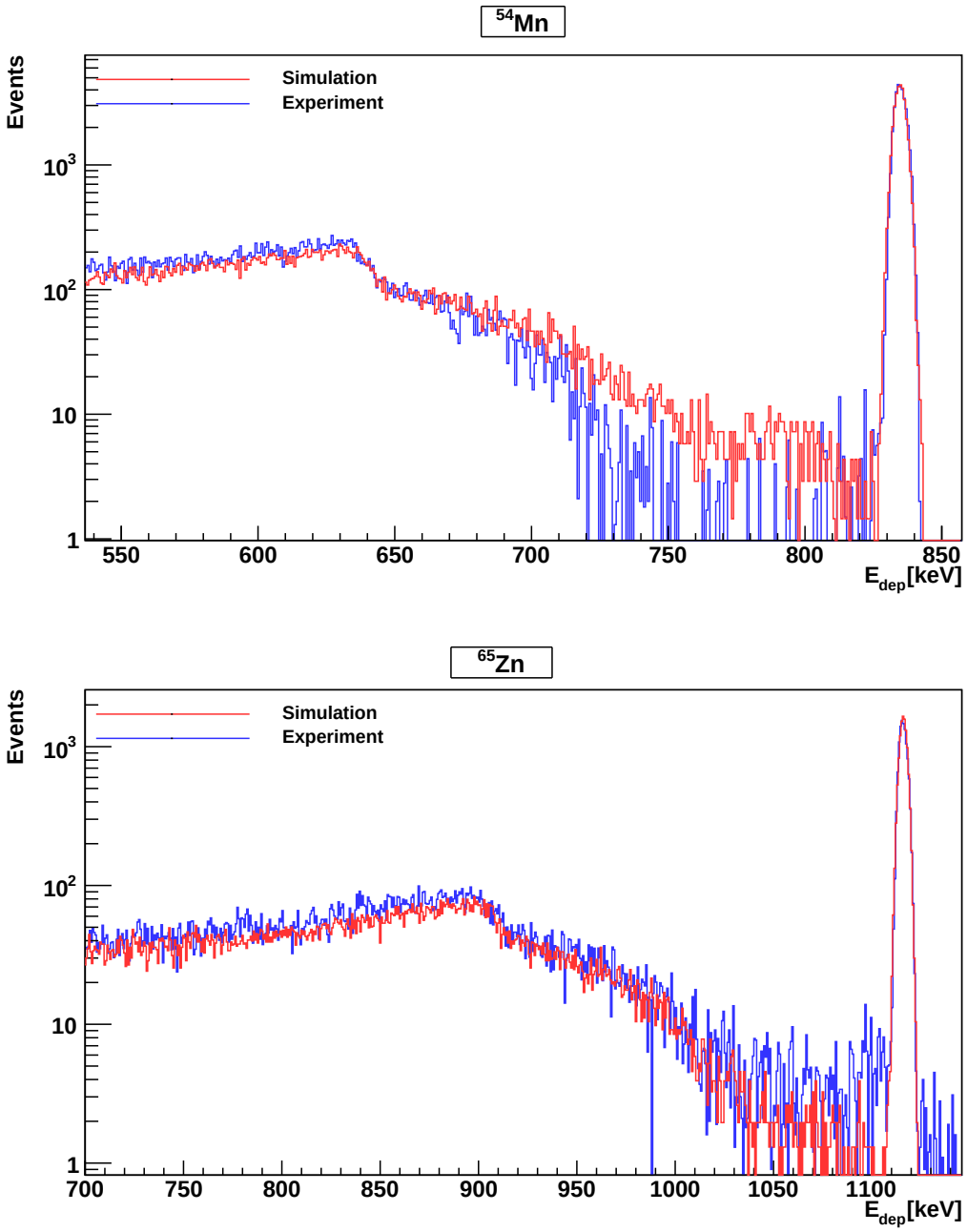

Figure 4.4: Energy spectra of the point single-peak sources (a) ^{54}Mn and (b) ^{65}Zn measured with the ICN HPGe detector and compared with their implemented simulation built in Geant4.

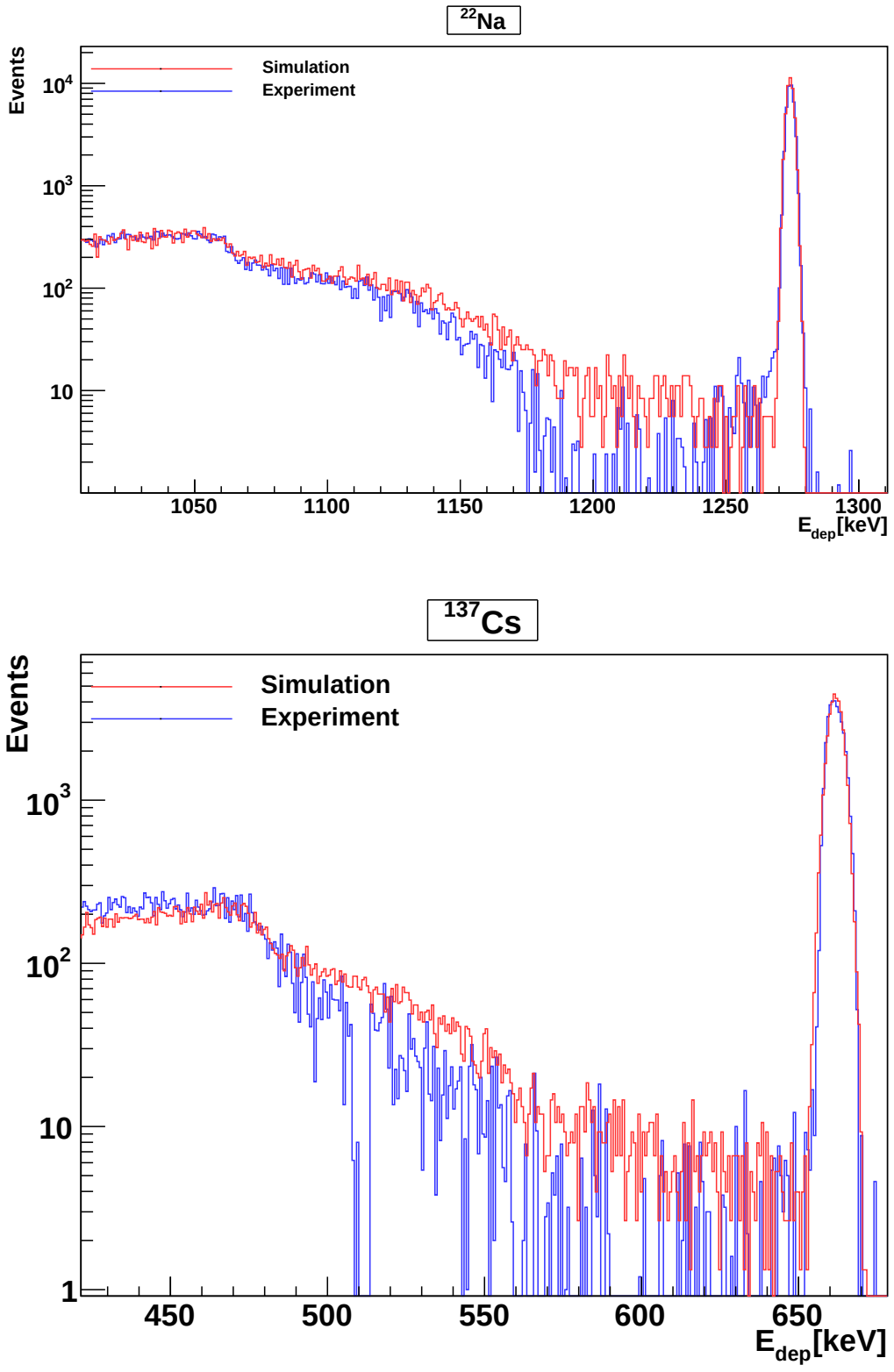

Figure 4.5: Energy spectra of the point single-peak sources (a) ^{22}Na and (b) ^{137}Cs measured with the ICN HPGe detector and compared with their implemented simulation built in Geant4.

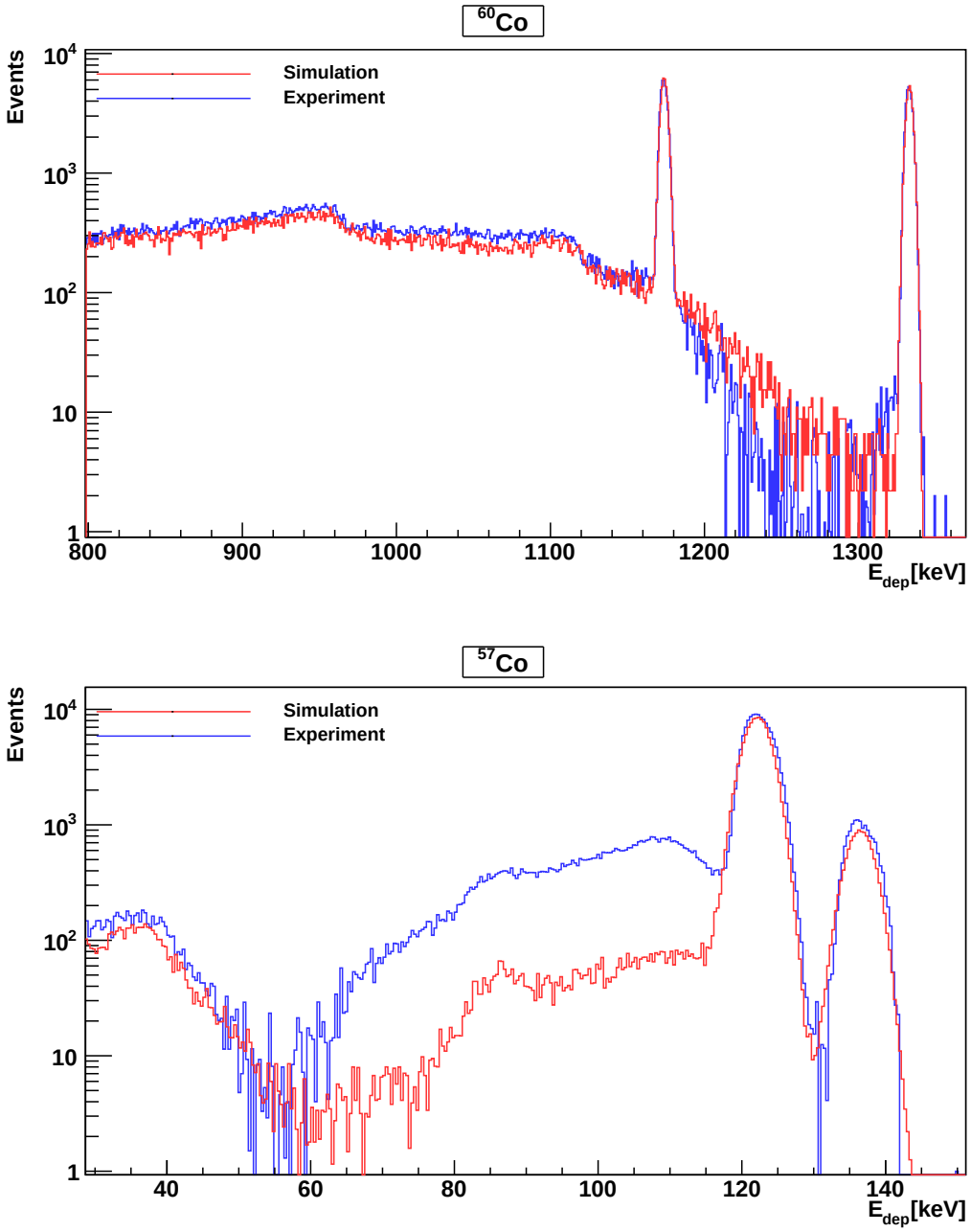

Figure 4.6: Energy spectra of the point double-peak source (a) ^{60}Co and (b) ^{57}Co measured with the ICN HPGe detector and compared with their implemented simulation built in Geant4.

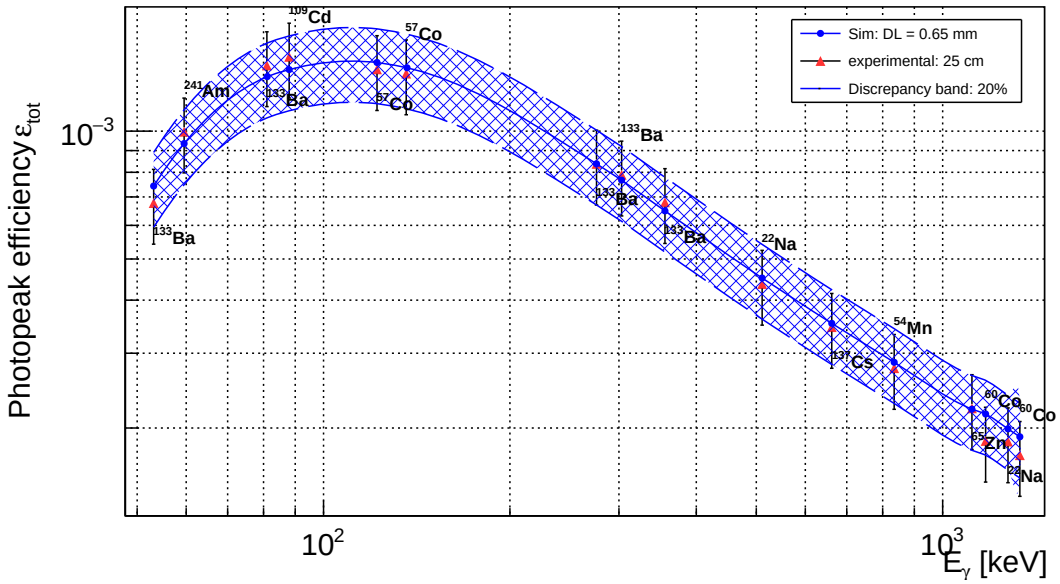

Figure 4.7: Efficiency curve of HPGe detector obtained through simulated spectra. Here the model of HPGe inner structure was set as DL = 0.65 mm.

Here we observe that simulation reproduce the same behavior as the experimental result, a linear tendency beyond 136 keV. Nevertheless, its curvature below 122.0 keV strongly depends on the chosen model, more specifically on the dead layer thickness since it is the outermost layer that has to go through the photon to penetrate the sensitive crystal. At low energy range the simulated efficiency curve is highly sensible to slight changes in inner structure. Therefore it must be chosen carefully, since some of the emission lines of natural elements present in many experimental components such as ^{210}Pb (46.53 keV) are in low energy range.

In order to establish a model to proceed with the extended sources case, the central model in the safe range is chosen which is also the one with a greater agreement with the experimental results. Recalling the uncertainty on the activity of the radioactive sources, a band of efficiency curve is obtained, see figure 4.7.

4.3 Extended source simulation

4.3.1 Extended geometry

So far, inner geometry model to the sensitive crystal to determine its agreement with experimental results. Now, the simulation of the ICN-HPGe detector is validated using water samples with a salt substitute containing Potassium Chloride (KCl) at different concentrations. First, the geometry of a clinical container is implemented in the simulation. This is performed by the usual method as described in previous section and setting as physical volume polypropylene. Then, it is necessary to declare

the basis solution of the sample solution, which is the injectable water solution. At first instance this seems to be a simple task when the water solution is considered uniquely as pure H_2O whose density is well known, nevertheless it contains a percentage of Potassium Chloride, just as discussed in previous chapter. This task must be performed by using the G4Material class reference which let user establish the actual percentage content of materials into a single one. Since distilled water label does not explicitly inform the actual potassium chloride concentration, then we proceed by setting it as 5% low concentration standard.

The density of basis solution, ρ_{bs}, is obtained by weighing the densities of the constituents by their respective percentages, i.e.,

$$\rho_{bs} = z_{H_2O}\rho_{H_2O} + z_{KCl}\rho_{KCl}, \tag{4.7}$$

where z_{H_2O} and ρ_{H_2O} are the percentage in solution an density of pure water respectively. Once the G4Material of the basis solution is declared, the actual sample solution can be further defined. Just as explained in chapter 3, the diluted samples were prepared with different potassium salt concentrations, therefore its presence in diluted sample must be declared in the material initialization. To declare the potassium salt material its chemical composition in NOVOXAL label is considered according table 4.1.

Item	Percentage
KCl	59 %
Iodized Salt	40 %
$NaAlO_2$	1 %

Table 4.2: Chemical composition of NOVOXAL Potassium salt.

Element	Percentage
Cl	60.823 %
NaI	38.85 %
Mg	0.29 %
Ca	0.029 %
P	0.008 %

Table 4.3: Chemical composition of standard Iodized Salt.

The chemical composition and the densities of the constituents in the table are well known. In the case of Iodized salt, it must be declared also as an auxiliary G4Material since it contains a wide variety of chemical elements [31], see table 4.3.1 Its density is obtained by weighting the constituents densities with the percentages as in equation 4.7. This process is performed once more with the items listed in table 4.1 to finally obtain the Potassium Salt material. Finally an ultimate material is

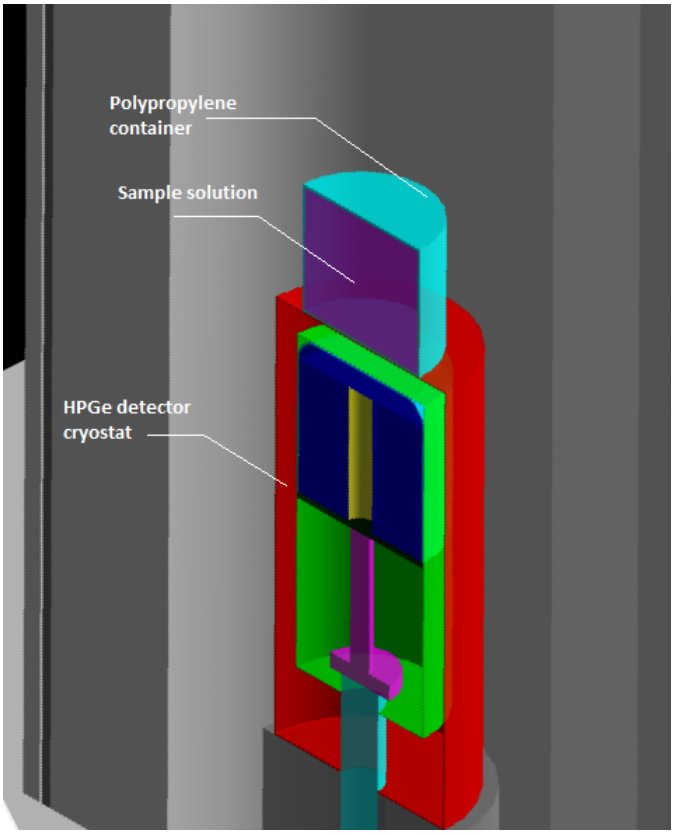

Figure 4.8: Filled polypropylene container geometry implemented in Geant4

declared as a mix of the basis water solution and potassium salt. As said in previous chapter, the container has a 50 ml. capacity, therefore the percentage of each material is obtained according to

$$z_{bs} = \frac{m_{bs}}{m_{bs} + m_{ps}}, \qquad z_{ps} = \frac{m_{ps}}{m_{bs} + m_{ps}}, \tag{4.8}$$

where m_{bs} and m_{ps} are the masses of the basis solution and the added potassium salt respectively. Here, the basis solution mass is obtained with the resulting density from equation 4.7. Such parameters as well as the declared materials for basis solution and potassium salt let us declare the sample material, whose logical volume fills the polypropylene container. The filled container is placed right on cryostat head. Figure 4.8 shows the whole set geometry including the extended source implemented in Geant4.

Every point within a extended sample can emit isotropically a γ-ray since the sample is presumably uniform. This is programmed in simulation by sampling a spatial point inside the clinical container physical volume and then running the simulation as in the point case. Unlike the point source case, the photon interacts with its surroundings before leaving the sample, hence it loses a fraction of its initial energy. Since it is desired to determine the photopeak efficiency in the characteristic emission energy

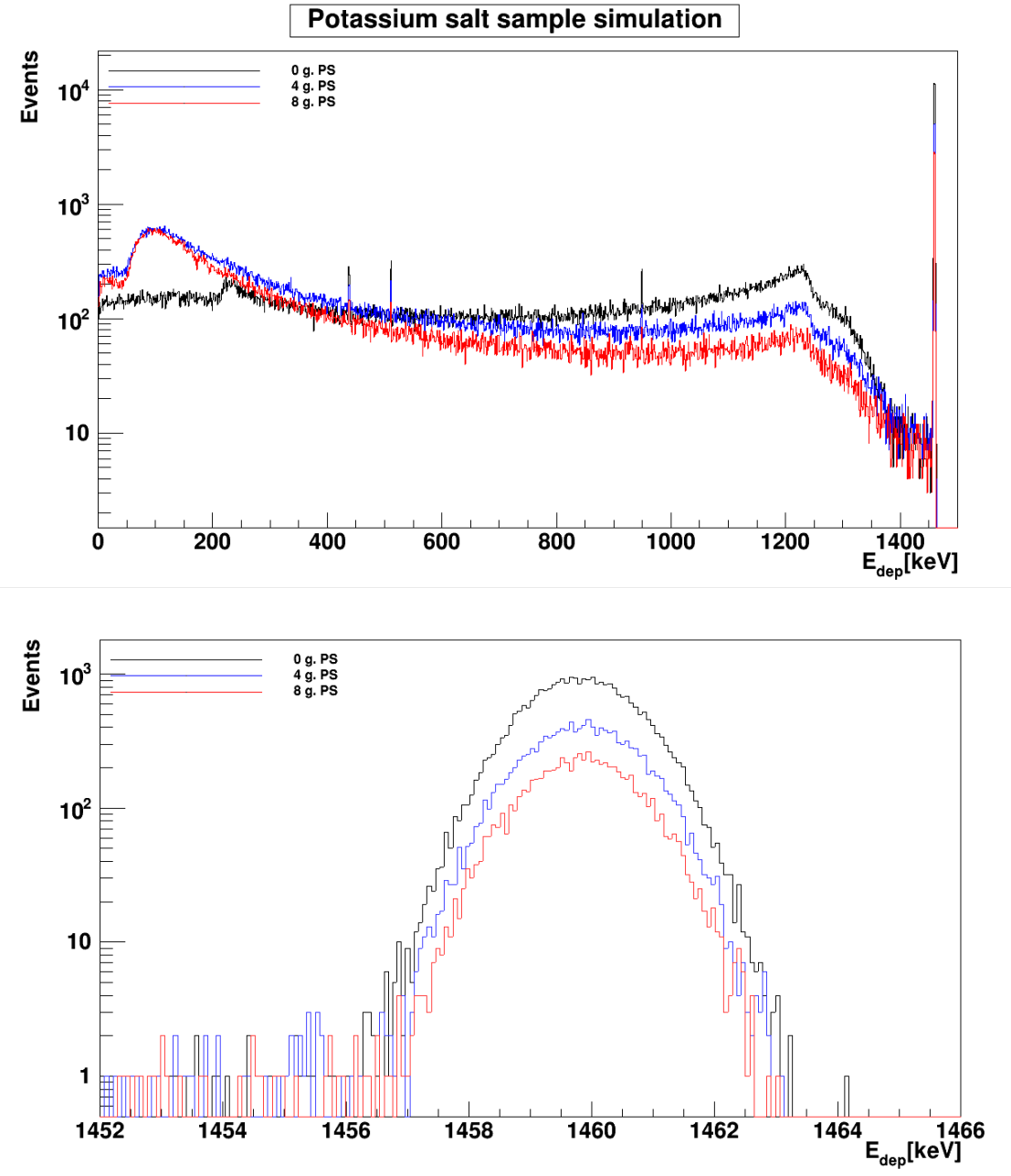

Figure 4.9: Simulated energy spectra of extended source compared for different sample concentrations.

of ^{40}K, then the γ-ray energy is set as 1460.0 keV. Due to the presence of potassium nuclei in sample the photon will be scattered or even absorbed more likely. This side effect is stronger if the Potassium salt concentration increases in material declaration. Figure 4.9 shows the actual effect on energy spectra. It becomes evident that since the outgoing photon lose a fraction of its energy then there will be an accumulation of events in low energy range to the point of deforming the Compton edge and even reducing the amplitude of the photopeak. This is a pure extended sample effect and

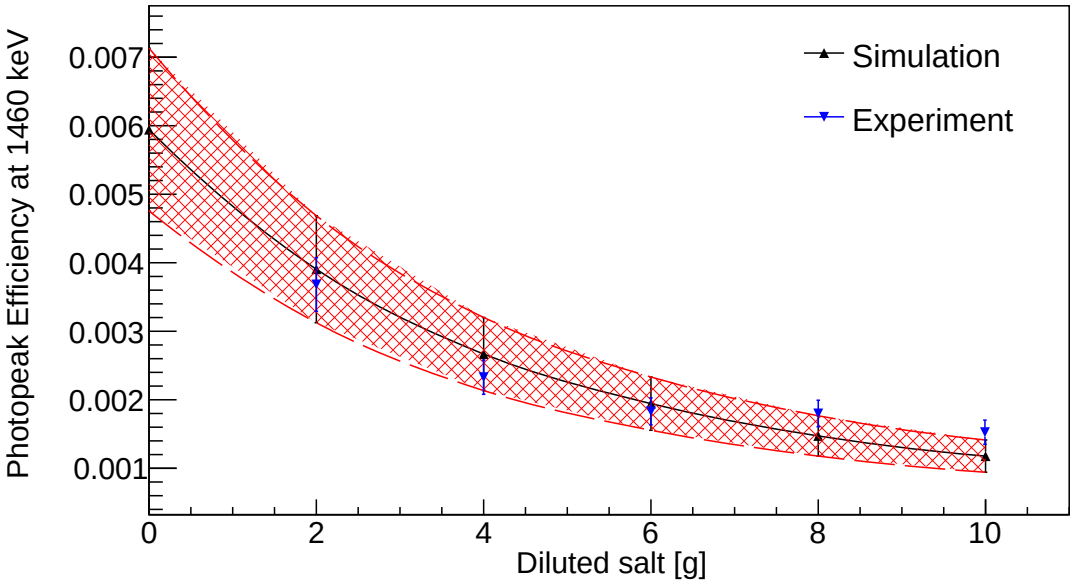

Figure 4.10: Simulated and experimental data extended source 40 K photopeak efficiency in the ICN-HPGe detector in a Potassium salt solution, as a function of the mass of diluted salt. A 20% systematic uncertainty is estimated in the simulation.

does not concerns to the detector geometry.

4.3.2 ^{40}K concentration

By fitting and integrating about the photopeak distribution as done in point source case for each concentration, the photopeak efficiency is calculated at 1460 keV gamma-ray energy for all the concentration values of potassium salt. Higher concentrations of KCl salt lead to a self-absorption effect of the γ-rays in the samples. The photopeak efficiency decreases as the potassium salt concentration in sample solution increases. This behaviour is expected since high concentration levels have implicit high sample densities because the potassium salt is denser than the basis solution. Thus the mean path of each photon within the sample will be shorter and the total number of photons leaving the sample will be slightly lower. Also the presence of other isotopes in the sample allow the photon to be scattered and transfer energy before hitting the sensitive crystal, so annihilation events are possible as seen in figure 4.9 (a). Figure 4.10 shows the simulated photopeak efficiency as function as salt concentration in sample in black color, the red shadow represents the actual error range of 20% systematic uncertainty from the point-like sources simulated efficiency.

Since photopeak efficiency depends in a wide range of parameters besides concentration salt, this project is not able to go beyond interpolating the intermediate values with a purely empirical function without trying to extract information from its parameters. In order to determine the actual ^{40}K mass concentration in Potassium salt

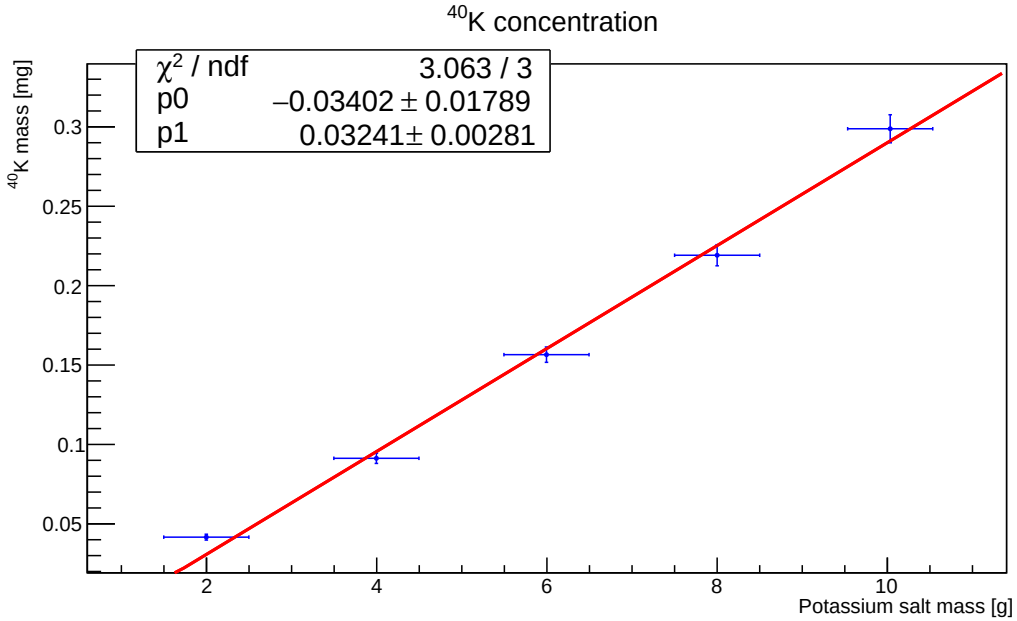

Figure 4.11: Mass of ^{40}K isotope per gram of potassium salt Novoxal measured with experiment-simulation method in ICN-HPGe detector

the activity A of the the sample is determined. For this, the number emitted photons by active nuclei N_t must be computed by recalling photopeak efficiency definition given in equation 3.8

$$A = \frac{N_t}{T} = \frac{N_p}{\varepsilon_p T}, \tag{4.9}$$

where T is the exposure time of the sample, ε_p is the photopeak efficiency at 1460 keV and N_p is the number of hits in full with photopeak, which have been determined in chapter 3 for each concentration level. Later, by multiplying the activity by the half-life of ^{40}K the number of active nuclei in sample is obtained. Finally using Avogadro relation, the mass of ^{40}K present in the sample can be obtained,

$$m_{K^{40}} = \frac{A\tau M}{N_A} = \frac{A t_{1/2} M}{\ln(2) N_A}, \tag{4.10}$$

where $t_{1/2} = 1.251 \times 10^9$ yr. is the half life, τ the mean life, $M = 1563.93$ g/mol the molar mass and $N_A = 6.022 \times 10^{23}$ the Avogadro number. Using these values and the photopeak efficiency, the ^{40}K mass is computed for every potassium salt concentration value. Figure 4.11 shows the results of the calculation, as explained in chapter 3 there is an intrinsic uncertainty in the salt concentration due to the weighting machine precision. A linear tendency is clear, then a straight line is fitted to data and the obtained slope is the rate of ^{40}K milligrams per potassium salt gram:

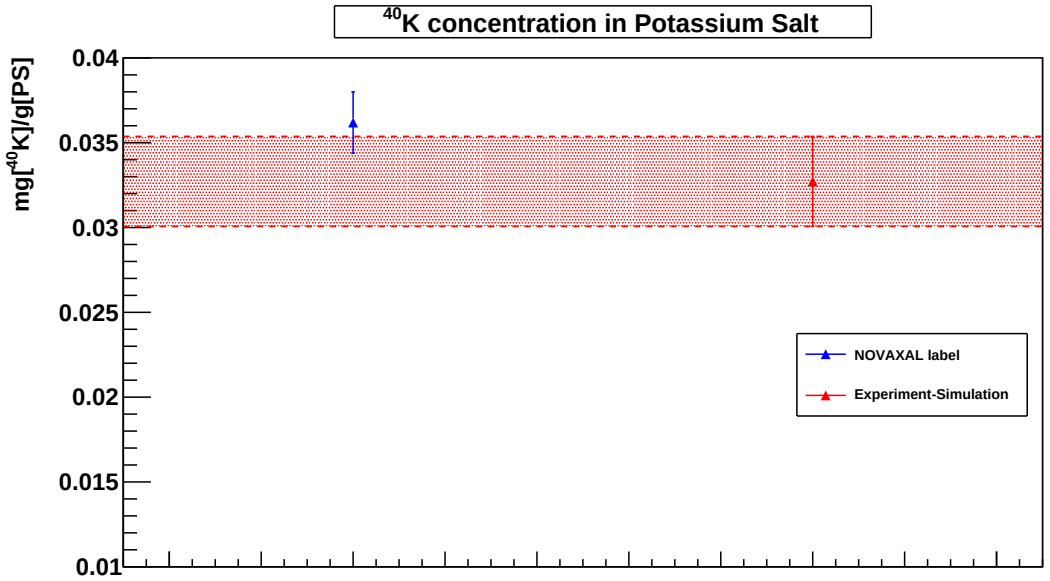

Figure 4.12: ^{40}K milligram concentration per potassium salt rates obtained, in blue, from information in Novoxal label and, in red, from experiment and extended source simulation.

$$\eta_s = (0.032 \pm 0.003)\ mg[^{40}K]/g[PS] \tag{4.11}$$

To compare such result, the same rate has been computed directly form Novoxal label information. According this, an amount of 464 mg. of pure potassium is present in every 1.5 g. of salt. This means a concentration of 309.33 mg of potassium per salt gram. By multiplying this quantity by the natural abundance of ^{40}K, which is 0.0117% [38] the rate of ^{40}K milligrams per potassium salt gram is obtained:

$$\eta_l = (0.036 \pm 0.002)\ mg[^{40}K]/g[PS]. \tag{4.12}$$

Since the evaporation process to produce Potassium chloride is complete unknown for Novoxal company, then the uncertainty is estimated as lower than 5% in potassium concentration. Figure 4.12 shows the comparison between both rates. In order to verify that rate 4.12 is actually consistent with the simulated photopeak efficiency its experimental calculation is performed by assuming a central concentration rate of 4.12 and following the reverse process to obtain 4.11. The comparison between label information and simulation-experiment photopeak efficiency is shown in figure 4.10, both results seem to agree within their error bars.

The experiment-simulation one central value is under the central value of such obtained from label, this is related to the fact that experimental spectra were recorded

for long period of time. This allows a fraction of the potassium salt to settle at the bottom of the polypropylene container, hence the radioactive nuclei get closer to the sensitive crystal. This effect is not present in simulation since radioactive nuclei and point sources stay always at their initial spatial position. Hence, a greater ratio of photons counts in full-energy photopeak in experimental results than in simulated case is expected.

Chapter 5

Conclusions

The HPGe detector described in this project is part of the detector suite planned for the first underground laboratory in Mexico at Mineral del Chico, Hidalgo. The efficiency and resolution of the detector, in conjunction with the low radioactive background provided by the mine environment, will allow the study of a wide range of samples with low radioactive content. This detectors will be used for experiments in nuclear and astroparticle physics, biology and geology. The energy scale and resolution of the ICN-HPGe detector were obtained over the energy range relevant to low-background astroparticle experiments and environmental radiation studies.

Energy spectra were recorded in the ICN HPGe detector by placing several radioactive point sources from LLC Spectrum techniques at a nominal distance of 25 cm above the detector cryostat and whose gamma-rays energies sweep a range from 53 keV to 1333 keV. By fitting a normal model to the photopeak distribution of each source the resolution at every energy from the source kit was determined. For this data set, an inverse square root model was proposed to interpolate data. Also, from the fitting the photopeak efficiency has been determined for energy energy value. Particularly at the second gamma emission line of ^{60}Co at 1332.5 keV a photopeak efficiency value of 1.726×10^{-4} was obtained, which corresponds to a relative efficiency of 14.38%. This result agrees with the nominal value given in ORTEC technical sheet [35] for HPGe coaxial detectors.

By extracting the dimensions from the X-ray lateral picture of the HPGe detector taken at Facultad de Medicina Veterinaria y Zootecnia, UNAM, a Monte Carlo simulation of the detector was built in Geant4. The dead layer width was set in two stages according to previous experiments [14] where collimated gamma rays were shot to a HPGe sensitive crystal to estimate such parameters. The point sources were programmed as monoenergetic isotropic photons sent from the same spatial position as the experimental case. Both experimental and simulated spectra showed a good coincidence in the photopeak region for every source. By integrating the simulated spectra with the same methodology of the experimental one, the efficiency curve was obtained in the [53.16,1460] keV energy range. Such curve matches reasonable with experimental results, specifically at 1.33 MeV a percentage error of 10.47 % was obtained between the central value of both results. Also, the relative efficiency of 15.84%

which also agree with the ORTEC technical sheet.

Finally, to test the MC simulation for extended sources several samples were prepared by diluting different concentrations of Novoxal Potassium salt in injectable water solution and putting them into polypropylene containers. Placing the samples on the detector head and recording long spectra, the number of events in the full energy photopeak were determined by the same method as previous cases. In order to determine the actual concentration of ^{40}K isotope in Potassium salt, the geometry of the source was added to the simulation. Just as expected, the radioactive nuclei concentration in the sample media has a high impact in the total number of photons arriving to the sensitive crystal. It was found that a non-linear decreasing tendency in simulated photopeak efficiency as function of the Potassium salt concentration in sample both for experiment-simulation and for Novoxal label information. Using simulated efficiency and the number of events in 1460 keV energy photopeak, the activity of the sample has been determined as function of potassium salt mass concentration. Finally the mass concentration of ^{40}K per gram of diluted potassium salt was determined. From the experiment-simulation a concentration ratio of $\eta_s = 0.032 \pm 0.003$ mg[^{40}K]/g[PS] which is in good agreement with the Novoxal label information $\eta_l = 0.036 \pm 0.002$ mg[^{40}K]/g[PS] having a percentage error of 9.41% between central values. The results of this project have been included in a paper that has been sent to the Journal of Instrumentation (JINST) which is waiting to be published. It aims to be a first step towards establishing the performance of the LABChico radio-assay capabilities.

Bibliography

[1] Peskin, Michael, *An introduction to Quantum Field Theory*. Perseus Books, 1995 Massachusetts.

[2] Knoll, Glen F., *Radiation Detection and Measurement Third Edition*. John Wiley and Sons, 2009 Michigan.

[3] Leo, William R., *Techniques for Nuclear and Particle Physics Experiments*. Springer, 1994 New York.

[4] Gilmore, Gordon R., *Practical Gamma-ray Spectrometry 2nd Edition*. John Wiley and Sons, 2008 Warrington, UK.

[5] Poeranu, Dorin N., *Nuclear Decay modes first Edition*. Taylor & Francis, 1996 Dubna, Russia.

[6] Lieser, Karl H. *Nuclear and Radiochemistry: Fundamentals and applications*. Wiley-VCH, 2001 Darmstadt, Germany.

[7] Byun, Soo Hyun *Radioisotopes and Radiation Methodology I, II.*. Lecture Notes, McMaster University, Canada.

[8] Gaucci, Dan G. *Handbook of Nuclear Engineering*. Springer, 978-0-387-98130-7, 2010.

[9] Pathria, R. K. *Statistical Mechanics: Third edition*. Elsevier, 2011 San Diego, USA.

[10] Riegler, Werner *Particle detectors*. CERN, Summer student lectures 2010, Switzerland.

[11] S. M. Sze, *Semiconductor Devices Physics and Technology, 2nd ed.*. John Wiley, 2002 New York, USA.

[12] M. Baum, Edward, et. al., *Nuclides and Isotopes 16th Edition*. Lockheed Martin, 2002 New York, US.

[13] Aguilar-Arevalo Alexis, et. al., *The CONNIE experiment*. arXiv:1608.01565v3, 2016.

[14] Boson, Jonas, et. al., *A detailed investigation of HPGe detector response for improved Monte Carlo efficiency calculations*. Nuclear Instruments and Methods in Physics Research A, 587 (2008) 304–314, 2008.

[15] Sanderson, C.G., *Comparison of Ge(Li) well and n-type coaxial detectors for low energy gamma-ray analysis of environmental samples*. Environmental Measurements Lab., New York, NY, 12587405, 1980.

[16] Montalván Diango, et. al., *Determination of the HPGe detector efficiency in measurements of radioactivity in extended environmental samples*. Applied Radiation and Isotopes, 130 (2017) 34-42, 2017.

[17] Huy N. Q., et. al., *Study on the increase of inactive germanium layer in a high-purity germanium detector after a long time operation applying MCNP code*. Nucl. Instrum. Methods Phys. Res., Sect. A 573, 384–388.

[18] Andreotti E., et. al., *Determination of dead-layer variation in HPGe detectors*. Applied Radiation and Isotopes, 87 (2014) 331–335.

[19] Challan Mohsen, *Gamma-ray efficiency of a HPGe detector as a function of energy and geometry*. Applied Radiation and Isotopes, 82 (2013) 166–169, 2013.

[20] Lépy, Marie-Christine, et. al., *Study of the response function of a HPGe detector for low-energy X-rays*. Nuclear Instruments and Methods in Physics Research A 505 (2003) 290–293, 2003.

[21] Nakano G.H., et. al., *Characteristics of Large Intrinsic Germanium Detectors Operated at Elevated Temperatures*. IEEE Trans. on Nucl. Sci. NS-24, No. 1 (1977).

[22] Scovell P.R., et. al., *Low-background gamma spectroscopy at the Boulby Underground Laboratory*. Astroparticle Physics, 97 (2018) 160–173, 2018.

[23] Luke P.N., *Voltage-assisted calorimetric ionization detector*. Journal of Applied Physics. 64:6858-6860, 1988.

[24] Kasap Safa, Capper Peter, *Handbook of Electronic and Photonic Materials 2nd Edition*. Springer, 10.1007/978-3-319-48933-9(2007).

[25] Dale Jeremy, *Method of Evaluating the effect of HPGe Design on the Sensitivity of Physics Experiments*. North Carolina 2009, USA.

[26] Werner M., et. al. *Physical Review Journal*. B37,3930(1985)

[27] Lawson, Ian, *Ultra-low background measurement capabilities at SNOLAB*. Journal of Physics: Conferences Series, 718 042034, 2016.

[28] Fourches N., *High defect density regions in neutron irradiated high-purity germanium: Characteristics and formation mechanisms*. Journal of Applied Physics. 77:3684-3689, 1995.

[29] Armengaud E, et. al., *Performance of the EDELWEISS-III experiment for direct dark matter searches.* Journal of Instrumentation. 12:P08010, 2017.

[30] Van de Water, Richard G., *Convincing Search for Sterile Neutrinos at LANL Coherent Captain-Mills (CCM) Experiment.* United States Department of Energy. `https://www.osti.gov/servlets/purl/1572310.`

[31] Holman, J. C., et. al., *Iodized Salt.* Chilean Iodine Educational Bureau, 18 (1958) 255-273, 1958.

[32] Holmes, Andrew, *From sunlight to electricity.* Australian Academy of Science, `https://www.science.org.au/curious/technology-future/solar-pv`

[33] Comarca Minera Hidalgo UNESCO Global Geopark, 2020. `https://www.geoparquehidalgo.com`

[34] Ametek, *PX5-HPGe: User Manual.* `https://www.amptek.com/products/digital-pulse-processors/`

[35] ORTEC, Ametek, *GEM Series Coaxial HPGe Detector: Product Configuration Guide.* `https://www.ortec-online.com/-/media/ametekortec/brochures/`

[36] ORTEC, Ametek, *HPGe Detector Manufacturing.* `https://www.ortec-online.com/`

[37] Geant4: A simulation toolkit. *User Documentation.* `https://geant4.web.cern.ch/support/user_documentation`

[38] National Laboratory Henri Becquerel. *Atomic and Nuclear Data.* `http://www.lnhb.fr/nuclear-data/nuclear-data-table/`

[39] Spectrum techniques. *Source to detection, for Educator and Professional.* `https://www.spectrumtechniques.com/products/sources/`

[40] Geant4, a simulation toolkit. *User documentation: Version: Geant4 10.6.* `https://geant4.web.cern.ch/support/user_documentation`

[41] Favela Francisco, Guerra Jaime. ***histoGe**: source code Version 2.0.* `https://github.com/ffavela/histoGe`

Appendix A

Geant4: Simulation toolkit

A.1 Monte Carlo method

The Monte Carlo method is a process widely used in many science branches. It is based on random variables sampling, a procedure that produces an large stream of random stochastic variables that are independent and identically distributed according to some distribution function, which depends upon the nature of the problem. Here, a stochastic variable can be either a number or a configuration of the system. In the case of a HEP simulation, such configurations are identified as beam trajectories.

A probability density function (PDF) $f(x)$ is a density function, i.e., it specifies the probability of realization of a stochastic variable x. It accomplishes the following requirements:

- Completely defined in the domain of the stochastic variable, D.
- It is defined non-negative in D.
- It is normalized, i.e.,

$$\int_D f(x)dx = 1. \tag{A.1}$$

A.2 Geant4

A.2.1 Generalities

In high energy physics (HEP), cosmology and physical medics a set of experimental data can be simulated in two stages, the event generation or beam initialization and the detector response. Event generation describes the initial state of the the particle beam. The output of the event generation is used as input for the next stage.

The response of a detector to the passage of the scattered particles involves random processes such as ionization, multiple Coulomb scattering among others. Therefore

the transport of particles through a detectors setup can be effectively implemented using the Monte Carlo techniques.

Geant4 is a free software package for a modern object-oriented environment based in C++ and Python. It is composed of a kit of tools that can be accurately used to simulate either the event generation or the detector response. The simulation features included in the toolkit are [40]:

- Geometry of the system,
- materials involved,
- fundamental particles of interest,
- tracking of particles through materials and electromagnetic fields,
- physics processes governing the fundamental interactions,
- response of sensitive detector components,
- generation of event data,
- storage of events and tracks,
- visualization of the detector and particle trajectories, and
- capture and analysis of simulation data at different levels of detail and refinement.

The manner in which these major categories are related is shown in figure A.1. It is not intended to give an exhaustive revision of the full usage of each category, instead a brief review of the relevant categories for the HPGe simulation.

A.2.2 Event generation and detector construction

Event initialization is the simplest stage in a HEP simulation. It is done by configuring all the intrinsic characteristics of the particles that make up the beam. Besides the initial kinematic conditions such as the space-time position and momentum direction, the intrinsic properties of the beam's constituents (particles or nuclei) must be established such as electric charge, spin, isospin. For this, Geant4 is provided with a class that contains a wide catalog of all the inner features of particles in standard models as well as the definition of stable ions when it comes to a radioactive decay.

Geant4 is based on a semi-classical approach. Since a defined trajectory is assigned to all the particles, they are treated classically rather than wave functions, but their interactions such as cross sections and final states take often into account the results of quantum field theory effects.

On the other hand, the detector definition requires a detailed description of its geometrical elements as well as the material composition and electronics generalities.

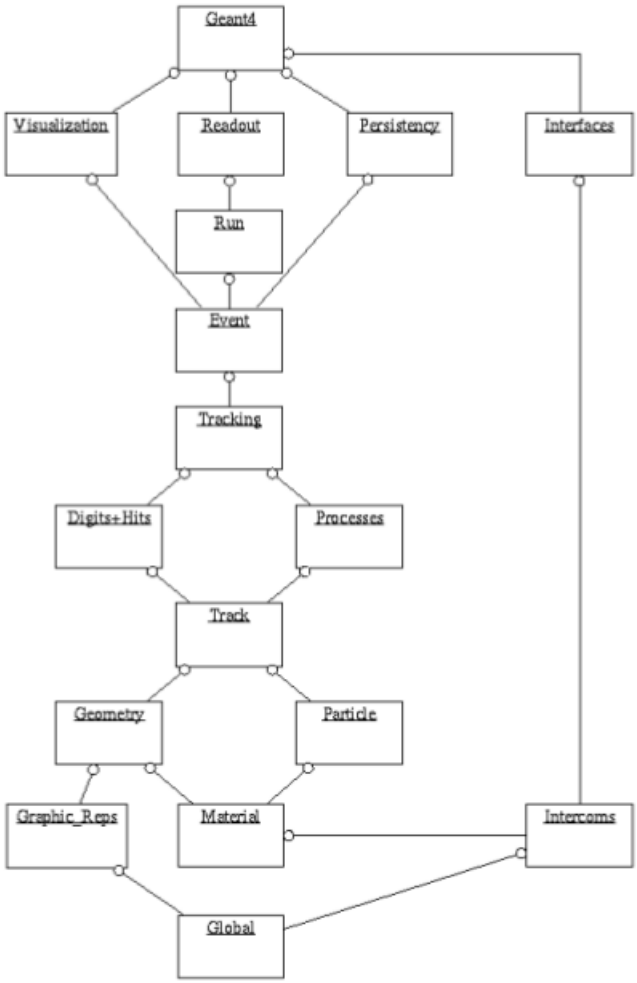

Figure A.1: Geant4 class category diagram.

The geometrical representation of detector elements focuses on the definition of solid models, their spatial position and the inclusion of either uniform or non-uniform electromagnetic fields that could vary in time. For this, detector definition is channeled in three major classes:

- **Solid volume (G4VSolid):** Defines the shape and size of all detector's constituents.
- **Logical volume (G4LogicalVolume):** Defines the physical features of each solid volume such as material, density and sensitivity.
- **Physical volume (G4VPhysicalVolume):** Defines the spatial location of each physical volume.

Figure A.2 shows the definition of a solid volume in simulation, every quantity

```
G4Polycone(const G4String& pName,
           G4double phiStart,
           G4double phiTotal,
           G4int numRZ,
           const G4double r[],
           const G4double z[]);
```

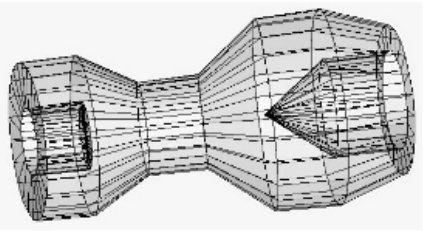

Figure A.2: Definition of a polycone in Geant4. This solid volume requires the angular range, the number of corners and their positions in cylindrical coordinates as income.

such as mass, energy, density is nrepresented by multiplying the numerical value with the unit.

A physical interaction of the beam with the sensitive crystal is known as an event. The storage of events is of huge importance since they simulate the physical signal in the actual detector and hence the detector response. To propagate a beam within a detector with a EM field the equations of motion of charged particles are included in the toolkit.

A.2.3 Physical processes

The physical processes describe how the particles interact throughout matter, they must be set according to the experiment scope. Geant4 is provided with seven major categories. In this project we focus exclusively on two of them which are relevant for the HPGe detector simulation. They are listed with the major processes:

Electromagnetic processes:

- Photon processes such as Compton Scattering, gamma conversion, photo-electric effect.
- Lepton/Anti-lepton processes such as pair annihilation, pair creation, Bhabha scattering, ionization and Bremstrahlung radiation.
- Hadron-ion process: Mostly ionization.
- Multiple Compton scatterings.
- Low energy electromagnetic processes as Rayleigh scattering.

When an incident gamma ray beam is enough energetic to compare its wavelength with nucleons' radii other kind of processes that involves strong interactions must be taken into account. These are the Hadronic interactions and their importance lies on

effective mechanisms that involve the inclusion gluons (gauge bosons) and quarks as well as their primary interactions between them and with photons and leptons. The main mechanisms included in Geant4 toolkit

Hadronic interactions:

- Lepton-Hadron interactions.
- Photonuclear and electronuclear reactions.
- Nucleus-nucleus reactions.
- Elastic scattering.
- Nuclear cascades.
- Fission, evaporation and break-up models.
- Low energy neutron interactions.
- Radioactive decays.

A.2.4 Tracking

The tracking stage manages the major objects that are in charge of perform properly the particle's beam properly. These objects are:

- **Event:** It is the basic unity of simulation in Geant4. At beginning of simulation an event contains primary particles that make up the beam. These primaries are pushed into a stack. When the stack becomes empty, processing of an event is over. The main parameters of the beam that distinguish an event are:
  - Initial position and momenta direction.
  - In case of radioactive decay, the ion parameters and exciting energy.
- **Run:** It is a collection of events which share the same detector conditions. Within a run, detector conditions can not be changed. These are:
  - Detector geometry and composition.
  - Involved physical processes.
- **Track:** It is a snapshot of the particle. It has the physical quantities corresponding only to the current instance i.e. it does not record quantities from previous events. A track is updated by steps. Finally, a track is deleted when the particle:
  - goes out of the world volume,
  - disappears by a decay or scattering.,

  - goes down to zero kinetic energy and no additional process is required.

- **Step:** A step has two spatial points that are well characterized by the volume and the material in which they are located. It also includes also an increase of information of a particle that contains the energy loss on the step (or deposited energy), time-of-flight spent by the step, etc. In case a step is limited by a volume boundary, the end point physically stands on the boundary, and it logically belongs to the next volume.

In tracking a particle a stepping manager plays an essential role. It takes care of all message passing between objects in the different categories relevant to transporting a particle. Starting from the fact that the probability of having an interaction at a distance L within a material in detector by the physical process i is

$$p_i(L) = 1 - e^{L/\lambda_i}, \tag{A.2}$$

where λ_i is the mean free path. Hence, the algorithm to handle one step of the track in simulation is the following:

1. Get all the λ_i values for all relevant processes.
2. Sample the free path length L from the distributions of all participating processes.
3. The geometry navigator calculates "safety distance", the distance to the next volume boundary. If the minimum physical step length from the processes is shorter than "safety distance", the physical step length is selected as the next step length.
4. If the minimum physical step length from the processes is longer than "safety distance", the former is taken and the distance to the next boundary is recalculated.
5. Propagate the particle by this step through the chosen track.
6. All active physical interactions are invoked.
7. After the interaction, the change in particle's kinetic energy will be the sum of the contributions from these processes.
8. If the particle still exists, go to 1.

For simplicity the algorithm has been simplified, nevertheless it is important to point out that step counts in stage 7 updates deposited energy by the beam the spatial and angular distributions of hits and, as mentioned, hits number per deposited energy. All these information is stored in a ROOT columnar data set, that is best known as NTuple.

A wide variety of tools to analyze recollected data have been developed, which are specially oriented to reading and processing data in columnar form. In this project, the set of interfaces designed for data analysis iAIDA since it has been implemented in C++ and adapted to ROOT data processing.

The main outputs from the Geant4-built simulation are the energy spectra and hit distribution in sensitive detector, which are directly comparable with experimental results.